AD NUMBER

AD922178

NEW LIMITATION CHANGE

TO

Approved for public release, distribution unlimited

FROM

Distribution authorized to U.S. Gov't. agencies only; Test and Evaluation; 31 JUL 1974. Other requests shall be referred to Naval Research Lab., Washington, DC 20375.

AUTHORITY

USNRL ltr, 11 Sep 1981

AD 922 178

NRL Report 7739

An Introduction to Adaptive Arrays

WILLIAM F. GABRIEL

Microwave Techniques Branch
Electronics Division

July 31, 1974

NAVAL RESEARCH LABORATORY
Washington, D.C.

SECURITY CLASSIFICATION OF THIS PAGE (When Data Entered)

REPORT DOCUMENTATION PAGE		READ INSTRUCTIONS BEFORE COMPLETING FORM
1. REPORT NUMBER NRL Report 7739	2. GOVT ACCESSION NO.	3. RECIPIENT'S CATALOG NUMBER
4. TITLE (and Subtitle) AN INTRODUCTION TO ADAPTIVE ARRAYS		5. TYPE OF REPORT & PERIOD COVERED Interim report on a continuing problem. 6. PERFORMING ORG. REPORT NUMBER
7. AUTHOR(s) William F. Gabriel		8. CONTRACT OR GRANT NUMBER(s)
9. PERFORMING ORGANIZATION NAME AND ADDRESS Naval Research Laboratory Washington, D.C 20375		10. PROGRAM ELEMENT, PROJECT, TASK AREA & WORK UNIT NUMBERS NRL Problem R08-37 RR021-05-41-5700
11. CONTROLLING OFFICE NAME AND ADDRESS Department of the Navy Naval Air Systems Command Washington, D.C. 20361		12. REPORT DATE July 31, 1974 13. NUMBER OF PAGES 139
14. MONITORING AGENCY NAME & ADDRESS(if different from Controlling Office)		15. SECURITY CLASS. (of this report) Unclassified 15a. DECLASSIFICATION/DOWNGRADING SCHEDULE

16. DISTRIBUTION STATEMENT (of this Report)

Distribution limited to U.S. Government Agencies only; test and evaluation; July 1974. Other requests for this document must be referred to the Director, Naval Research Laboratory, Washington, D.C. 20375.

17. DISTRIBUTION STATEMENT (of the abstract entered in Block 20, if different from Report)

18. SUPPLEMENTARY NOTES

19. KEY WORDS (Continue on reverse side if necessary and identify by block number)

Adaptive arrays
Antennas

20. ABSTRACT (Continue on reverse side if necessary and identify by block number)

A tutorial introduction to adaptive arrays is presented via analysis of linear arrays with adaptive control loops of the Applebaum analog type, which derive weighting adjustment control from the correlations between element signals, i.e., on the basis of the covariance matrix of the set of system inputs.

Phase conjugacy, cross-correlation interferometers, and the IF phase-cancellation principle were reviewed, and a simple two-element array with a single adaptive control loop was analyzed.

(Continued)

DD FORM 1 JAN 73 1473 EDITION OF 1 NOV 65 IS OBSOLETE
S/N 0102-014-6601 |

SECURITY CLASSIFICATION OF THIS PAGE (When Data Entered)

The analysis was based on reduction to a type-0 follower servo equivalent circuit and includes transient behavior, bandwidth effects, and the Applebaum hard-limiter modification.

The analysis then proceeded to a K-element linear array with K adaptive control loops. The system analysis consisted of a Q-matrix transformation into orthonormal eigenvector space, and interpreting the transformation in terms of an orthogonal beam-forming network, similar in principle to a Butler matrix network. The system was thus converted into an equivalent "orthonormal," adaptive control-loop network to which the type-0 follower servo analysis can again be applied.

The Q-matrix transformation network produced a set of K orthogonal, normalized, eigenvector beams whose output powers are proportional to the eigenvalues of the covariance matrix. These beams were used as the basis of a convenient expression for calculating the time-dependent output pattern function for the array. Performance was calculated for eight different distributions of interference sources to demonstrate the effects of power level, source location with respect to the quiescent beam pattern, source spacing in terms of array resolution, source bandwidth, and continuous source distributions. The Applebaum hard-limiter modification was also introduced into the control loops and the performance recalculated.

CONTENTS

AN INTRODUCTION TO ADAPTIVE ARRAYS

BACKGROUND

Airborne early warning (AEW) radar systems operating over land in an electronic countermeasures (ECM) environment are severely troubled by both jamming and clutter [1]. Ground clutter can be very large, typically some 30 dB larger than return from targets of interest, and because of aircraft motion (plus antenna rotation, if present) its power spectrum generally spreads throughout target doppler regions of interest, particularly in low-PRF (pulse repetition frequency) systems. Clutter-cancellation techniques [2] used in present AEW radar cannot overcome the ground-clutter problem, and a performance improvement of more than one order of magnitude is essential.

Adaptive array antenna systems are being considered as a solution to the above serious problems because they can respond to their environment, in real time, in both the spatial domain and the time (doppler) domain to optimize the signal-to-noise ratio for the system [3]. Jammer interference is sensed in the spatial domain, and array pattern nulls are formed in the directions of the interference sources to attenuate their contributions to output noise. Platform motion is sensed in the doppler domain from the frequency spreading of the clutter power, and the array shifts into appropriate separated "phase centers" in the time domain to collapse the clutter spectral spread and permit better cancellation. The optimization achieved by an adaptive array may also result in secondary benefits, including compensation for antenna pattern distortions caused by aircraft structure blockage and scattering effects; compensation for element excitation errors, damaged elements, and radome effects; the possibility of more arbitrary element spacing and arrangement, as in conformal array-mounting designs; and very low sidelobes for antennas on aircraft over large sectors of interest.

1. INTRODUCTION

The term *adaptive array* has been applied to so many different types of processing systems that it is well to define the class of systems to be discussed in this report. For the purposes of this report, an adaptive array is system consisting of an array antenna and a real-time adaptive receiver-processor which, given a beam-steering command, samples its current environment and automatically adjusts itself as a matched filter to optimize the ratio of signal to noise (jamming, clutter, or interference) for the indicated direction, frequency, and time. Adjustment control is accomplished by sensing the correlation between element signals, i.e., on the basis of the covariance matrix of the set of system inputs.

Adaptive arrays as applied to radar systems are a relatively new concept, but they have roots in a number of different fields, including retrodirective and self-focusing RF

Note: Manuscript submitted February 22, 1974.

antenna arrays [4], sidelobe cancellers [5], adaptive filters [6], acoustic or sonar arrays [7,8], and seismic arrays [9,10].

The first real contribution in the RF-antenna field was the retrodirective array invented by L.C. Van Atta in the 1950's. Another major step was the development of phase-lock loop theory and practice, which made possible self-steering arrays. Phase-lock loops can be used to phase coherently add signals from different antenna elements in an array. A further advance allowed the phase-lock loop scheme to produce retrodirectivity; the conjugate phase front required for retrodirectivity is in the lower coherent sidebands. In the early 1960's, a key development came in the form of an IF sidelobe canceller circuit invented by Howells [11]. This type of circuit has been widely used and developed into practical phase-conjugate adaptive filtering devices. Howells, Applebaum, and their coworkers at Syracuse University Research Corporation have so greatly refined and generalized sidelobe canceller analysis and design [12] that it now constitutes one of the most important contributions to adaptive array concepts.

On the basis of the sidelobe canceller experience, Applebaum [13,14] developed a control-law theory (algorithm) for adaptive arrays which maximizes a generalized signal-to-noise (S/N) ratio. He applied the theory in the form of analog adaptive element-control loops. Because of its practical basis, the Applebaum control loop was selected as the model for discussion in this report.

Several other interesting adaptive-array algorithms and techniques are described in the literature. Time did not permit their inclusion herein, but an extensive reference list has been prepared for the interested reader.

This report is intended to be tutorial, and starts out in Sec. 2 by reviewing some basic ideas, namely phase conjugacy, cross-correlation interferometers, and the IF phase-cancellation circuit. Section 3 is an analysis of a simple two-element array that has a single adaptive loop of the Applebaum type. One can get an excellent perspective on adaptive system performance by studying this single-loop behavior, since it is easy to keep track of the various parameters.

The main section of the report is Sec. 4, which is an analysis of a K-element linear array with K adaptive loops of the Applebaum type. An effort is made to interpret the mathematics in terms of beam-forming networks. In particular, a retrodirective-eigenvector-beam concept is employed to aid in visualizing the transient behavior of the adaptive-array output pattern.

2. REVIEW OF SOME BASIC CONCEPTS

2.1 Phase Conjugacy

The adaptive array performs spatial filtering by sensing automatically the direction of a source of interference and forming a retrodirective receive beam in that direction to subtract from its normal (unadapted) pattern. The principle is illustrated in Fig. 1, where "retrodirective beam" denotes the receive beam automatically formed in the direction of a single source of interference. To achieve retrodirectivity [4,15], the phase of each element of the array must be delayed (with respect to a given reference element) by exactly

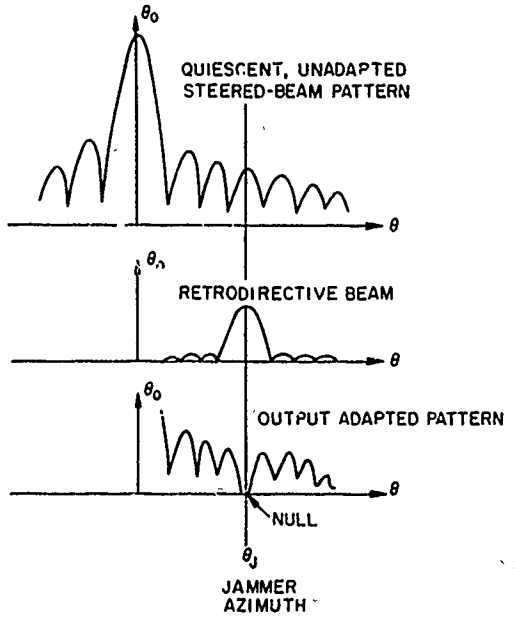

Fig. 1—Retrodirective beam principle of operation for adaptive array, with one interference source

the same amount that the incoming wave was advanced. At any given frequency, time delay may be represented by a phase shift, which may be ambiguous to within $\pm 2n\pi$. Thus, at any element the retrodirective phase must bear a conjugate relationship to the phase of the received signal at that element when compared to a common reference element.

It turns out that phase conjugacy can be obtained very easily by feeding a mixer with a reference signal either equal to or higher in frequency than the received signal, and then choosing the difference frequency as the output. To see this, let us briefly review mixer operation for a typical hot-carrier mixer diode with two input signals, as illustrated in Fig. 2. Define input signals E_1 and E_2 as the real parts of corresponding complex numbers $\bar{E}_1$ and $\bar{E}_2$, where

$$\bar{E}_1 = ae^{j(\omega_1 t+\phi_1)} \quad \text{and} \quad \bar{E}_2 = be^{j(\omega_2 t+\phi_2)} \tag{2.1}$$

$$E_1 = \text{Re}\,(\bar{E}_1) = a\cos(\omega_1 t + \phi_1) \tag{2.2}$$

$$E_2 = \text{Re}\,(\bar{E}_2) = b\cos(\omega_2 t + \phi_2). \tag{2.3}$$

The instantaneous current-voltage relationship for a hot-carrier diode is

$$I = I_s(e^{\alpha v} - 1) \tag{2.4}$$

where

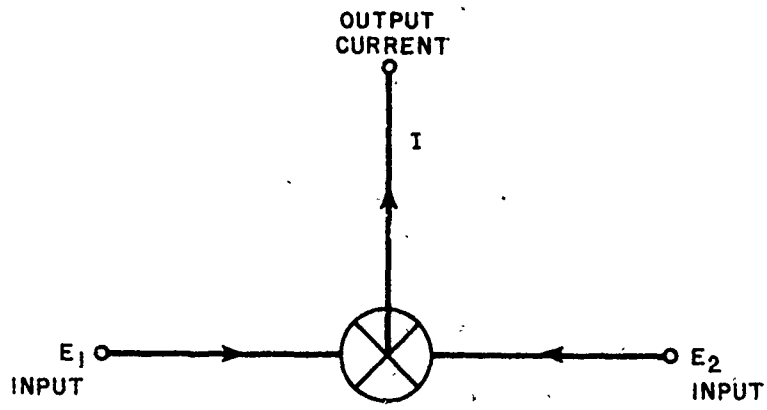

Fig. 2—Diode mixer representation

I_s = reverse saturation current (constant)

$c \approx 38$ (constant)

v = voltage across diode junction.

Next, let

$$v = y - V_b, \tag{2.5}$$

where

V_b = total dc voltage, including self-bias,

and

$$y \approx k_0(E_1 + E_2). \tag{2.6}$$

Voltage y is the RF voltage across the diode junction, with factor k_0 dependent on the particular mixer-circuit parameters. Equation (2.4) may be written as

$$I = -I_s + \left(\frac{I_s}{I_b}\right) e^{\alpha y} \tag{2.7}$$

where $I_b = e^{\alpha V_b}$. By expanding $e^{\alpha y}$ in a power series, one obtains

$$I = -I_s + \left(\frac{I_s}{I_b}\right)\left[1 + \alpha k_0(E_1 + E_2) + \frac{\alpha^2 k_0^2 (E_1 + E_2)^2}{2} + \frac{\alpha^3 k_0^3 (E_1 + E_2)^3}{6} + \ldots\right]. \tag{2.8}$$

An inspection of the power-series terms reveals that total output current I consists of a dc component plus all of the harmonics $n\omega_1$, $m\omega_2$, $(n\omega_1 - m\omega_2)$, and $(n\omega_1 + m\omega_2)$. We are interested only in the linear product of E_1 and E_2, and this product is contained only in the squared term of the series, so from Eq. (2.8) we pick out

$$\frac{I_s\alpha^2k_0^2}{2I_b}(E_1+E_2)^2 = \frac{I_s\alpha^2k_0^2}{2I_b}\left(E_1^2+2E_1E_2+E_2^2\right). \tag{2.9}$$

If we neglect the multiplying factor, the product of E_1 and E_2 in Eq. (2.9) may be written as

$$2(E_1E_2) = 2ab\cos(\omega_1t+\phi_1)\cos(\omega_2t+\phi_2) \tag{2.10}$$

$$2(E_1E_2) = ab\cos[(\omega_1+\omega_2)t+\phi_1+\phi_2] + ab\cos[(\omega_1-\omega_2)t+\phi_1-\phi_2] \tag{2.11}$$

$$2(E_1E_2) = \mathrm{Re}(\bar{E}_1\bar{E}_2) + \mathrm{Re}(\bar{E}_1\bar{E}_2^*) \tag{2.12}$$

where $\bar{E}_2^*$ is the complex conjugate of $\bar{E}_2$ with $\omega_2 \leqslant \omega_1$.

Thus, the sum frequency term corresponds to the simple vector product of $\bar{E}_1$ and $\bar{E}_2$, whereas the difference frequency term results in a product with the complex conjugate of the input of lowest frequency. Note that the complex conjugate must apply to the signal of lowest frequency to obtain the correct direction of vector rotation, i.e., a "positive" difference frequency. The amplitude of the product is proportional to the product of the amplitudes of the two inputs but is also dependent on the mixer-diode parameters and the mixer circuit, as indicated in Eq. (2.9). In the special case in which $\bar{E}_1$ and $\bar{E}_2$ are of the same carrier frequency, $\omega_1 = \omega_2$, the difference frequency is zero (dc output) and the complex conjugate may be applied to either signal.

2.2. Cross-Correlation Interferometer

The adaptive array derives the phase-conjugate element "weights" for forming a retrodirective receive beam by cross-correlating the received element signals with a received reference signal. The reference signal may consist of the output of a separate antenna or the output of the array in which the particular element is located. In either case, the basic principle is that of the cross-correlation interferometer. This is a basic type of antenna, first used in the field of radio astronomy. It is shown in simple, schematic form in Fig. 3 [16,17].

Signals from a single point source at angle θ off boresight arrive at the two antennas A and B with a path-length phase difference of u, where

$$u = \frac{2\pi D}{\lambda}\sin\theta \tag{2.13}$$

with

D = distance between antenna phase centers

λ = wavelength.

These RF signals are translated into a convenient IF band by two mixers fed from a common local oscillator, so that the RF phases and amplitudes are preserved in the IF signals. If we denote the IF signal from antenna B as $\bar{E}_2$, we can write the real part as

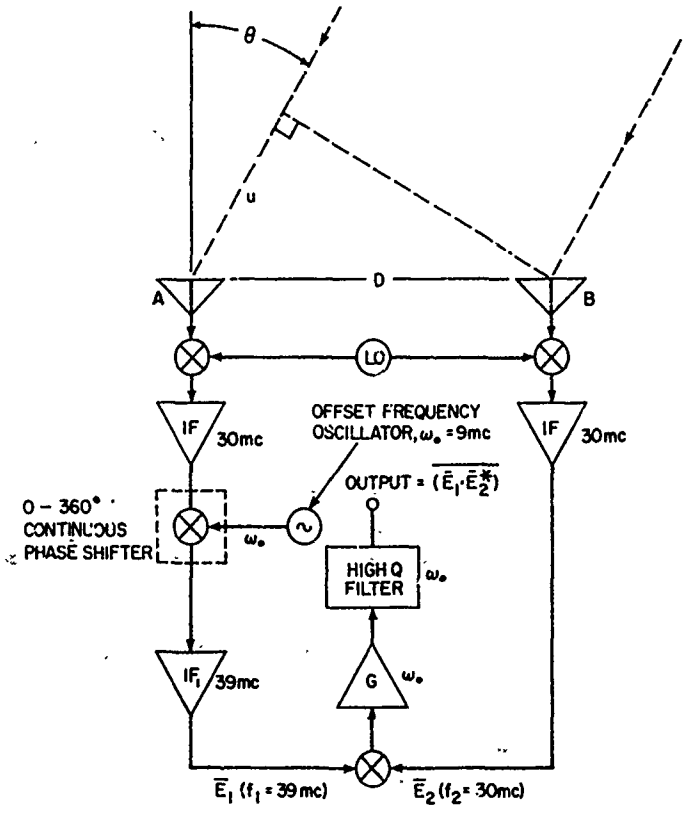

Fig. 3—Simple schematic of cross-correlation interferometer antenna

$$E_2 = b \cos(\omega t + u), \tag{2.14}$$

where b is the amplitude of the signal received at B, ω is the IF angular frequency, and u is the phase advance at B in reference to A. The IF signal from the mixer of antenna A is amplified and then offset to a higher frequency by mixing it with a constant reference offset frequency ω_0 in a second mixer. (The advantages of inserting an offset frequency are discussed later.) Thus, we may express the real part of signal $\bar{E}_1$ as

$$E_1 = a \cos[(\omega + \omega_0)t + \phi_0], \tag{2.15}$$

where a is the amplitude of the signal received at A, $(\omega + \omega_0)$ is its shifted IF angular frequency, and ϕ_0 is a phase constant of the reference offset.

The mixer technique shown in Fig. 3 is only one of several methods that have been used for achieving a frequency offset. Other methods include the following:

1. A Fox-type, 0°–360° RF phase shifter may be continuously rotated [16].

2. If antenna A is circularly polarized (as, for example, a cavity-backed spiral antenna), the antenna itself can be rotated, as in the AN/ASQ-96 DF system.

3. Various electronic serrodyne techniques may be used, such as sawtooth-swept travelling wave tubes, "staircase-driven" digital phase shifters, and upper-sideband amplitude modulators.

The continuous phase-shift rate $\omega_0 t$ introduced by the offset frequency in any of the above techniques results in continuous scanning of the multilobe receive pattern of the interferometer. Lobes scan through a given point-source position at the rate of (ω_0/π) lobes per second.

If signals E_1 and E_2 are combined in the final mixer shown in Fig. 3 and the difference-frequency output is chosen, then from the mixer description given in the previous section the output will be the real part of the product of $\bar{E}_1$ and the complex conjugate of $\bar{E}_2$:

$$\text{Re}\,[\bar{E}_1\bar{E}_2^*] = \frac{ab}{2}\cos(\omega_0 t + \phi_0 - u) \tag{2.16}$$

$$= \frac{ab}{4}\cos u \cos(\omega_0 t + \phi_0) + \frac{ab}{4}\sin u \sin(\omega_0 t + \phi_0).$$

This final mixer operation is a true cross-correlation of the signals received at antennas A and B, with the output having a carrier frequency precisely equal to the reference offset frequency. The amplitude of the output is proportional to the product of the signal amplitudes received at the two antennas. The phase of the output is equal to phase difference u between the signals received at the two antennas, except for the arbitrary phase constant ϕ_0 associated with the reference offset frequency. The constant ϕ_0 can be calibrated out in a standard phase detector, permitting measurement of phase difference angle u, as is done in some applications.

The cross-correlation mixer signal is then amplified in a high-gain amplifier of gain G, with passband centered at offset frequency ω_0, and integrated in a narrowband, high-Q filter to improve the output signal-to-noise ratio. In addition to reducing the noise in the output by narrowing its bandwidth, the filter integrates or averages the correlation mixer output signal. This averaging is denoted symbolically by an upper overall bar:

$$\int_t^{t+\tau} \text{Re}\,[\bar{E}_1\bar{E}_2^*]\,dt = \text{Re}\,\overline{(\bar{E}_1\bar{E}_2^*)}. \tag{2.17}$$

The averaging is very important in adaptive array processing and is discussed in greater detail in later sections. For the moment, it does not change the output as represented by Eq. (2.16) because we are dealing with simple sinusoidal signals in steady state.

Therefore, the cross-correlation interferometer receiver system shown in Fig. 3 results in an output at some convenient reference offset frequency which is a constant complex number, the amplitude of which is proportional to the product of the amplitudes of the signals received at the two antennas, and the phase of which is equal to path-length phase difference u. In addition, the phase of this complex number happens to be the conjugate phase of antenna B with respect to antenna A, so that it constitutes the exact phase angle

required for this two-element array to form a retrodirective lobe pointed toward the signal source.

It is not necessary to inject an offset frequency, since we could get the same output result from a "zero-IF" correlation detector with dc output. However, the dc detector output must contend with all of the other dc voltage terms represented in Eqs. (2.8) and (2.9) and requires balanced mixer networks and differential dc amplifier balancing in order to get rid of the unwanted voltages. This is generally very troublesome in low-level dc detection and requires continual dc drift corrections. Another disadvantage associated with low-level dc detection is the presence of $1/f$ noise (flicker noise).

2.3. IF Phase-Cancellation Mixer

The next step is to add to the cross-correlation interferometer a phase-cancellation mixer as shown in Fig. 4 (based on Ref. 11). The output of the averaging filter is denoted as complex weight $\overline{W}$ and its steady-state value is gain G times the averaged cross-correlator output from Eq. (2.16):

$$\overline{W} = kG(\overline{\overline{E}_1\overline{E}_2^*}) \tag{2.18}$$

$$W = \mathrm{Re}\,(\overline{W}) = k\,ab\,G\cos(\omega_0 t + \phi_0 - u)\,, \tag{2.19}$$

where k is a constant representing the correlation—mixer conversion factor. The constant k can be further defined, from constants given in Eq. (2.9), as

$$k \approx \frac{I_s\alpha^2 k_0^2}{2I_b}\,R_m\,, \tag{2.20}$$

where R_m represents the mixer circuit load resistance. The constant k has units of volts^{-1}, such that $k(\overline{E}_1\overline{E}_2^*)$ will have the expected units of volts.

Weight $\overline{W}$ and signal $\overline{E}_2$ are fed into the additional mixer, and the sum frequency output, denoted by

$$\overline{E}_3 = k(\overline{W}\overline{E}_2) = k^2G(\overline{\overline{E}_1\overline{E}_2^*})\overline{E}_2\,, \tag{2.21}$$

is chosen so that the product of $\overline{E}_2$ and the averaged cross-correlator output is obtained. In the case of simple sinusoids, as represented in Eq. (2.16), there is no envelope modulation to average, and $\overline{E}_2$ can be directly multiplied into its own complex conjugate, thus changing Eq. (2.21) into

$$\overline{E}_3 = k^2G|\overline{E}_2|^2\overline{E}_1 \tag{2.22}$$

or

$$E_3 = \mathrm{Re}\,(\overline{E}_3) = k^2b^2Ga\cos[(\omega + \omega_0)t + \phi_0]\,. \tag{2.23}$$

The net result is that the phase of the $\overline{E}_2$ signal is automatically cancelled, and the output is precisely in phase with offset signal $\overline{E}_1$. Also, it should be noted that the amplitude of E_3 is proportional to the received element power.

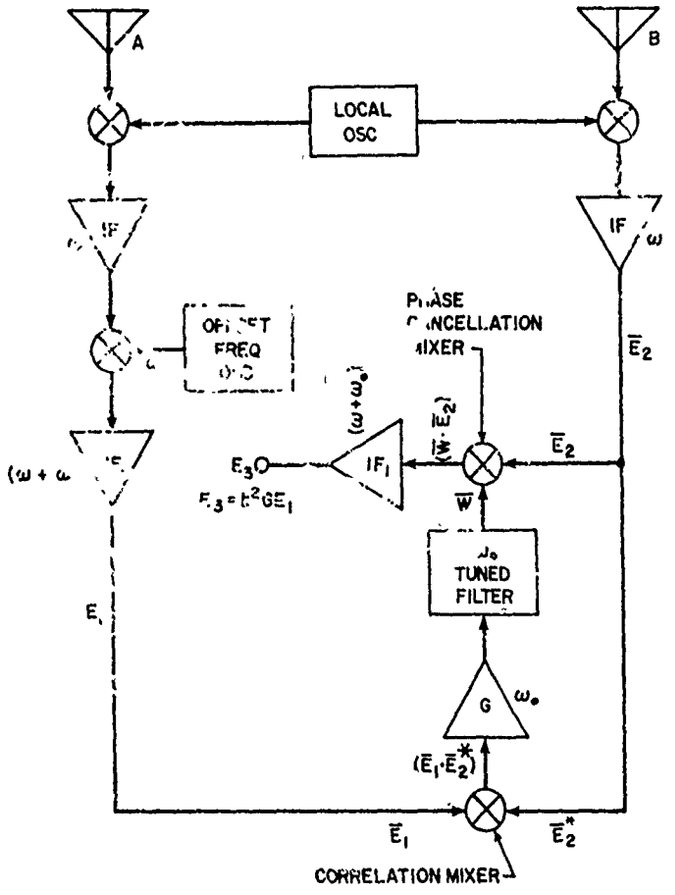

Fig. 4—Cross-correlation interferometer with IF phase-cancellation mixer added

In the general case where $\bar{E}_1$ and $\bar{E}_2$ are broadband envelope-modulated signals, phase φ is slightly different for each spectral line and weight $\bar{W}$ represents an average conjugate phase of $\bar{E}_2$ relative to $\bar{E}_1$. Thus, the product of $\bar{E}_2$ with $\bar{W}$ would not result in complete phase cancellation across the band, and the output would be slightly different from $\bar{E}_1$.

2.4 Integrating Filter Considerations

Section 2.2 briefly discussed the steady-state output of the integrating filter, but there are other aspects to examine. For convenience, consider the single-tuned *RLC* filter circuit shown in Fig. 5. This can be analyzed via the usual Laplace-transform approach [18], starting with the integrodifferential equation of the circuit,

$$\frac{W}{R} + C\,\frac{dW}{dt} + \frac{1}{L}\int W\,dt = \frac{v}{R}, \tag{2.24}$$

where v is an input step-function sinusoid, and

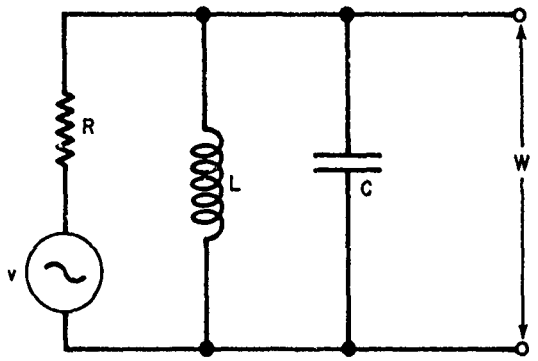

Fig. 5—Single-tuned *RLC* filter circuit for *W*

$$v = 0 \qquad \text{for} \quad t < 0$$

$$v = \frac{abG}{2} \sin(\omega_0 t + \phi_0 - u) \qquad \text{for} \quad t \geqslant 0. \tag{2.25}$$

The necessary manipulations are contained in Appendix A, where W is found to be

$$W = abG[e^{-\alpha t} A \cos(\beta t + \psi) + B \sin(\omega_0 t + \theta)]. \tag{2.26}$$

The various quantities are defined in Appendix A. Equation (2.26) consists of the usual transient term plus a steady-state term. Examination of the expressions for B and θ shows that the steady-state term will not be identical to the input sinusoid unless the circuit resonance is tuned exactly equal to ω_0, whereupon $\theta = (\phi_0 - u)$ and $B = 1/2$. Otherwise, the filter circuit introduces a constant phase shift.

The transient term is a decaying sinusoid of frequency β nearly equal to ω_0, since we assume a high-Q filter, and the exponential decay is governed by

$$\alpha = \frac{1}{\tau} = \frac{1}{2RC}, \tag{2.27}$$

where τ is the circuit time constant or equivalent integration time.

In adaptive arrays it is desirable to be able to control the time constant, yet not introduce extra phase shifts, which would interfere with proper operation of the phase-cancellation mixer shown in Fig. 4. The *RLC* circuit relationships indicate that this may be difficult, and in practice this has been found to be the case. Thus, tuned-carrier integrating filters are not very desirable here. A compromise solution is to convert down from offset frequency ω_0 to dc baseband I and Q channels (in phase and quadrature) at the output of the ω_0 amplifier. The integrating filter can then be a simple *RC* type. Such a compromise is shown in Fig. 6. It attempts to retain the "best of both worlds"; i.e., it retains the offset frequency output from the cross-correlation mixer in order to keep the offset detection advantages noted in Sec. 2.2, and after amplification it converts to high-level dc in order to take advantage of the simpler *RC* integrating filter circuits, which avoid unwanted phase-shift problems and permit easy control of time constants.

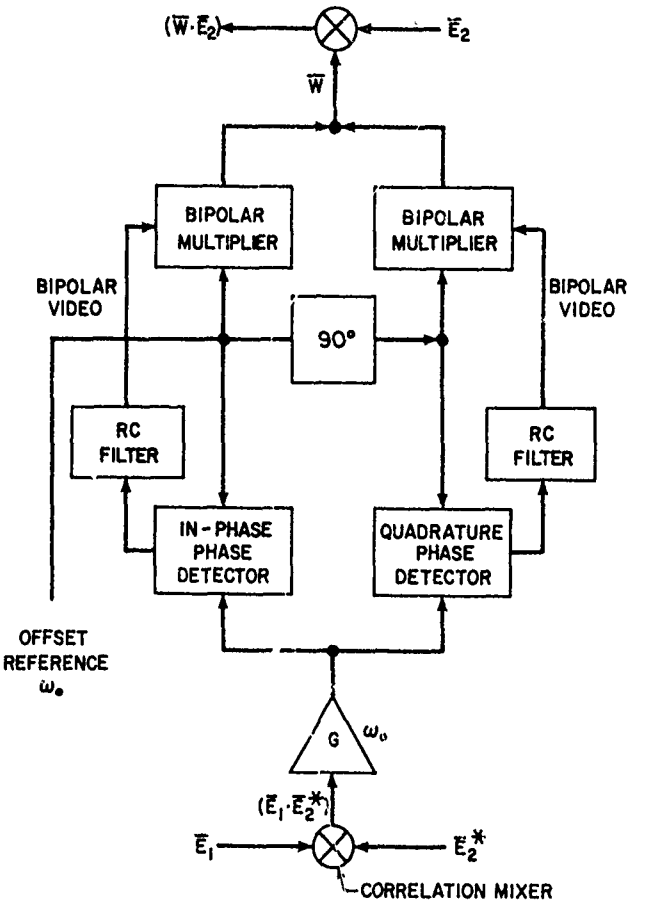

Fig. 6—Technique for using simple *RC* integrator filters

The arrangement shown in Fig. 6 uses the I and Q bipolar video from the RC filters to remodulate the offset reference signal and reestablish weight $\bar{W}$ at the offset frequency ω_0 prior to mixing with $\bar{E}_2$.

For the rest of this report, it is assumed that the integrating filter is of the RC type, as in Fig. 6, and our filter transient analysis therefore can be based on the simple RC circuit shown in Fig. 7. The differential equation will be

$$\frac{W}{R} + C\,\frac{dW}{dt} = \frac{v}{R} \tag{2.28}$$

or

$$\tau_0\,\frac{dW}{dt} + W = v, \tag{2.29}$$

where $\tau_0 = RC$ is the circuit time constant and v is an input step-function dc voltage;

$$\begin{aligned} v &= 0 \quad \text{for} \quad t < 0 \\ v &= v_0 \quad \text{for} \quad t \geq 0. \end{aligned} \tag{2.30}$$

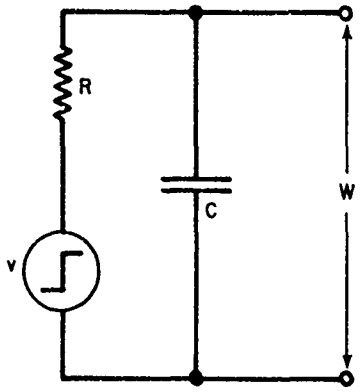

Fig. 7—Simple *RC* integrator filter

Taking the Laplace transform of Eq. (2.29), we get

$$\tau_0 SW(S) - \tau_0 W(0) + W(S) = \frac{v_0}{S} \tag{2.31}$$

or

$$W(S) = \frac{W(0)}{(S + \alpha_0)} + \frac{\alpha_0 v_0}{S(S + \alpha_0)}, \tag{2.32}$$

where $\alpha_0 = 1/\tau_0$, and $W(0)$ is the initial value of voltage W at time $t = 0$. Taking the inverse Laplace transform results in

$$W = W(0)e^{-\alpha_0 t} + v_0(1 - e^{-\alpha_0 t}) \tag{2.33}$$

or

$$W = [W(0) - v_0]\, e^{-\alpha_0 t} + v_0 . \tag{2.34}$$

Since we could do this separately for the I and Q filters, it is obvious that Eq. (2.34) can be written in terms of the entire complex numbers $\overline{W}$ and $\overline{v}_0$, so that

$$\overline{W} = [\overline{W}(0) - \overline{v}_0]\, e^{-\alpha_0 t} + \overline{v}_0 . \tag{2.35}$$

This gives us a simple transient equation for complex weight $\overline{W}$ representing the I and Q components of the bipolar video coming out of the integrating *RC* filters.

3. TWO-ELEMENT ARRAY WITH SINGLE ADAPTIVE LOOP

The first adaptive array configuration to be discussed consists of a simple two-element array with a single Applebaum loop (Fig. 8). It is schematically similar to the single-loop sidelobe canceller described in Refs. 11 and 19, except that a beam-steering signal is added, as described in Ref. 13. The most significant difference between Fig. 8 and Fig. 4 is the addition of a summing junction in which W_2E_2 is added to W_1E_1, with the sum then becoming the output and being fed back to the correlation mixer. The arrangement

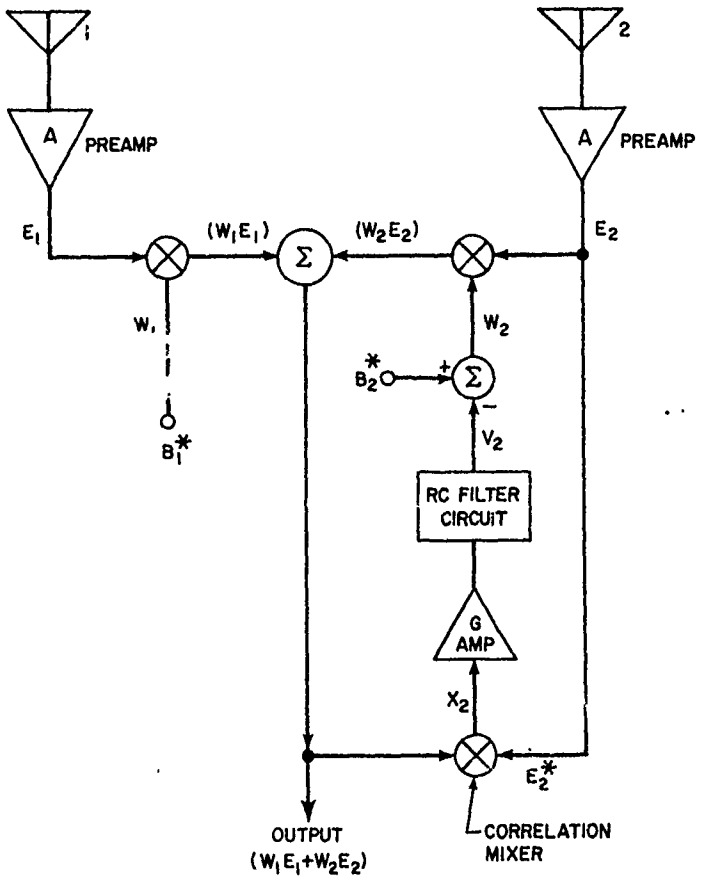

Fig. 8—Two-element array with a single adaptive loop

is intended to result in a negative-feedback servo loop. For the sake of simplicity, Fig. 8 does not show the local oscillator, IF buffer amplifiers, and bandpass filters of an actual system. These are not essential to the analysis at this point.

Beam-steering signals B_1^* and B_2^* are intended to steer the receive beam in some desired azimuth direction θ_0. For quiescent conditions wherein only receiver noise is present, adaptive weight W_2 will settle to a steady-state value denoted by quiescent weight W_q. We want W_q and W_1 to be precisely equal to the weight values needed to point the beam in direction θ_0. Thus, define W_1 and W_q as those desired values with unit amplitudes, such that

$$W_1 = e^{ju_0} \quad \text{and} \quad W_q = W_1^* = e^{-ju_0} \tag{3.1}$$

where

$$u_0 = \frac{\pi d}{\lambda} \sin \theta_0 \,. \tag{3.2}$$

The quantity u_0 is defined on the basis of a reference phase point midway between the phase centers of the two elements, which are spaced apart by distance d. These weights result in quiescent beam pattern $G_q(\theta)$, such that

$$G_q(\theta) = \frac{1}{2}\left[e^{j(u-u_0)} + e^{-j(u-u_0)}\right] = \cos(u-u_0), \tag{3.3}$$

where

$$u = \frac{\pi d}{\lambda}\sin\theta\,; \tag{3.4}$$

θ is the far-field angle variable.

Weight W_1 is injected directly by the beam-steering signal B_1^*, so

$$B_1^* = W_1 = e^{ju_0}. \tag{3.5}$$

Beam-steering signal B_2^*, however, is related to W_q through constant b_2, as

$$B_2^* = b_2 W_q = b_2 e^{-ju_0}. \tag{3.5}$$

This constant will be evaluated later. B_1^* and B_2^* are injected at some reference offset ω_0, but the $e^{j\omega_0 t}$ carrier term is not included since it would be only an extra nonessential quantity to be carried along. In fact, we assume in this discussion that all signals have bandpass frequency spectra which are represented by their complex envelopes, and RF or IF carrier modulated by that envelope will be assumed; i.e., it will not appear explicitly in any of the equations to follow.

Define element signals E_1 and E_2 as consisting of quiescent receiver channel noise voltages n_1 and n_2 plus a statistically independent noisy voltage J_i arising from a single external interference source located at angle θ_i. It is assumed that the source of interference is narrowband unless otherwise stated and that the source is suddenly switched on at time $t = 0$ in a step-function manner. Thus,

$$\left.\begin{aligned} E_1 &= n_1 \\ E_2 &= n_2 \end{aligned}\right\} \quad \text{for} \quad t < 0 \text{ (quiescent)} \tag{3.6}$$

$$\left.\begin{aligned} E_1 &= n_1 + J_i e^{-ju_i} \\ E_2 &= n_2 + J_i e^{ju_i} \end{aligned}\right\} \quad \text{for} \quad t \geq 0 \tag{3.7}$$

where

$$u_i = \frac{\pi d}{\lambda}\sin\theta_i. \tag{3.8}$$

3.1. Equations for Weights W_2 and W_{02}

Weight W_2 is equal to the beam-steering signal B_2^* for element No. 2, minus the output V_2 of the correlator:

$$W_2 = B_2^* - V_2 . \tag{3.9}$$

The correlator consists of the mixer, amplifier, and filter. Its transient behavior may be solved for on the basis of the simple RC filter approach used in Sec. 2.4, provided that the input voltage can be represented as a suitable step function over time. Now the output from the correlation mixer,

$$x_2 = k^2(W_1E_1 + W_2E_2)E_2^* , \tag{3.10}$$

has very rapid rms fluctuations in accordance with the receiver channel passband. The filter, however, integrates or averages these rapid rms fluctuations in accordance with its closed-loop characteristics. The important criterion for our purposes is to have this averaged value $\bar{x}_2$ of the mixer voltage represent an input step function. Thus, assume that $\bar{x}_2$ remains constant with respect to time except for the step-function change occurring at time $t = 0$, which implies that the averaged rms values of the element signals must obey this step-function property in the analysis to follow:

$$\begin{aligned} \bar{x}_2 &= \overline{k^2(W_1E_1 + W_2E_2)E_2^*} \\ &= k^2W_1(\overline{E_1E_2^*}) + k^2W_2|\bar{E}_2|^2 \\ &= k^2W_1(\overline{E_1E_2^*}) + k^2|\bar{E}_2|^2(B_2^* - V_2) . \end{aligned} \tag{3.11}$$

Voltage V_2 obeys the RC filter differential equation, Eq. (2.27), discussed in Sec. 2.4. Under the above assumption regarding averaged values, this may be written as

$$\tau_0 \frac{dV_2}{dt} + V_2 = G\bar{x}_2 . \tag{3.12}$$

Substituting Eq. (3.11) into Eq. (3.12) and rearranging yields

$$\tau_0 \frac{dV_2}{dt} + \left(1 + k^2G|\bar{E}_2|^2\right)V_2 = k^2G|\bar{E}_2|^2\left[B_2^* + \frac{W_1(\overline{E_1E_2^*})}{|\bar{E}_2|^2}\right]. \tag{3.13}$$

For a step-function change in $(E_1E_2^*)$ and $|\bar{E}_2|$, Eq. (3.13) yields for V_2 the solution

$$V_2 = [V_2(0) - V_2(\infty)]\,e^{-\alpha t} + V_2(\infty) , \tag{3.14}$$

where

$$V_2(\infty) = \frac{k^2 G|\bar{E}_2|^2 \left[B_2^* + \dfrac{W_1(\overline{E_1 E_2^*})}{|\bar{E}_2|^2} \right]}{1 + k^2 G|\bar{E}_2|^2} \tag{3.15}$$

and

$$\alpha = \frac{1 + k^2 G|\bar{E}_2|^2}{\tau_0}. \tag{3.16}$$

The quantity $V_2(0)$ is the initial value of voltage V_2 at time $t = 0$, and $V_2(\infty)$ is the steady-state value after the transient has died out. This solution for V_2 is substituted into Eq. (3.9) to get weight W_2.

The quantity W_{02} is defined as the optimum value of weight W_2; it is that value which minimizes the output noise power of the array. The output noise power is the sum of the quiescent receiver noise plus the external interference noise, weighted by array weights W_1 and W_2. If Y_n is the array output noise voltage, the expression to be minimized is the mean square of Y_n, or

$$|Y_n|^2 = |(W_1 E_1) + (W_2 E_2)|^2 . \tag{3.17}$$

We see by inspection that the optimum value of W_2 needed to minimize Eq. (3.17) is

$$W_{02} = -\frac{(W_1 E_1)E_2^*}{|E_2|^2} = -\frac{W_1(E_1 E_2^*)}{|E_2|^2}. \tag{3.18}$$

Incorporating the assumptions regarding averaged values for the element signals results in

$$W_{02} = -\frac{W_1(\overline{E_1 E_2^*})}{|\bar{E}_2|^2}. \tag{3.19}$$

Recalling the discussion in Sec. 2.2, we note that W_{02} is the normalized retrodirective weight which will place a perfect spatial pattern null in the direction of an external source of interference.

Returning to Eq. (3.15), we note that the relationship for W_{02} is contained therein, so that the steady-state output of the correlator may be rewritten as

$$V_2(\infty) = \frac{k^2 G|\bar{E}_2|^2 (B_2^* - W_{02})}{1 + k^2 G|\bar{E}_2|^2}. \tag{3.20}$$

3.2. Servo-loop Considerations

The adaptive loop in Fig. 8 exhibits behavior similar to that of a Type 0 follower servo [20], a simple example of which is shown in Fig. 9a. This uni.. feedback circuit is inherently stable and could represent, for example, a cathode follower or an emitter follower. If the same approach is used as in Sec. 2.4, the equation for the circuit may be written

$$\tau_0 \frac{dv_0}{dt} + v_0 = \mu\epsilon = \mu(v_i - v_0)$$

or

$$\tau_0 \frac{dv_0}{dt} + (1+\mu)v_0 = \mu v_i . \tag{3.21}$$

For a v_i input step function, the solution for v_0 will be found to be

$$v_0 = \left[v_0(0) - \left(\frac{\mu v_i}{1+\mu}\right)\right] e^{-\alpha t} + \frac{\mu v_i}{1+\mu} \tag{3.22}$$

where

$$\alpha = \frac{1+\mu}{\tau_0}. \tag{3.23}$$

If the above equations are compared with Eqs. (3.13), (3.14), (3.16), and (3.20), it is obvious that there are direct correspondences between

$$v_0 \quad \text{and} \quad V_2 ,$$

$$\mu \quad \text{and} \quad k^2 G|\bar{E}_2|^2 ,$$

and

$$v_i \quad \text{and} \quad (B_2^* - W_{02}) .$$

Based on this correspondence, the adaptive loop of Fig. 8 can be modeled by the equivalent servo loop shown in Fig. 9b, whereupon the equations associated with weight W_2 simplify to the following set:

$$W_2 = B_2^* - V_2 \tag{3.24}$$

$$V_2 = [V_2(0) - V_2(\infty)]\, e^{-\alpha t} + V_2(\infty) \tag{3.25}$$

$$V_2(\infty) = \frac{\mu}{1+\mu}(B_2^* - W_{02}) \tag{3.26}$$

$$\alpha = \frac{1+\mu}{\tau_0} \tag{3.27}$$

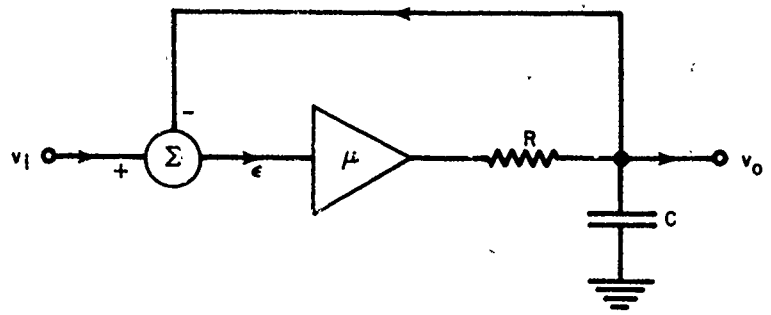

(a) Type 0 follower servo

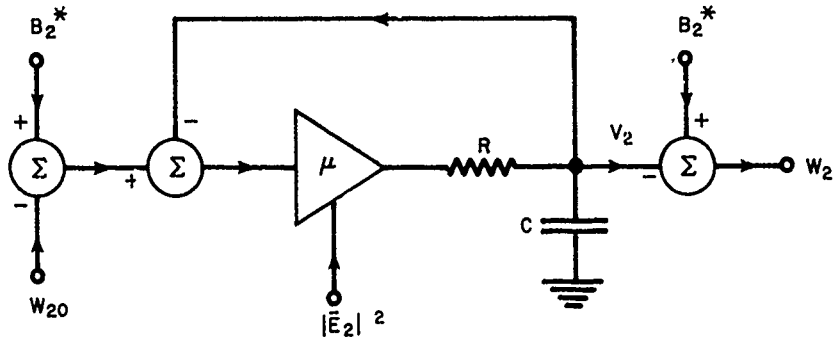

(b) Equivalent circuit of single adaptive loop

Fig. 9—Servo loop schematic diagrams

$$W_{02} = -\frac{W_1\overline{(E_1 E_2^*)}}{|\bar{E}_2|^2} \tag{3.28}$$

$$\mu = k^2 G|\bar{E}_2|^2 . \tag{3.29}$$

This equivalent servo concept is very interesting because it uses the optimum weight as its input signal, and the degree to which the output approaches optimum then depends on servo gain factor μ. Note that for $\mu >> 1$, the steady-state value of W_2 is equal to W_{02}. It is also important to note that the equivalent servo gain factor, as defined in Eq. (3.29), is proportional to the average power level from element No. 2. Two consequences of this peculiar power-sensitive gain behavior are that it is necessary to establish a minimum value for μ, based on quiescent receiver noise power, and a maximum value, based on the maximum interference power to be received at the elements.

Addressing the minimum condition first, we would have E_2 equal to quiescent receiver noise voltage n_2 at the mixers, or

$$\text{minimum } \mu = \mu_0 = k^2 G|\bar{n}_2|^2 \tag{3.30}$$

By choosing an appropriate value for amplification gain G, we can set the value of μ_0 as desired. For example, a convenient choice might be unity. Therefore, the gain will be defined, on the basis of Eq. (3.30), as

$$G = \frac{\mu_0}{k^2|\bar{n}|^2}. \tag{3.31}$$

The quantity $k^2|\bar{n}_2|^2$ represents the voltage coming out of the correlation mixer due to n_2 alone, and since it is proportional to power rather than voltage, it is important to use enough preamplification to ensure its dominance over the thermal noise voltage generated at that mixer. This is not an insignificant problem, as can be seen by examining the two magnitudes. The available thermal noise power at the mixer will be KT_0B_0, where

K = 1.38×10^{-23} J/K (Boltzmann's constant),

T_0 = equivalent noise temperature (K),

and

B_0 = bandwidth of the RC integrating filter.

If we choose typical values of $725K$ for T_0 and 25 cycles for B_0, then the available thermal noise voltage at the mixer is

$$\sqrt{KT_0B_0} = 5 \times 10^{-10} \text{ volts}. \tag{3.32}$$

By comparison, the quiescent receiver noise power referred to the elements would be KT_0B_c, where B_c is the element signal channel bandwidth. Choosing 5 Mc as a typical value for B_c, we have

$$\sqrt{KT_0B_c} = \sqrt{5} \times 10^{-7} \text{ volts}, \tag{3.33}$$

and n_2 represents this voltage after preamplification by some gain A, or

$$n_2 = A\sqrt{KT_0B_c} = A\sqrt{5} \times 10^{-7} \text{ volts}. \tag{3.34}$$

Thus, the correlation mixer voltage due to n_2 alone will be

$$k^2(W_qE_2E_2^*) = k^2W_q|\bar{n}_2|^2 = k^2W_qA^2\ 5 \times 10^{-14} \text{ volts}. \tag{3.35}$$

Since the amplitude of W_q is unity, the magnitude of Eq. (3.35) is essentially $(k^2|\bar{n}_2|^2)$. Furthermore, the mixer conversion factor k, given in Eq. (2.20), is unlikely to exceed unity by an appreciable amount. Therefore, a considerable preamplification gain A is necessary to ensure the dominance of $k^2|\bar{n}_2|^2$ over the mixer thermal noise level as represented in Eq. (3.32). A preamplification gain on the order of 60 dB is indicated here. Figure 8 shows this necessary preamplification in the schematic form of a single preamplifier for each element. The preamplifiers set the level of n_2, which in turn determines the servoamplifier gain G from Eq. (3.31).

The level of quiescent noise n_2 also determines the magnitude of beam-steering signal B_2^*, as may be seen by taking the steady-state expression for weight W_2, given by Eqs. (3.24) and (3.26):

$$W_2(\infty) = B_2^* - \frac{\mu}{1 + \mu}(B_2^* - W_{02}). \tag{3.36}$$

In the quiescent condition, $E_1 = n_1$ and $E_2 = n_2$. These independent noise voltages have zero average cross-correlation; i.e.,

$$\overline{(n_1 n_2^*)} = 0, \tag{3.37}$$

or W_{02} is zero. Also, the quiescent value of μ is μ_0, so that the quiescent expression for $W_2(\infty)$ becomes

$$\text{quiescent } W_2(\infty) = \frac{B_2^*}{1 + \mu_0} = \frac{b_2}{1 + \mu_0} W_q. \tag{3.38}$$

The quiescent value of $W_2(\infty)$ is equal by definition to quiescent weight W_q defined in Eq. (3.1), or

$$W_q = \left(\frac{b_2}{1 + \mu_0}\right) W_q. \tag{3.39}$$

Therefore

$$b_2 = 1 + \mu_0. \tag{3.40}$$

The amplitude of b_2 is greater than the magnitude of the amplified quiescent voltage coming out of the correlation mixer. Note that the phase of the quiescent correlation voltage output is precisely the same as that of the beam-steering signal, since we have, from Eqs. (3.37) and (3.38),

$$\bar{X}_{q2} = \overline{k^2(W_1 E_1 + W_2 E_2)E_2^*} = \overline{k^2(W_1 n_1 + W_2 n_2)n_2^*} = k^2 W_q |\bar{n}_2|^2$$

or

$$\text{quiescent } \bar{X}_{q2} = k^2 |\bar{n}_2|^2 e^{-ju_0}. \tag{3.41}$$

Then, using the value for gain G from Eq. (3.31), we have, for quiescent V_2,

$$V_{q2} = G\bar{X}_{q2} = \mu_0 e^{-ju_0}, \tag{3.42}$$

and we can doublecheck the quiescent weight

$$W_q = B_2^* - V_{q2} = \left[(1 + \mu_0)e^{-ju_0} - \mu_0 e^{-ju_0}\right] = e^{-ju_0}. \tag{3.43}$$

Next, consider the effect on μ of a steadily increasing interference power level at the elements, in order to establish a maximum gain condition. From Eqs. (3.27) and (3.29) we see that as the power increases, the response/integration time decreases and produces less and less averaging effect until the conditions assumed for the simple transient solution of Eq. (3.13) are no longer valid.

Both μ and W_2 then tend to follow the fast fluctuations in the envelopes of the element signals, causing weight W_2 to become "noisy." Reference 21 presents the theory for control-loop noise and derives expressions for the variance of the array element weights and for the additional noise in the array output due to this element weight fluctuation.

The upper-bound condition for avoiding "noisy loops" is most conveniently stated in terms of bandwidth; i.e., the closed-loop, two-sided bandwidth should not exceed approximately one-tenth the bandwidth of the element signal channels [19]. This ensures enough integration time to average out rapid fluctuations in μ and to permit W_2 to be reasonably independent in a statistical sense from the instantaneous fluctuations of the signal envelopes. For the simple circuit of Figs. 9a and 9b, the closed-loop bandwidth is α, as is easily seen by assuming that v_i and v_0 are sinusoids, whereupon Eq. (3.21) can be written as

$$j\omega\tau_0 v_0 + v_0 = \mu(v_i - v_0)$$

or

$$v_0 = \frac{\mu v_i}{1 + \mu + j\omega\tau_0} \quad . \tag{3.44}$$

The half-power or 3-dB bandwidth point occurs for the condition

$$\omega_3\tau_0 = (1 + \mu) \quad \text{or} \quad \omega_3 = \alpha. \tag{3.45}$$

Thus, if the element signal channel bandwidth is B_c, then the upper-bound condition may be expressed as

$$2\omega_3 = 2\alpha_m = \frac{2\pi B_c}{10} \tag{3.46}$$

or

$$\mu_m = \frac{\pi B_c \tau_0}{10} - 1, \tag{3.47}$$

where μ_m is the upper bound or maximum value permitted for the gain factor.

It is convenient to express μ in terms of μ_0 and a power ratio, and this can be done by noting that when an interference source is present, $|\bar{E}_2|^2$ will be the sum of the squares of the magnitudes of n_2 and the interference source voltage J_i at the mixers, so that

$$|\bar{E}_2|^2 = |\bar{n}_2|^2 + |\bar{J}_i|^2 .$$

Thus

$$\frac{\mu}{\mu_0} = \frac{k^2 G_i |\bar{E}_2|^2}{k^2 G |\bar{n}_2|^2} = \frac{|\bar{n}_2|^2 + |\bar{J}_i|^2}{|\bar{n}_2|^2} = 1 + \frac{|\bar{J}_i|^2}{|\bar{n}_2|^2}. \tag{3.48}$$

The ratio of the squares of the voltage magnitudes is equal to the ratio of interference power to receiver noise power. If this power ratio is denoted by P_i, then, from Eq. (3.48), μ can be expressed in the form

$$\mu = \mu_0(1 + P_i), \tag{3.49}$$

where the gain factor is essentially normalized to the quiescent receiver noise-power level. One can proceed to calibrate servo-loop response according to the practical ratio of interference power to receiver noise power. Substituting Eq. (3.49) into Eq. (3.47) results in

$$\mu_m = \mu_0(1 + P_{im}) = \frac{\pi B_c \tau_0}{10} - 1$$

or

$$\tau_0 = \frac{10}{\pi B_c}(1 + \mu_0 + \mu_0 P_{im}). \tag{3.50}$$

This simple expression relates basic filter time constant τ_0 to the maximum interference power to be handled, since channel bandwidth B_c is generally fixed by the radar-pulse waveform characteristics and cannot readily be changed. For example, choose a maximum interference power condition 40 dB above receiver noise level, and a channel bandwidth of 5 Mc. Then from Eq. (3.50) we get, for $\mu_0 = 1$,

$$\tau_0 = \frac{2 \times 10^{-6}}{\pi}(2 + 10^4)$$

or

$$\tau_0 = 0.00637 \text{ s}.$$

The corresponding filter bandwidth is $(1/2\pi\tau_0)$, or about 25 cycles.

The relationship between servo-loop gain and bandwidth is best illustrated by making a Bode plot [20] as shown in Fig. 10, where the servo-loop gain is plotted as a function of frequency. Loop gain is obtained by cutting the loop at a convenient point, in this case the feedback path, whereupon we get

$$j\omega\tau_0 v_0 + v_0 = \mu\epsilon$$

or

$$\text{loop gain} = \left|\frac{v_0}{\epsilon}\right| = \left|\frac{\mu}{1 + j\omega\tau_0}\right|. \tag{3.51}$$

The breakpoint for the 20-dB-per-decade slope line occurs at $\omega = 1/\tau_0$, the basic *RC* filter bandwidth point, and the intersection of the slope line with the unity gain axis occurs approximately at $\omega = \mu/\tau_0$. The slope-line intersection is a very useful indication of the

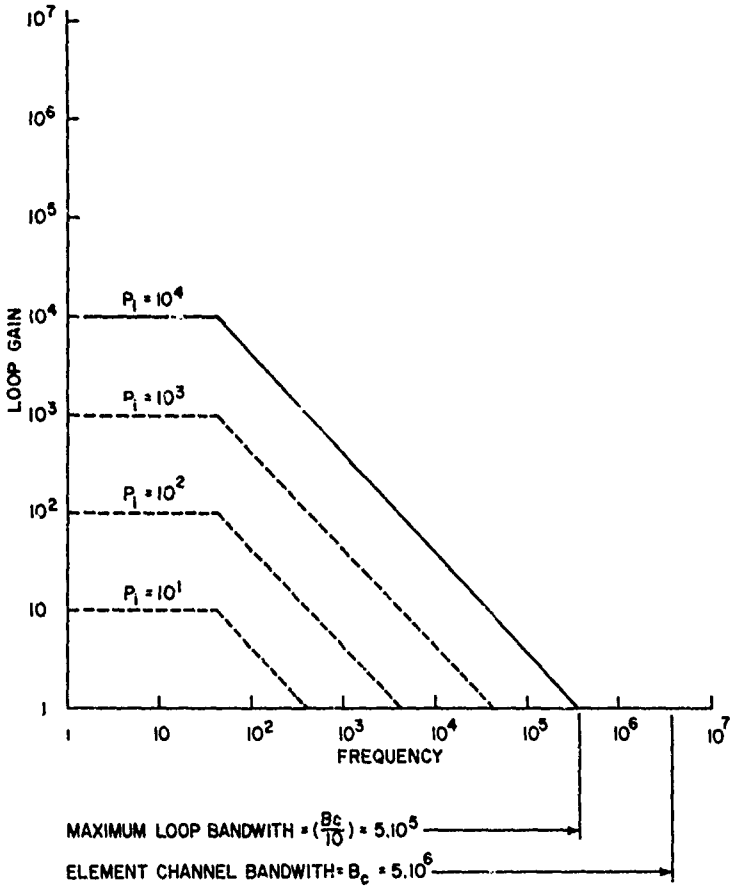

Fig. 10—Bode plot illustrating adaptive loop bandwidth variation with power level

overall 3-dB bandwidth of the servo, which can be verified by referring to Eq. (3.45). Figure 10 shows the Bode plot for interference power ratios of 10 dB, 30 dB, and 40 dB above receiver noise level and is obtained by substituting Eq. (3.49) into Eq. (3.51) to obtain

$$\text{loop gain} = \left| \frac{\mu_0(1 + P_i)}{1 + j\omega\tau_0} \right|. \tag{3.52}$$

3.3. Revised Equations for W_2 and W_{02}

The servo-loop considerations discussed in Sec. 3.2 have introduced so many modifications to the equations developed earlier that it is desirable to consolidate all of these changes into a revised set of equations for W_2 and W_{02}. Starting with the latter, from Eq. (3.19), we first evaluate the averaged cross-correlation products from signals E_1 and E_2, as defined in Eq. (3.7):

$$\overline{(E_1 E_2^*)} = |\bar{J}_i|^2 e^{-j2u_i} \tag{3.53}$$

$$\overline{(E_2 E_2^*)} = |\bar{E}_2|^2 = |\bar{n}_2|^2 + |\bar{J}_i|^2 \tag{3.54}$$

Substituting into Eq. (3.19) results in the convenient expression,

$$W_{02} = \left[- \frac{W_1 \overline{(E_1 E_2^*)}}{|\bar{E}_2|^2} \right]$$

$$= \left[- \frac{W_i |\bar{J}_i|^2 e^{-j2u_i}}{|\bar{n}_2|^2 + |\bar{J}_i|^2} \right]$$

$$= -W_1 \left(\frac{\mu_0}{\mu} \right) P_i e^{-j2u_i} . \tag{3.55}$$

Next, we convert the transient equations in V_2, Eqs. (3.25) and (3.26), over to W_2 by using Eq. (3.24); i.e.,

$$W_2(\infty) = [B_2^* - V_{2\backslash}(\infty)] = \left[\left(\frac{1 + \mu_0}{1 + \mu} \right) W_1^* + \left(\frac{\mu}{1 + \mu} \right) W_{02} \right] \tag{3.56}$$

$$W_2(0) = B_2^* - V_2(0) = W_q = W_1^* , \tag{3.57}$$

where $V_2(0)$ is the quiescent V_{q2} evaluated in Eq. (3.42). Then the transient equation in W_2 becomes

$$W_2 = [W_2(0) - W_2(\infty)] e^{-\alpha t} + W_2(\infty) , \tag{3.58}$$

where

$$\alpha = \frac{1 + \mu}{\tau_0} \quad \text{and} \quad \mu = \mu_0 (1 + P_i) . \tag{3.59}$$

Note that steady-state part $W_2(\infty)$ has two distinct components:

$$\text{beam-steering component} = \frac{B_2^*}{1 + \mu} = \left(\frac{1 + \mu_0}{1 + \mu} \right) W_1^*$$

and

$$\text{retrodirective component} = \left(\frac{\mu}{1 + \mu} \right) W_{02} .$$

When power ratio P_i is close to zero, W_{02} is also close to zero and the beam-steering component is dominant. As P_i increases, μ increases, and the beam-steering component is attenuated while the source retrodirective component increases in magnitude. For large P_i ratios where $\mu >> 1$, the beam-steering component becomes negligible and the source component dominates, essentially "capturing" adaptive weight W_2.

3.4. Adaptive Loop Performance

Initial Conditions and Assumptions—Recall from Eqs. (3.6) and (3.7) that quiescent receiver noise prevails up to time $t = 0$, when a single narrowband interference source is switched on in a step-function manner. Ratio P_i of interference power to receiver noise power is assumed to have a maximum limit of 40 dB. When coupled with a receiver channel bandwidth B_c of 5 Mc and a minimum servo gain factor μ_0 of unity, Eq. (3.50) results in an RC time constant τ_0 of 6,370 μs. Summarizing these conditions, together with G, μ, W_1, B_2^*, and $W_2(0)$, we have

$$\text{maximum } P_i = P_{im} = 10{,}000$$

$$B_c = 5 \text{ Mc}$$

$$\tau_0 = 6{,}370\ \mu s$$

$$\mu_0 = 1$$

$$G = \frac{\mu_0}{k^2|n_2|^2} = \frac{1}{k^2|n_2|^2}$$

$$\mu = \mu_0(1 + P_i) = (1 + P_i)$$

$$W_1 = e^{ju_0}$$

$$B_2^* = (1 + \mu_0)W_1^* = 2e^{-ju_0}$$

$$W_2(0) = W_1^* = e^{-ju_0}.$$

Let us assume that the elements are spaced apart by a half wavelength $d = \lambda/2$, to simplify the expressions for u_0 in Eq. (3.2), u in Eq. (3.4), and u_i in Eq. (3.8).

Transient Behavior of Adaptive Weight W_2—The first performance characteristic of interest is the transient behavior of the adaptive weight W_2. This can be calculated from Eqs. (3.55) through (3.59), using the initial conditions and assumptions listed above.

The transient behavior of W_2 depends on two factors: the obvious power ratio P_i contained in μ and W_{02}, and the less obvious phase-angle rotation which W_2 undergoes in reaching its adapted value. To illustrate the latter factor, Figs. 11a through 11d contain four plots of the amplitude and phase of W_2 vs time, with the same power ratio $P_i = 100$, but with source direction θ_i varied. Starting with Fig. 11a, where the source is directly on boresight ($\theta_i = 0$ degrees), W_2 must undergo a complete 180° phase reversal to place a pattern null where it previously had a maximum, and it will be noted that it does so by rapidly decreasing in amplitude to zero in about 45 μs, abruptly reversing phase 180°, and then increasing in amplitude toward its steady-state value of 0.96. In Fig. 11b the source is 10° off boresight, which requires W_2 to rotate through a phase angle of 148°. For this rotation, the amplitude drops sharply for about 45 μs but does not decrease to zero, and the phase changes smoothly. In Fig. 11c the source is 30° off boresight, which

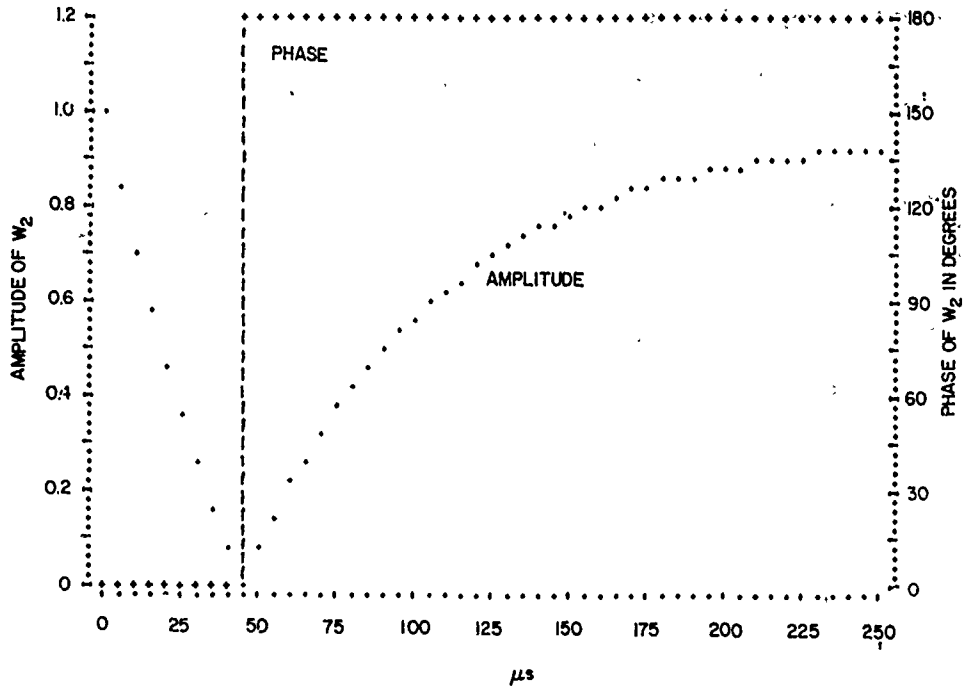

(a) $\theta_I = 0°$

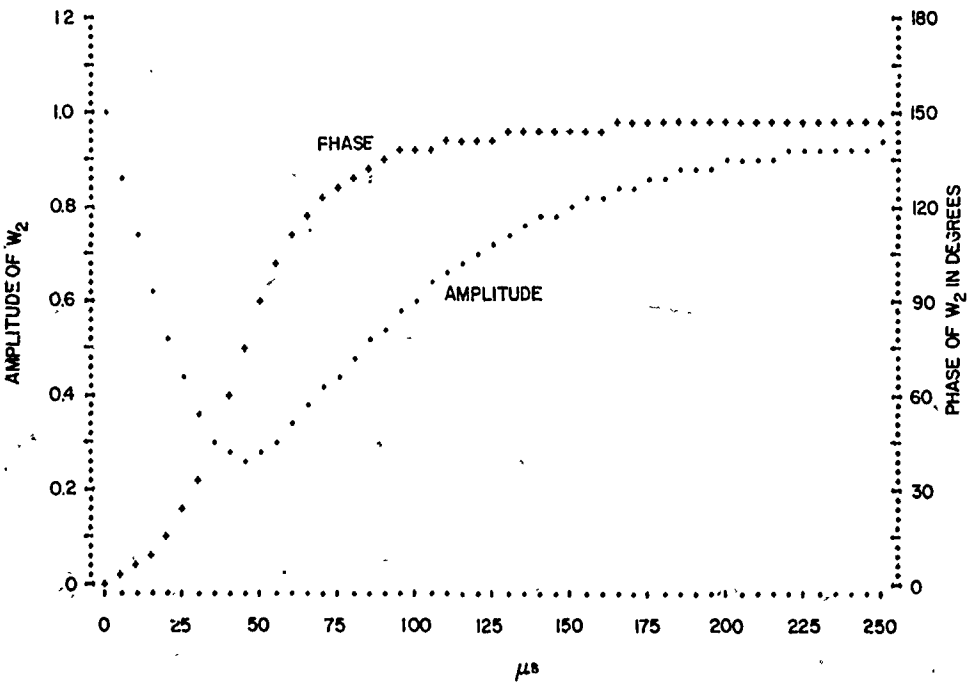

(b) $\theta_I = 10°$

Fig. 11—Transient behavior of W_2 for $P_I = 100$ and $\theta_0 = 0°$

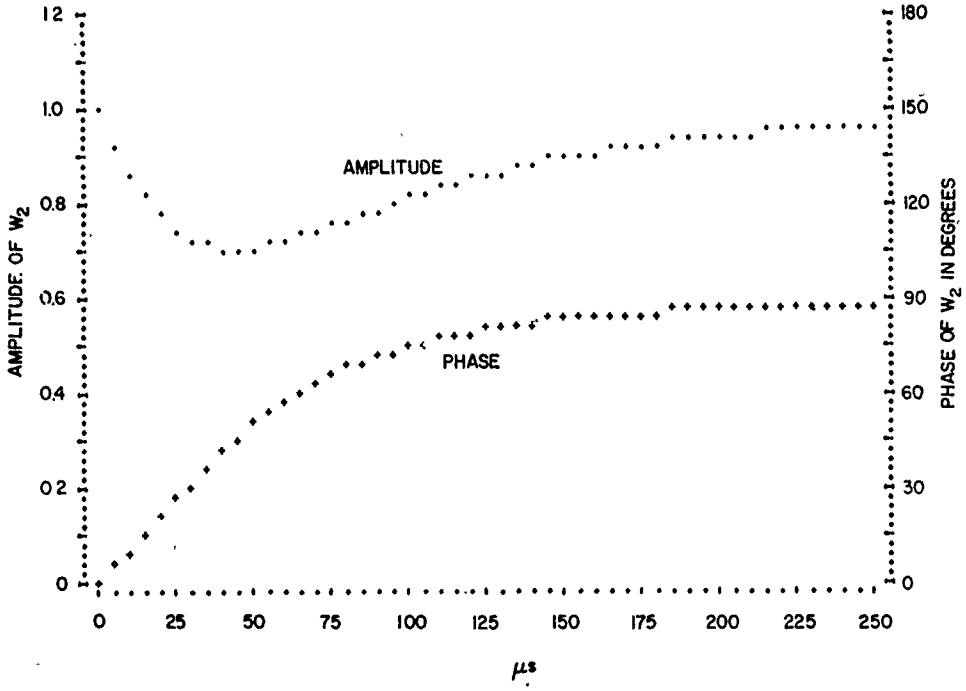

(c) $\theta_i = 30°$

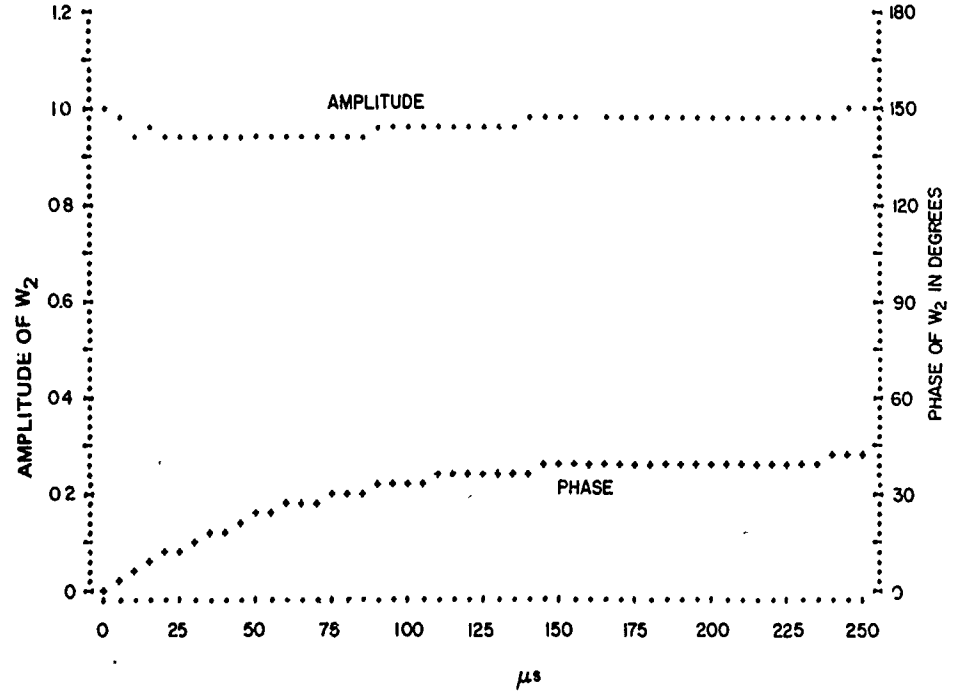

(d) $\theta_i = 50°$

Fig. 11 (Continued)—Transient behavior of W_2 for $P_i = 100$ and $\theta_0 = 0°$

requires W_2 to rotate through a phase angle of 89°. Note that the amplitude dip has now become rather shallow. In Fig. 11d the source is 50° off boresight, which requires W_2 to rotate through a phase angle of only 42°, and here the amplitude varies only slightly from unity. If the source is moved further over into the quiescent pattern null at 90° off boresight, W_2 is already correct in both amplitude and phase, so that no transient would occur.

The effect of changing the power ratio amounts to changing the time scale of the transient, as illustrated in Fig. 12, where we have the same conditions as in Fig. 11b except that the power ratio is now P_i = 1,000. Note that the transient curves are almost identical to Fig. 11b, but the time scale has been reduced by a factor of 10; i.e., the increase in source power level by a factor of 10 has caused the adaptive loop to respond ten times faster in changing W_2.

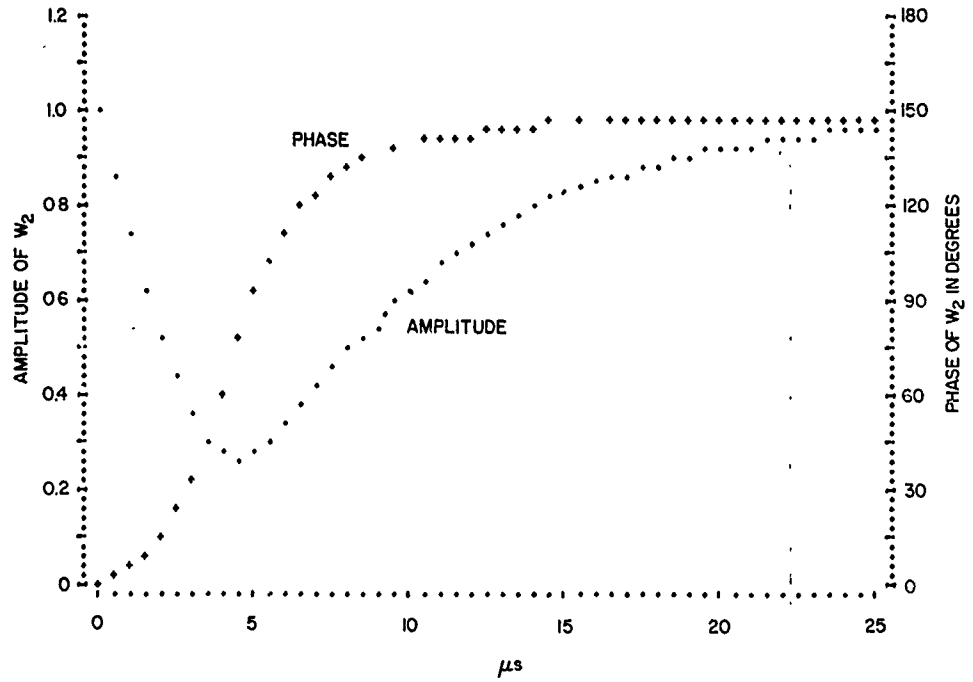

Fig. 12—Transient behavior of W_2 for P_i = 1000, $\theta_0 = 0°$, and $\theta_i = 10°$

Transient Behavior of Spatial Pattern—We easily obtain the behavior of the spatial pattern of our two-element array by "freezing" weight W_2 at various instants of time during its transient change and calculating array output voltage Y produced by a far-field test source of variable spatial angle θ; i.e.,

$$Y = S(W_1 e^{-ju} + W_2 e^{ju}), \tag{3.60}$$

where u is the phase factor defined in Eq. (3.4), and S is the voltage amplitude at the element mixers produced by the test source. As a practical note, it would be necessary to design the test-source signal and receiver system so that the test-source signal would not be sensed by the adaptive loop; otherwise it might influence weight W_2. The spatial-array pattern is proportional to the absolute value of Y, and for convenience in plotting

we generally normalize the function to the maximum value of $|Y|$. Since the maximum value for two elements would be $2S$, the normalized spatial-array pattern function $G(\theta, t)$ becomes

$$G(\theta, t) = \frac{Y}{2S} = \frac{1}{2}(W_1 e^{-ju} + W_2 e^{ju}) \tag{3.61}$$

Figure 13 contains five plots of $|G(\theta), t)|$ under the condition $P_i = 100$ for $t \geq 0$, $\theta_0 = 0°$, and $\theta_i = 15°$. The plots are for time $t = 20$, 50, 100, and 200 μs, and for a steady state. The quiescent, beam-steered pattern at time $t = 0$ is repeated in each plot to serve as the beginning reference. Recall that this quiescent pattern, denoted as $G_q(\theta)$, was defined in Eq. (3.3). It may be verified by substitution of Eq. (3.57) into Eq. (3.61). Thus, starting from this cosine function at $t = 0$ with $\theta_0 = 0°$, the pattern plots demonstrate the progressive development of a pattern null in the direction of a source of interference at $\theta_i = 15°$.

It may be of interest to note that the final steady-state pattern can also be manipulated into a trigonometric expression if the steady-state part of W_2 from Eq. (3.56) is substituted into Eq. (3.61). This yields

$$G(\theta, \infty) = \cos(u - u_0) - \frac{P_i \cos(u_0 - u_i)}{2 + P_i} e^{j(u-u_i)}$$

$$= G_q(\theta) - \frac{P_i G_q(\theta_i)}{2 + P_i} e^{j(u-u_i)}, \tag{3.62}$$

where $G_q(\theta_i)$ is the value of the quiescent, beam-steered pattern function in direction θ_i. Note that for the particular direction $\theta = \theta_i$, $G(\theta, \infty)$ reduces to

$$G(\theta_i, \infty) = \frac{2G_q(\theta_i)}{2 + P_i} = \frac{2\cos(u_i - u_0)}{2 + P_i}, \tag{3.63}$$

which gives us the depth of the pattern null in the direction of the source of interference. For the conditions in Fig. 13, the depth of the null would be about −35 dB, which seems remarkable since P_i is only 20 dB. This excellent null performance occurs because the voltage null in Eq. (3.63) is inversely proportional to power ratio P_i.

Transient Behavior of Output Noise Power—The performance factor of ultimate interest in an adaptive array is the improvement in output signal-to-noise ratio as compared to a conventional array subjected to the same interference conditions. In this ratio, the signal portion can be readily calculated from the change produced in $G(\theta, t)$, as discussed in the previous section. The denominator output noise portion, however, is more fundamental to the improvement that can be obtained and will therefore be treated in some detail in this section and the one to follow.

The output noise power is the sum of the quiescent receiver noise and the interference noise, weighted by array weights W_1 and W_2. From the expressions for signals E_1 and E_2 as given in Eq. (3.7), output noise voltage Y_n may be written as

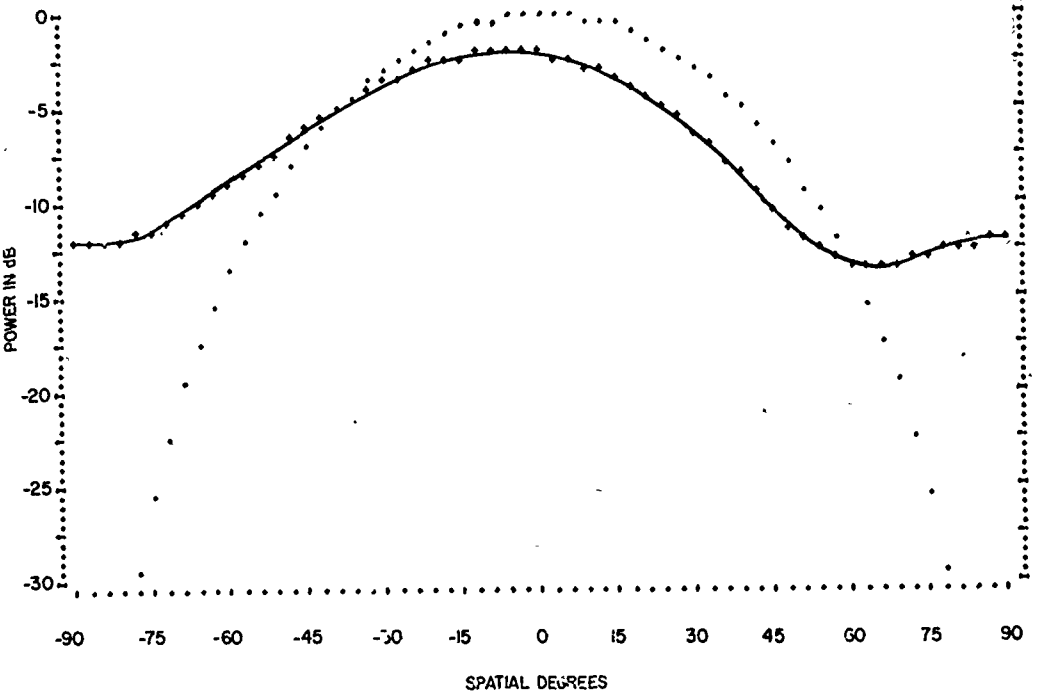

(a) $t = 20\ \mu s$

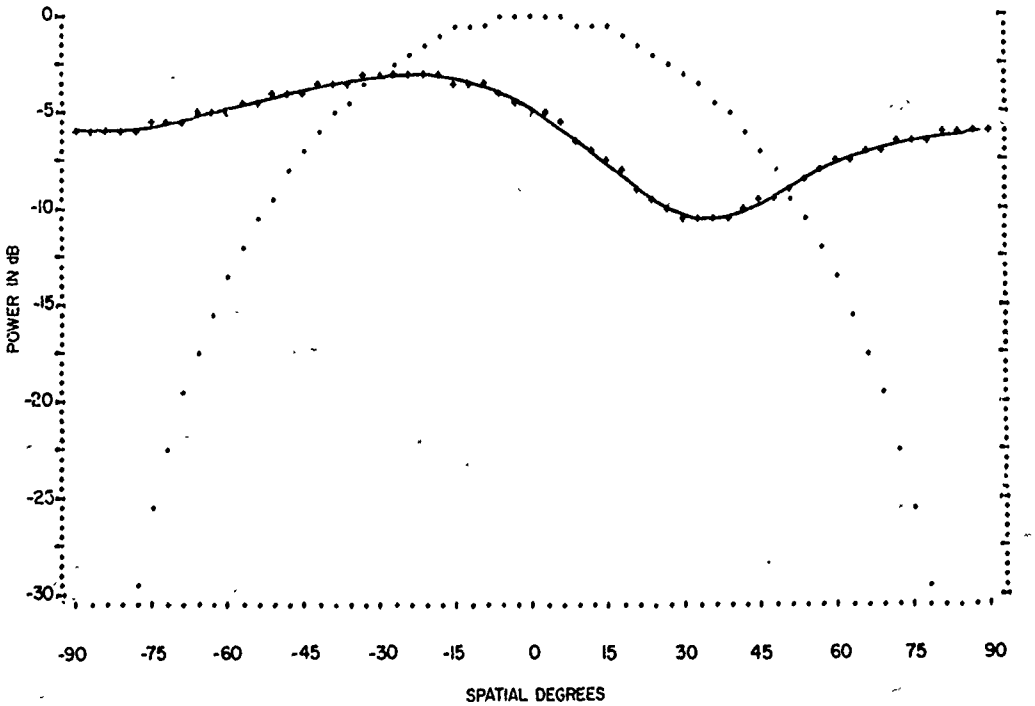

(b) $t = 50\ \mu s$

Fig. 13—Transient behavior of spatial patterns for $P_i = 100$, $\theta_0 = 0°$, and $\theta_i = 15°$

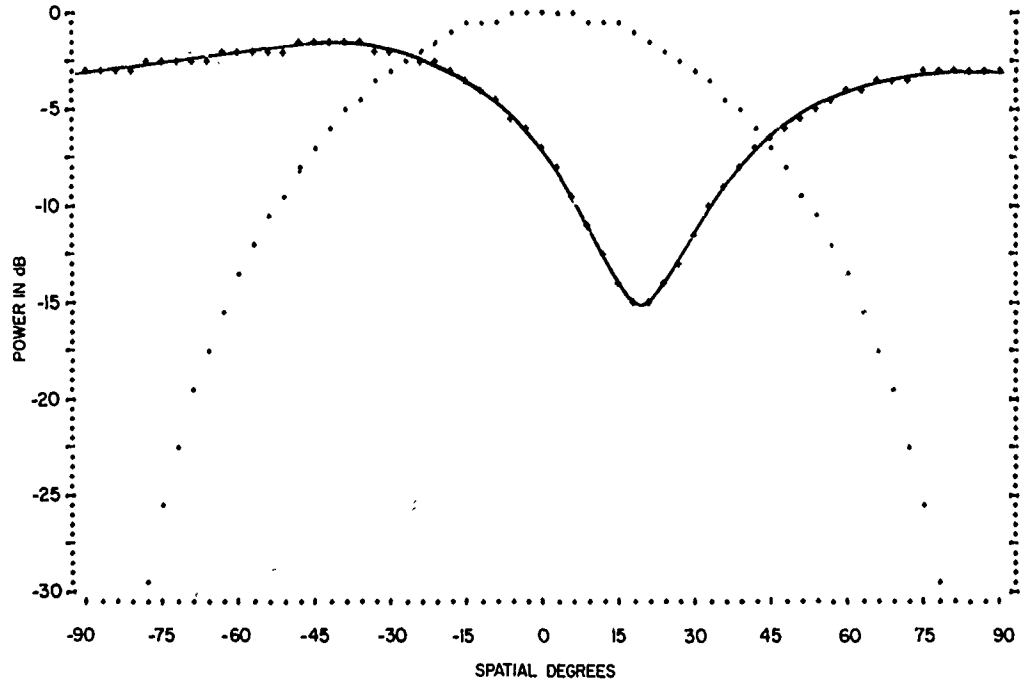

(c) $t = 100\ \mu s$

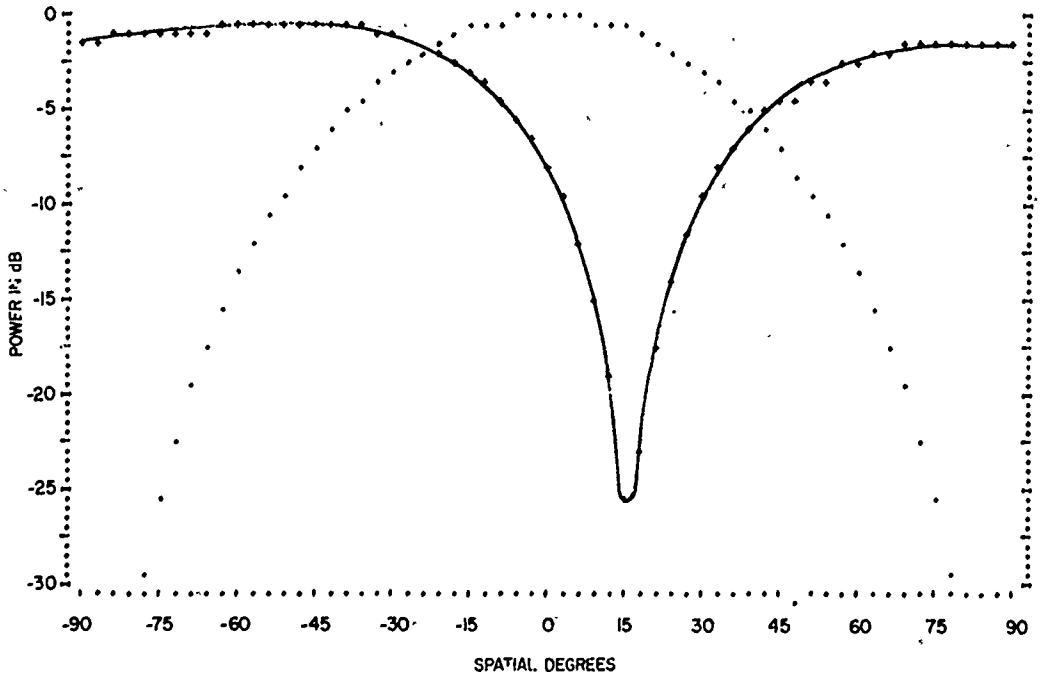

(d) $t = 200\ \mu s$

Fig. 13 (Continued)—Transient behavior of spatial patterns for $P_l = 100$, $\theta_0 = 0°$, and $\theta_l = 15°$

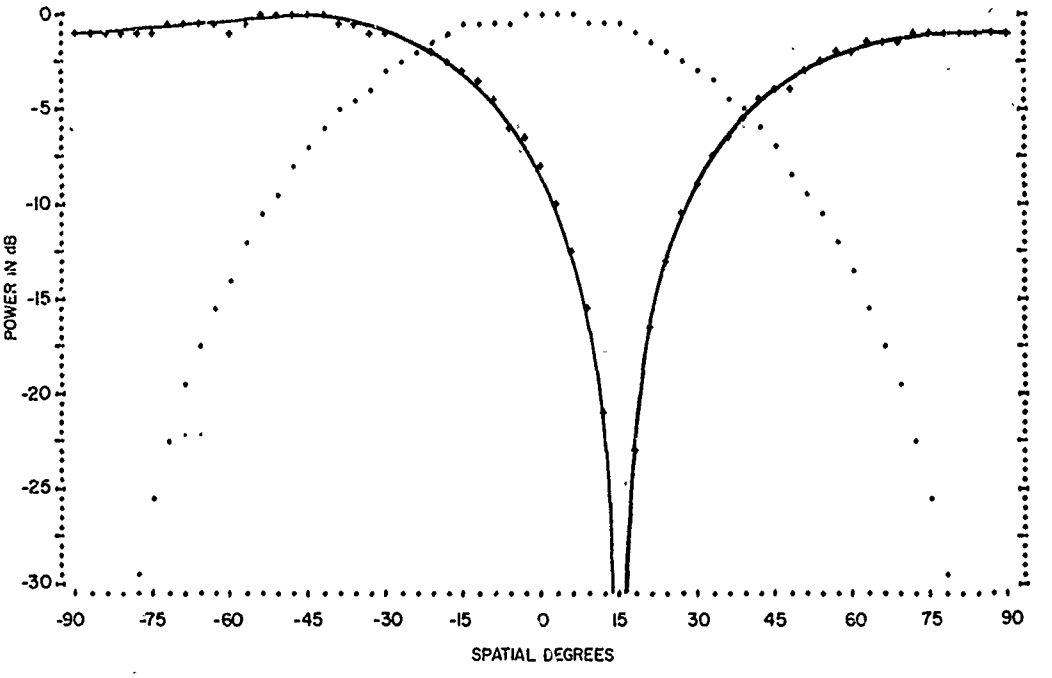

(e) Steady state

Fig. 13 (Continued)—Transient behavior of spatial patterns for $P_i = 100$, $\theta_0 = 0°$, and $\theta_i = 15°$

$$Y_n = W_1 E_1 + W_2 E_2$$

$$= \sqrt{|W_1 n_1|^2 + |W_2 n_2|^2} + J_i \left(W_1 e^{-ju_i} + W_2 e^{ju_i} \right), \tag{3.64}$$

where the square-root term expresses the fact that n_1 and n_2 derive from independent receiver noise sources. This term can be simplified because the rms amplitudes are assumed to be equal; i.e.,

$$\sqrt{|W_1 n_1|^2 + |W_2 n_2|^2} = |n_2| \sqrt{|W_1|^2 + |W_2|^2}\,. \tag{3.65}$$

The value of this term prior to time $t = 0$ represents the quiescent output receiver noise voltage, and since both W_1 and $W_2(0)$ have an amplitude of unity,

$$|n_2| \sqrt{|W_1|^2 + |W_2|^2}\Big|_{t<0} = \sqrt{2}\,|n_2|\,. \tag{3.66}$$

Thus, the increase in output noise power caused when an interference source is turned on can be expressed as a ratio of the square of the amplitude of Y_n to the square of the quiescent output receiver noise voltage; i.e.,

$$\frac{|Y_n|^2}{2|n_2|^2} = \frac{1}{2}\left(1 + |W_2|^2 + \frac{|J_i|^2}{|n_2|^2}\left|W_1 e^{-ju_i} + W_2 e^{ju_i}\right|^2\right), \tag{3.67}$$

where the ratio of $|J_i|^2$ to $|n_2|^2$ can be replaced by power ratio P_i.

Figure 14 illustrates the plotting of Eq. (3.67), when $\theta_0 = 0°$ and $\theta_i = 15°$, for power ratios of 10 dB, 20 dB, 30 dB, and 40 dB. These curves show clearly the direct dependence on power ratio P_i of the speed of transient response. If one examines the amount of time elapsed for output noise power to drop to the 3-dB increase point, the following tabulated are obtained:

P_i (dB)	Recovery Time to 3-dB Increase (μs)
10	1,000
20	175
30	24
40	3

There are two additional points of interest concerning the curves in Fig. 14. First, the starting value of the output noise power at time $t = 0$ will, of course, depend on the value of the array space factor in direction θ_i; i.e., the location of the interference source

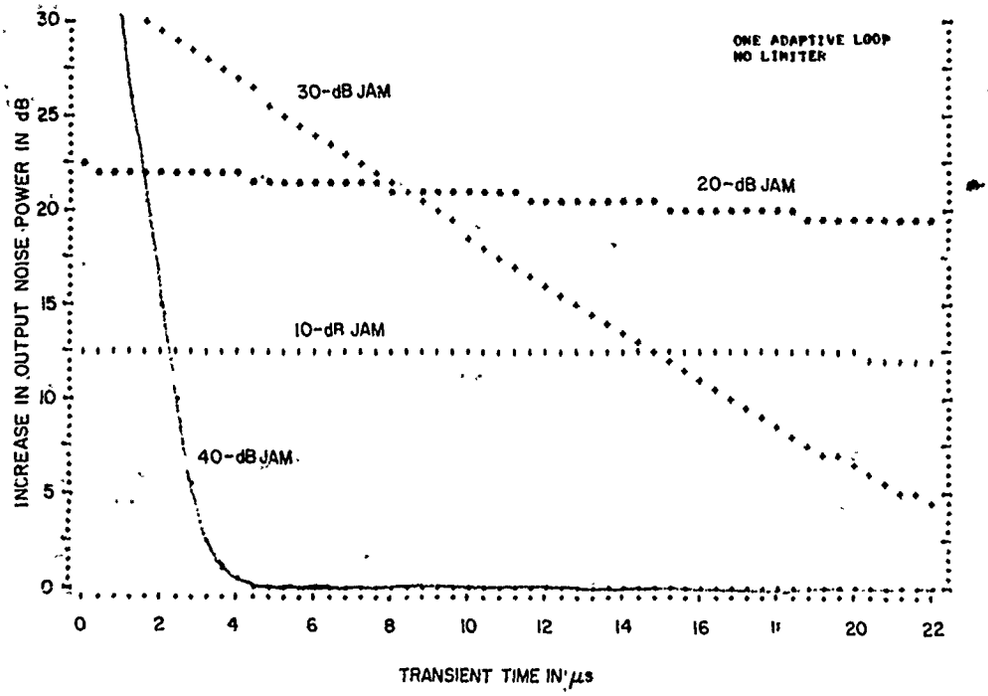

Fig. 14—Transient behavior of output noise power when $\theta_0 = 0°$, $\theta_i = 15°$, for P_i values of 10 dB, 20 dB, 30 dB, and 40 dB

in the quiescent spatial power pattern of the array. For our two-element array, this is readily shown if the value of $W_2(0)$ from Eq. (3.57) is inserted into Eq. (3.67); simplifying shows that

$$\left(\frac{|Y_0|^2}{2|n_2|^2}\right)_{t=0} = 1 + 2P_i \cos^2 (u_0 - u_i). \tag{3.68}$$

Note that the squared cosine term is quiescent power pattern value $|G_q(\theta_i)|^2$.

Second, the end or steady-state value of the increase in output noise power after the transient has died out. We can obtain this by taking the steady-state part of W_2 as given in Eq. (3.56) and substituting it into Eq. (3.67) to get

$$\left(\frac{|Y_0|^2}{2|n_2|^2}\right)_{t=\infty} = \frac{1}{2}\left\{1 + |W_2|^2 + \left[\frac{4\sqrt{P_i}\cos(u_0 - u_i)}{2 + P_i}\right]^2\right\}. \tag{3.69}$$

This steady-state equation results in unity when $P_i = 0$ or when $P_i >> 1$, but it is greater than unity when P_i is near unity. This steady-state increase in output noise power is shown in Fig. 15 plotted vs ratio P_i for the worst condition, where $\theta_i = \theta_0$. Note that it peaks at an increase of 1.75 dB when $P_i = 2$, and that steady-state $W_2(\infty)$ is zero for that particular ratio.

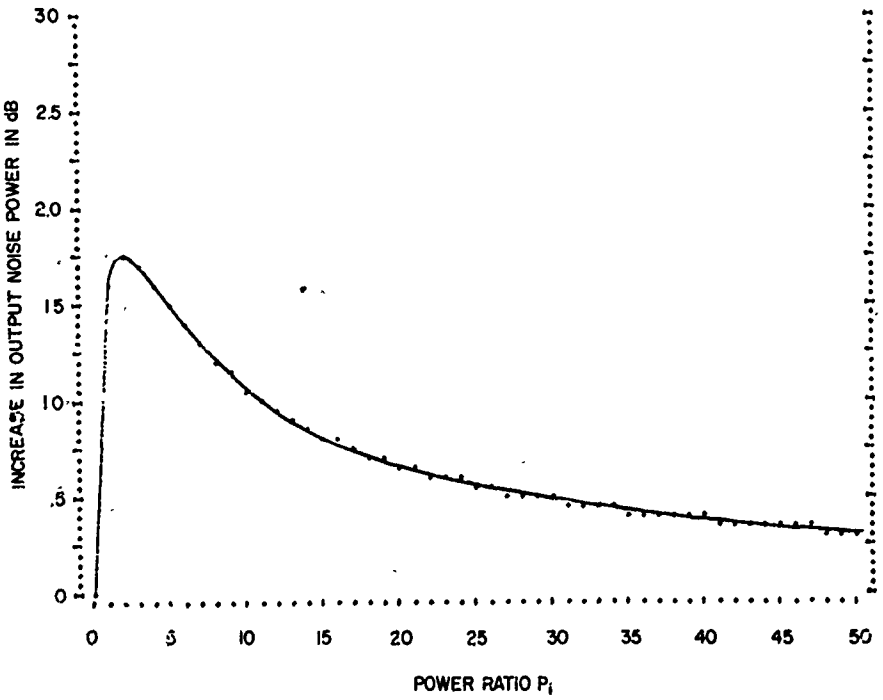

Fig. 15—Steady-state increase in output noise power vs P_i for worst condition, $\theta_i = \theta_0$

Bandwidth Effects—The bandwidth of the power received from the source of interference will affect the performance of our adaptive array because the array is frequency sensitive. Recall that adaptive weight W_2 can assume only one amplitude value and one phase value at any given instant of time. The delay (or advance) of an incoming signal at one element with respect to another involves a true time-delay distance, as shown in Fig. 16, where time-delay distance u_i is referenced to the geometric phase center of the array. For any given wavelength λ we defined u_i in Eq. (3.8) as

$$u_i = \frac{\pi d}{\lambda} \sin \theta_i .$$

We have assumed an element spacing of half a wavelength, which can now be more rigorously defined as wavelength λ_0 corresponding to center frequency f_0 of the RF bandwidth.

Therefore specify

$$d = \frac{\lambda_0}{2} \tag{3.70}$$

and

$$u_i = \frac{\lambda_0}{\lambda} \frac{\pi}{2} \sin \theta_i$$

or

$$u_i = \frac{f}{f_0} \frac{\pi}{2} \sin \theta_i . \tag{3.71}$$

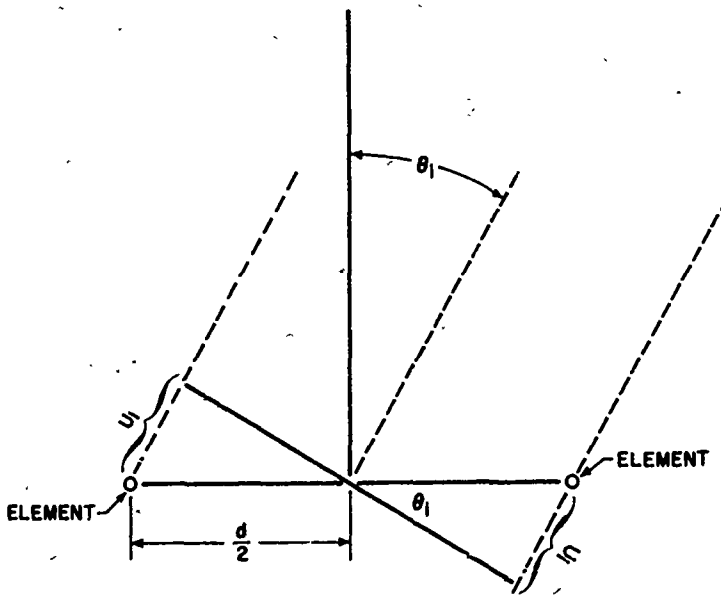

Fig. 16—Diagram for true time-delay distance u_i

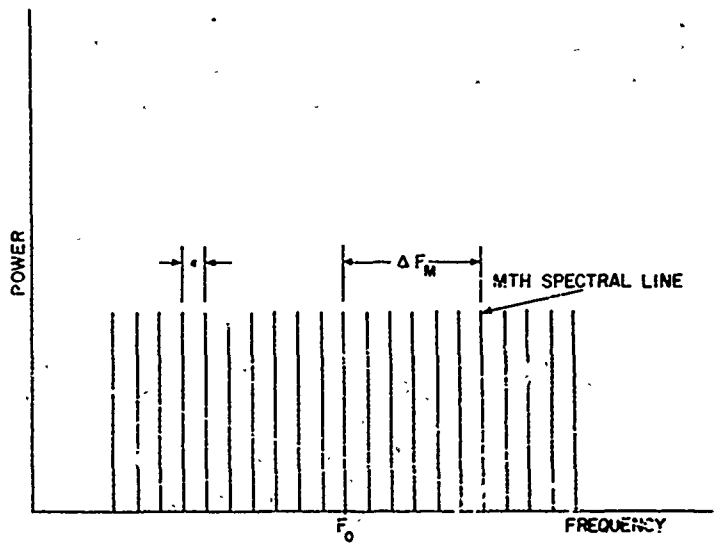

Fig. 17—Interference-source power spectrum, uniform amplitude lines spaced ϵ apart

Frequency f can be further defined as equal to f_0 plus some offset Δf, so that u_i finally becomes

$$u_i = \left(1 + \frac{\Delta f}{f_0}\right)\frac{\pi}{2}\sin\theta_i . \tag{3.72}$$

With this frequency-dependent relationship for u_i, we can now handle an interference source with bandwidth by dividing its power into a number of discrete spectral lines, the mth line of which has associated with it offset frequency Δf_m, voltage at the mixers J_m, and power ratio P_m. For convenience in calculation, assume a uniform amplitude spectrum of lines spaced apart by a constant frequency increment, as shown in Fig. 17. Further assume that the lines are not coherent with one another; i.e., they will not cross-correlate. Under these assumptions, element signals E_1 and E_2 in Eq. (3.7) may be rewritten as the summations

$$\left.\begin{aligned} E_1 &= n_1 + \sum_{m=1}^{M} J_m e^{-ju_m} \\ E_2 &= n_2 + \sum_{m=1}^{M} J_m e^{ju_m} \end{aligned}\right\} \text{for } t \geq 0, \tag{3.73}$$

where

$$u_m = \left(1 + \frac{\Delta f_m}{f_0}\right)\frac{\pi}{2} \sin \theta_i \tag{3.74}$$

$$|J_i|^2 = \sum_{m=1}^{M} |J_m|^2 \tag{3.75}$$

with

M = total number of spectrum lines

$|J_i|$ = total voltage magnitude at mixers.

From the same arguments on cross-correlation as used previously, the cross-correlation products from the new E_1 and E_2 would be

$$\overline{(E_1 E_2^*)} = \sum_{m=1}^{M} |\bar{J}_m|^2 e^{-j2u_m} \tag{3.76}$$

$$\overline{(E_2 E_2^*)} = |\bar{n}_2|^2 + \sum_{m=1}^{M} |\bar{J}_m|^2 = |\bar{n}_2|^2 + |\bar{J}_i|^2. \tag{3.77}$$

The new expression for $\overline{(E_1 E_2^*)}$ must be incorporated into W_{02}, changing Eq. (3.55) to

$$W_{02} = -\frac{W_1 \overline{(E_1 E_2^*)}}{|E_2|^2} = -W_1 \frac{i t_0}{\mu} \sum_{m=1}^{M} P_m e^{-j2u_m}. \tag{3.78}$$

The expression for μ remains the same as before, since we interpret P_i as the sum of all the spectral-line power ratios; i.e.,

$$\mu = \mu_0(1 + P_i)$$

where $P_i = \sum_{m=1}^{M} P_m$.

It is evident that W_{02}, although optimum, no longer represents a perfect solution for W_2 because we now have a different phase angle $2u_m$ associated with each spectral-line contribution, and we will get a single resultant vector representing the sum of all of these small vector contributions. Thus W_{02} represents an adaptation to the power centroid of the interference spectrum.

The increase in output noise power can be expressed by a ratio similar to Eq. (3.67):

$$\frac{|Y_n|^2}{2|n_2|^2} = \frac{1}{2}\left(1 + |W_2|^2 + \sum_{m=1}^{M} P_m |(W_1 e^{-ju_m} + W_2 e^{ju_m})|^2\right). \qquad (3.80)$$

The sum term consists of a summation of individual power residues which correspond to the various spectral lines of the source of interference. Figure 18 shows a plot of Eq. (3.80) vs interference source bandwidth when $P_i = 2{,}000$, $\theta_i = 45°$, and $\theta_0 = 0°$. Also plotted are the phase of steady-state W_2 and the output noise that would result from the quiescent, beam-steered pattern alone. The abscissa scale is percentage bandwidth, and each successive point represents an increase of one more spectral line, which increases bandwidth by 0.2%. For example, starting at the origin, we have the entire power ratio of 2,000 concentrated into a single spectral line of "zero bandwidth," and steady-state adapted weight $W_2(\infty)$ from Eq. (3.52) nulls it out to a negligible residue. The next abscissa point then adds a spectral line at a frequency 0.2% higher than the first line, giving us a "bandwidth" of 0.2% for the two lines and dividing the power equally into 1,000 for each line. The next point adds a third spectral line 0.2% higher in frequency than the second, resulting in a "bandwidth" of 0.4% for the three lines and an equal power of 666 per line. This process of adding spectral lines is continued up to 51 lines, resulting in a bandwidth of 10% and an equal power of 39.2 per line. Figure 18 shows clearly the deterioration (increase) in output noise power as the constant power of the interference source is spread over an increasingly wider bandwidth.

To prevent confusion, recall that two different bandwidths are involved here: first, the fixed channel bandwidth B_c of 5 Mc, which determines a fixed receiver noise-power level;

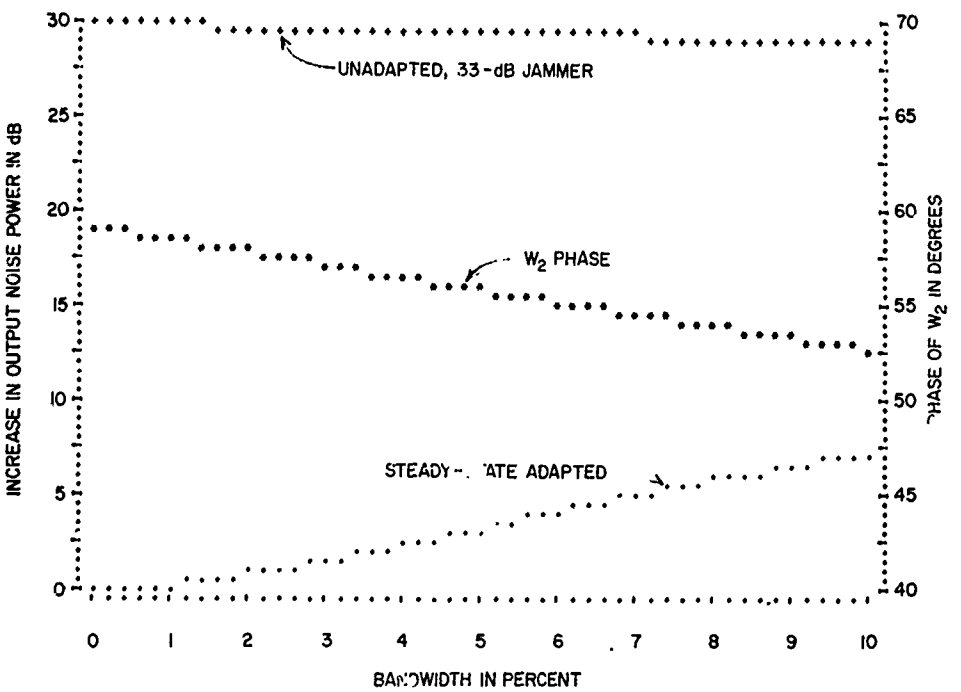

Fig. 18—Output noise power versus bandwidth of interference source for $P_i = 2{,}000$, $\theta_i = 45°$, $\theta_0 = 0°$

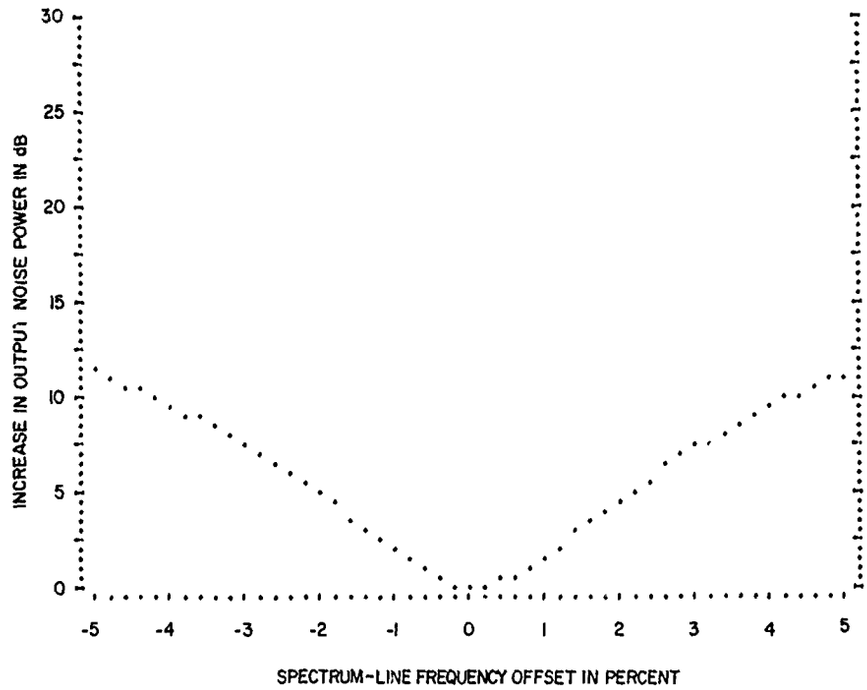

Fig. 19—Output noise power contributed by each of the 51 spectral lines for the 10% bandwidth case

second, the bandwidth of the interference source, expressed in percentage, which must always be contained within B_c in order to be meaningful.

The 7-dB increase in output noise power at 10% bandwidth for this case is a summed result. It is of interest to see what happens to each spectral line in the output for this 10% bandwidth case, and Fig. 19 shows the increase in output noise power contributed by each of the 51 spectral lines within its own 0.2% subbandwidth. Here we see the effect of adapting W_2 to the "power centroid" of the interference spectrum; i.e., the center frequencies of the power spectrum are nulled out nicely by the single vector weight, and, even though the nulling must deteriorate for frequencies away from band center, the extremes are well balanced to achieve the best overall noise-output compromise.

3.5. Hard-limiter Modification

The adaptive loop configuration of Fig. 8. which we have been discussing, has two drawbacks because voltage output X_2 from the correlation mixer is proportional to the power received at the elements:

1. The dynamic range of voltage X_2 is the square of the element signal dynamic range. Thus, to handle the 40-dB range of interference power discussed in previous sections, the correlator branch components must have a linear dynamic range of 80 dB,

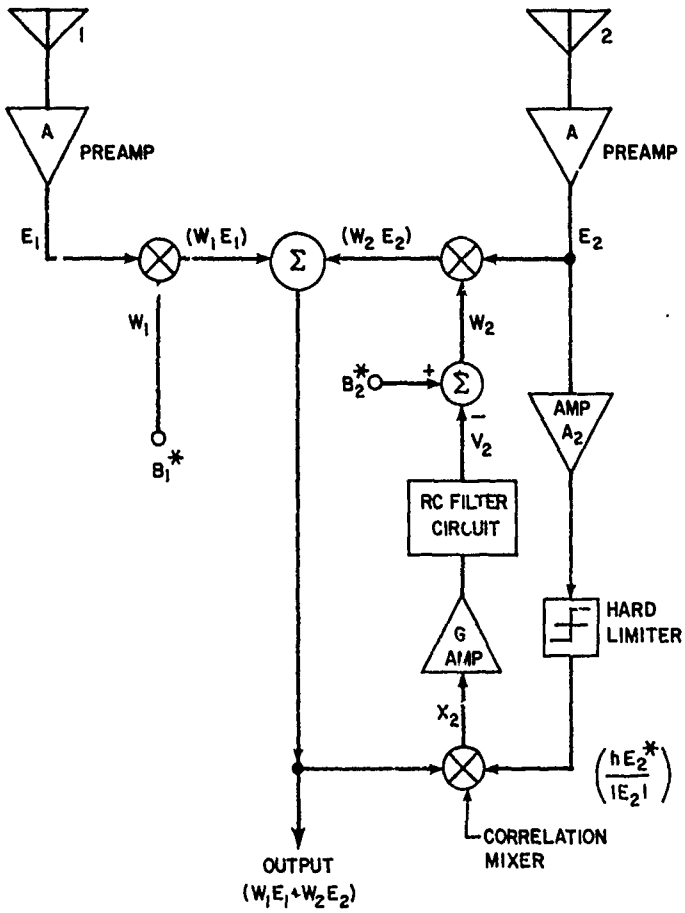

Fig. 20—Hard-limiter modification of single adaptive control loop

which is uncomfortably close to practical component limits. Conversely, a severe restriction is placed on the system input signal dynamic range.

2. The speed of response is proportional to power, as shown in Fig. 14, and this results in very sluggish response for weaker sources of interference.

The best solution so far discovered for alleviating these drawbacks has been to modify the adaptive loop by incorporating a hard limiter in the conjugate signal branch of the correlation mixer [19]. This hard-limiter modification is shown in Fig. 20, where it will be noted that an amplifier of gain A_2 precedes the limiter. The purpose of the amplifier is to boost the amplitude of the conjugate signal so that, after limiting, it will be of normal local oscillator level when fed to the correlation mixer. This amplitude level is denoted by constant h.

The modification changes the equations developed in the previous sections because instead of the correlator product as given in Eq. (3.10), we now have

$$X_2' = k^2(W_1E_1 + W_2E_2)\frac{hE_2^*}{|E_2|}. \tag{3.81}$$

The amplitude variation in the conjugate signal has been removed and only the phase variation is retained. If we start with loop gain μ in Eq. (3.29), we find that this becomes

$$\mu' = k^2G'E_2\frac{hE_2^*}{|E_2|} = hk^2G'|\bar{E}_2|, \tag{3.82}$$

so that loop gain is now proportional to voltage level rather than to power level. If we again define amplifier gain G' as in Eq. (3.31), based on the quiescent loop gain of μ_0', the new gain setting will be

$$G' = \frac{\mu_0'}{hk^2|\bar{n}_2|}. \tag{3.83}$$

There is no longer a problem in getting the magnitude of the voltage coming out of the correlation mixer, due to n_2 alone, to dominate over the thermal noise generated there, because enough preamplification has been inserted to raise the output of the limiter to local oscillator level (on the order of 1 mW).

The loop gain can be expressed in terms of a power ratio as in Eq. (3.49) if the above two equations for μ' and G' are used together with Eq. (3.54), so that

$$\frac{\mu'}{\mu_0'} = \frac{hk^2G'|\bar{E}_2|}{hk^2G'|\bar{n}_2|} = \sqrt{\frac{|\bar{n}_2|^2 + |\bar{J}_i|^2}{|\bar{n}_2|^2}} = \sqrt{1 + P_i}. \tag{3.84}$$

Thus, μ'/μ_0' is simply the square root of the previous expression.

Turning next to the relationship between maximum interference power and basic filter time constant τ_0, as in Eq. (3.50), we have

$$\mu_m' = \mu_0'\sqrt{1 + P_{im}} = \left(\frac{\pi B_c\tau_0'}{10}\right) - 1. \tag{3.85}$$

If we again take the maximum interference power ratio of 40 dB and a channel bandwidth of 5 Mc for B_c, then the value for τ_0' is

$$\tau_0' \approx 0.637 \times 10^{-6}(1 + 100\,\mu_0'). \tag{3.86}$$

For $\mu_0' = 1$, $\tau_0' = 64.3\ \mu$s, and the corresponding filter bandwidth is 2,475 cycles. Note that because of the square root of P_{im}, the basic time constant is faster now by the factor of 100.

Optimum weight W_{02}, as given in Eq. (3.19), remains the same, but when expressed in terms of new servo gain factor μ', it must change to the new expression

$$W_{02} = -\frac{W_1\overline{(E_1E_2^*)}}{|\bar{E}_2|^2} = -W_1\left(\frac{\mu_0'}{\mu'}\right)^2 P_i e^{-j2u_i}. \tag{3.87}$$

The equations for new weight W_2' will be the same as Eqs. (3.56), (3.58), and (3.59) if μ' is substituted for μ in those expressions; i.e.,

$$W_2' = [W_2'(0) - W_2'(\infty)]\, e^{-\alpha' t} + W_2'(\infty) \tag{3.88}$$

$$W_2'(\infty) = \frac{1+\mu_0'}{1+\mu'} W_1^* + \frac{\mu'}{1+\mu'} W_{02} \tag{3.89}$$

$$W_2'(0) = B_2^* - V_2'(0) = W_1^* \tag{3.90}$$

where

$$\alpha' = \frac{1+\mu'}{\tau_0'} \quad \text{and} \quad \mu' = \mu_0'\sqrt{1+P_i}.$$

Note that, because of the square root in μ', a considerable change has occurred in both α' and $W_2'(\infty)$. This is best illustrated if Eq. (3.67) is used to plot the transient behavior of the increase in output noise power for the same conditions as in Fig. 14. The new set of curves for the hard-limiter modification is shown in Fig. 21, where $\theta_0 = 0°$ and $\theta_i = 15°$, for P_i of 10 dB, 20 dB, 30 dB, and 40 dB. The transient decay for a 40-dB ratio is identical to the response in Fig. 14 because 40 dB was the maximum power condition for both cases and results in the same value of $\alpha_m' = \alpha_m = 1.58 \times 10^6\ s^{-1}$. However, the decay for ratios less than 40 dB is obviously much faster with the limiter modification. Another large difference evident in Fig. 21 is the rather high steady-state residue (approximately 7 dB) remaining after the transient term has died out. This is principally because the new loop gain μ' involves the square root of P_i and is therefore much smaller than the previous μ for the same power-ratio values.

To reduce the unacceptably large output noise residue, it is necessary to increase quiescent loop gain μ_0' above the value of unity chosen previously. Although this increases the value of τ_0' almost in direct proportion to μ_0', as seen in Eq. (3.85), it has only a minor effect on α', and in turn on the speed of response. Thus, we can improve the retrodirective amplitude portion of $W_2'(\infty)$, by increasing μ_0', without incurring a penalty in response time. Figure 22 shows the increase in steady-state output noise power residue vs P_i, where $\theta_i = \theta_0$, for four values of quiescent loop gain $\mu_0' = 1$, 3, 10, and 100. This shows that it is necessary to have $\mu_0' \geqslant 10$ to hold the residue to a reasonably small value. To illustrate that the response time is unaffected, Fig. 23 shows the transient behavior of output noise power under the same conditions as Fig. 21, except that now $\mu_0' = 100$. If μ_0' can be thus increased, the hard-limiter modification results in a satisfactory output noise residue and retains its advantages of much faster response time, double the dynamic range in decibels, and better loop stability. The disadvantages include the inherent limiter problems of small signal suppression when more than one signal is received and the possible generation of spurious response.

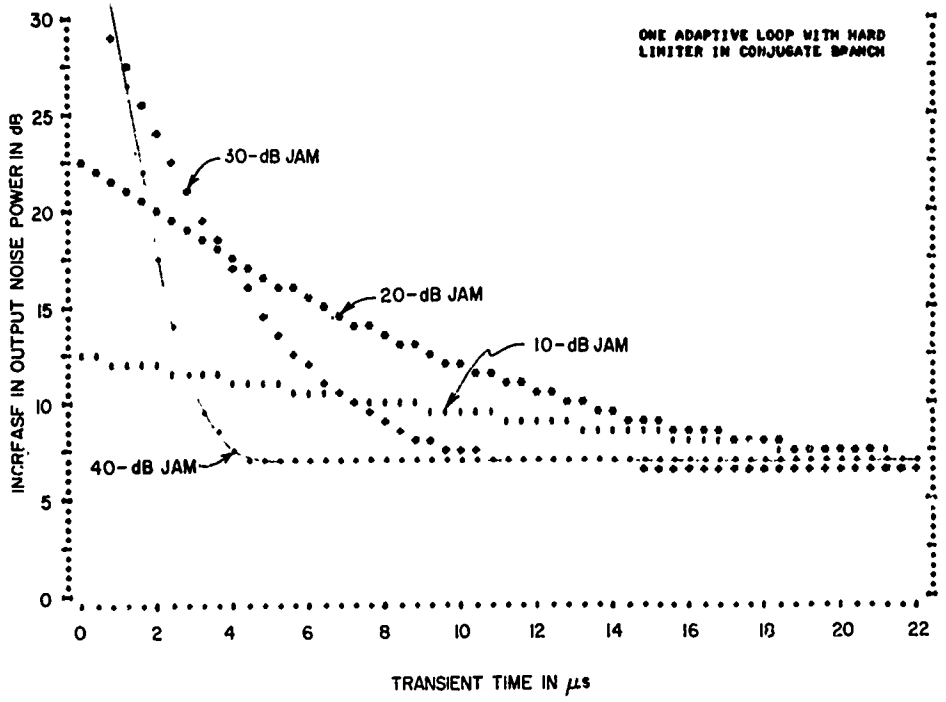

Fig. 21—Limiter-modification transient behavior of output noise power when $\theta_0 = 0°$, $\theta_t = 15°$, for P_t = 10 dB, 20 dB, 30 dB, and 40 dB

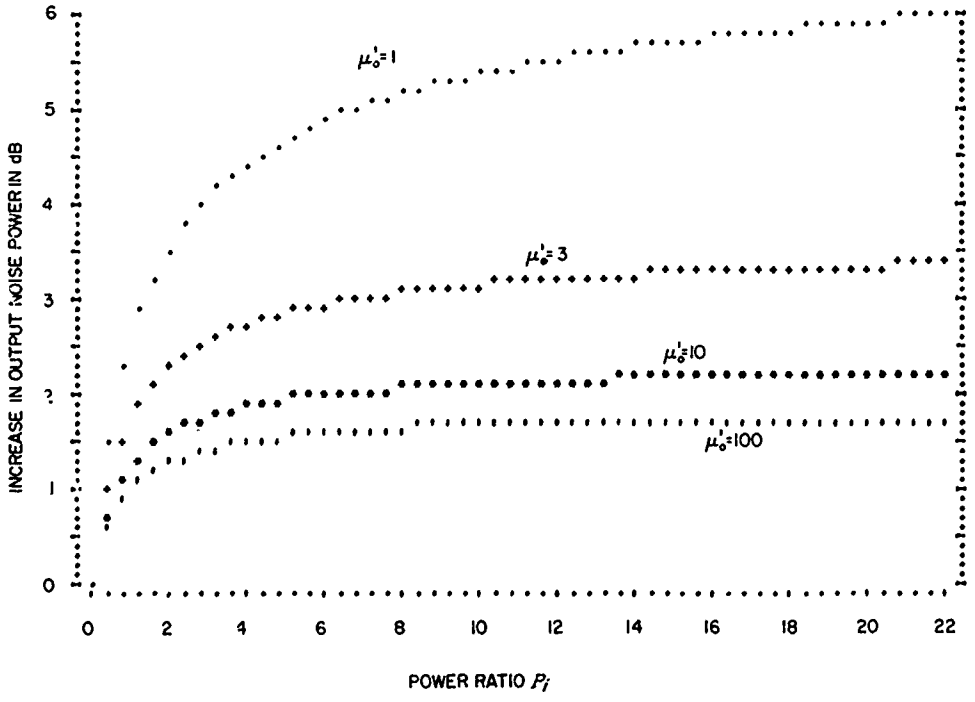

Fig. 22—Limiter-modification steady-state increase in output noise power versus P_t under the worst condition, $\theta_t = \vartheta_0$, for four values of quiescent loop gain, μ_0 = 1, 3, 10, and 100

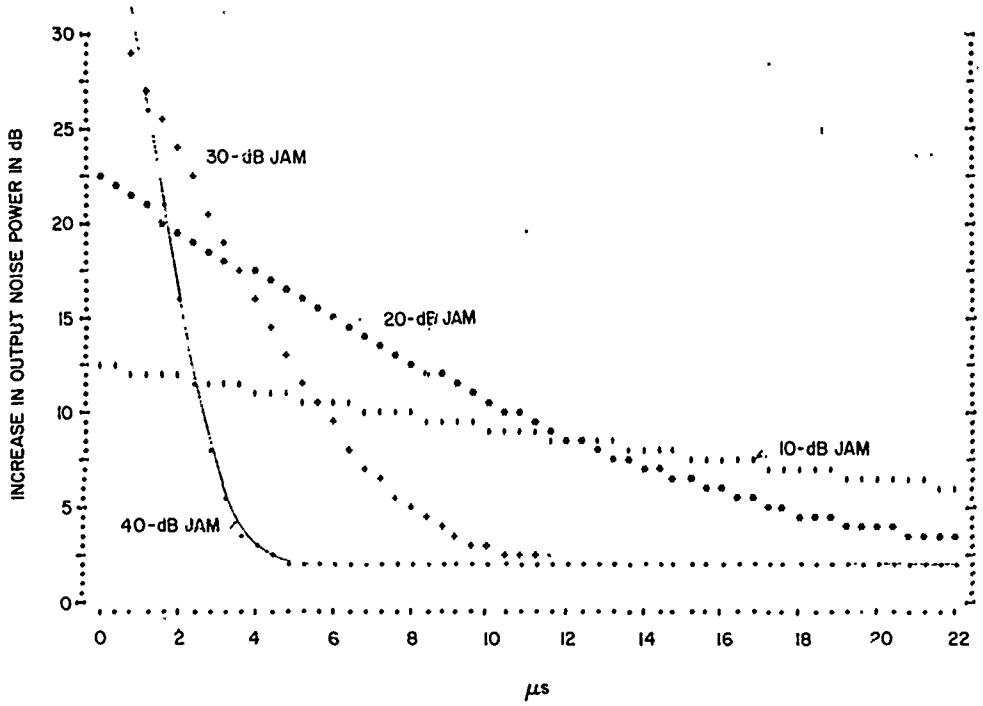

Fig. 23—Limiter-modification transient behavior of output noise power when $\mu_0 = 100$, $\theta_0 = 0°$, $\theta_i = 15°$, for P_i values of 10, 20, 30, and 40 dB

3.6. Correlation Coefficient

In the study and analysis of adaptive arrays, it is desirable to become familiar with the concept of a correlation coefficient. This can be done by starting from the expression for the mean square of output noise voltage Y_n, as given by Eq. (3.17):

$$|\bar{Y}_n|^2 = \overline{|(W_1E_1) + (W_2E_2)|^2}. \tag{3.91}$$

If the expression for W_{02} in Eq. (3.19) is used, $|Y_n|^2$ can be manipulated into the interesting form

$$|\bar{Y}_n|^2 = |\overline{W_1E_1}|^2 - (|W_{02}|^2|\bar{E}_2|^2) + (|W_2 - W_{02}|^2|\bar{E}_2|^2). \tag{3.92}$$

Then, for W_2 equal to W_{02}, we would have the minimum output noise residue expressed as

$$|\bar{Y}_n|^2_{\min} = |\overline{W_1E_1}|^2 - |W_{02}|^2|\bar{E}_2|^2 \tag{3.93}$$

or

$$|\bar{Y}_n|^2_{\min} = \left(1 - \frac{|W_{02}|^2|\bar{E}_2|^2}{|\overline{W_1E_1}|^2}\right)|\overline{W_1E_1}|^2. \tag{3.94}$$

Next, define a coefficient ρ for the ratio contained in the brackets; i.e., let

$$|\rho|^2 = \frac{|W_{02}|^2|\bar{E}_2|^2}{|\overline{W_1E_1}|^2} = \left(\frac{|\overline{E_1E_2^*}|^2}{|\bar{E}_1|^2|\bar{E}_2|^2}\right) \tag{3.95}$$

or define

$$\rho = \frac{(E_1E_2^*)}{|\bar{E}_1||\bar{E}_2|}. \tag{3.96}$$

Thus, we have a normalized cross-correlation coefficient for element signals E_1 and E_2 or, simply, a correlation coefficient in the statistical sense, because the time-averaged product $\overline{(E_1E_2^*)}$ is the covariance of E_1 and E_2, and it is being divided by the time-averaged magnitudes of E_1 and E_2 which are the square roots of their variances. This is a useful concept, because the real-life signals either consist of noise or are corrupted by noise, so that statistical theory is needed for correct mathematical interpretation.

Using the correlation coefficient, then, makes the minimum output noise residue simply

$$|\bar{Y}_n|^2_{\min} = (1 - |\rho|^2)|\overline{W_1E_1}|^2. \tag{3.97}$$

Note that $(1 - |\rho|^2)$ is equal to the ratio of minimum output noise residue to the power in channel 1 and therefore defines a maximum cancellation ratio,

$$\frac{|\bar{Y}_n|^2_{\min}}{|\overline{W_1E_1}|^2} = (1 - |\rho|^2). \tag{3.98}$$

Obviously, a good cancellation ratio demands a high degree of correlation between the two channels.

If we now substitute the complete expression for $W_2(\infty)$, Eq. (3.56), into Eq. (3.92) to incorporate the steady-state servo error contribution, we find that the output noise residue increases to the value

$$|\bar{Y}_n|^2 = \left[1 - |\rho|^2 + \left(\frac{1}{1+\mu}\right)^2\left|(1+\mu_0)\frac{W_1^*|E_2|}{W|E_1|} + \rho\right|^2\right]|\overline{W_1E_1}|^2. \tag{3.99}$$

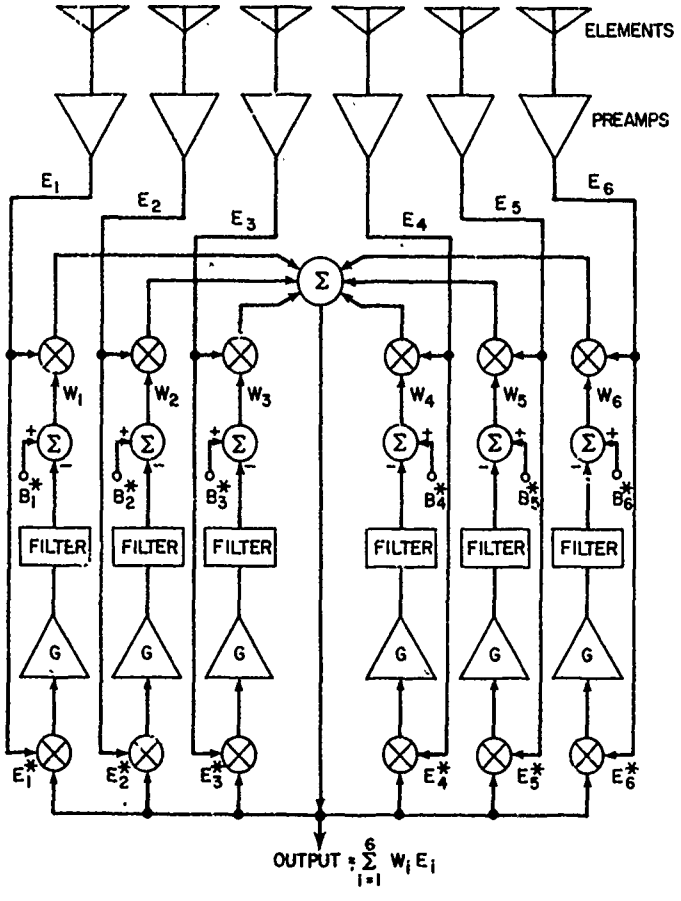

Fig. 24—An analog linear adaptive array configuration of six elements and six loops with beam steering

For the hard-limiter modification, μ must be replaced by μ'.

These expressions, based on the correlation coefficient, permit evaluation of decorrelation effects caused by mismatches between the transfer functions of the two channels, differences in arrival times at the elements (array bandwidth effects), and multipath effects. Reference 19 is recommended to the reader for further discussion of such decorrelation effects.

4. *K*-ELEMENT ARRAY WITH *K* ADAPTIVE LOOPS

Now that the basic principles of operation and the performance characteristics of a single adaptive servo loop have been discussed, we are ready to consider the multiple-loop case, wherein each element of a *K*-element linear array has an associated adaptive servo loop. A possible configuration for such an adaptive array is shown in Fig. 24 for six elements. Note that each servo loop is arranged in the same manner as the single loop of Fig. 8.

Define element signal column vector $\mathbf{E}$ in which kth element component E_k is similar to Eq. (3.7) and consists of quiescent receiver channel noise voltage n_k plus a summation of voltages associated with I external, narrowband interference sources:

$$\mathbf{E}^t = [E_1, E_2, E_3, \ldots, E_k] \tag{4.1}$$

where

$$E_k = n_k + \sum_{i=1}^{I} J_i e^{ju_i(2k-K-1)} \tag{4.2}$$

$$u_i = \left(\frac{\pi d}{\lambda}\right) \sin \theta_i. \tag{4.3}$$

Note that $\mathbf{E}^t$ is the transpose of matrix $\mathbf{E}$. The sources are assumed to be statistically independent; J_i is the element channel voltage amplitude associated with the ith source, and θ_i is its azimuth angle direction from array boresight. It is assumed that a given source will induce equal voltage amplitudes at all of the array elements. Element phase is referenced to the geometric center of the array.

The beam-steering signals are intended to set up a shaped receive beam which is steered in some desired azimuth direction θ_0. For quiescent conditions wherein only receiver noise is present, the adaptive weights will settle to steady-state values denoted by the quiescent weight column vector $\mathbf{W}_q$. We want the components of this vector to be precisely equal to the array weights one would choose to generate the desired quiescent, shaped-beam pattern $G_q(\theta)$. Thus, define $\mathbf{W}_q$ as this desired vector, so that

$$\mathbf{W}_q^t = [W_{q1}, W_{q2}, W_{q3}, \ldots, W_{qK}]. \tag{4.4}$$

where

$$W_{qk} = a_k e^{-ju_0(2k-K-1)} \tag{4.5}$$

$$u_0 = \left(\frac{\pi d}{\lambda}\right) \sin \theta_0. \tag{4.6}$$

The values of element coefficients a_k are chosen to achieve the desired beamshape and sidelobe levels. The quiescent beam pattern can then be expressed as

$$G_q(\theta) = (\mathbf{S}^t \mathbf{W}_q) = \sum_{k=1}^{K} a_k e^{j(u-u_0)(2k-K-1)}, \tag{4.7}$$

where $\mathbf{S}$ is a column vector representing element signals of unit amplitude. Phase factor u is associated with far-field angle variable θ; i.e.,

$$\mathbf{S}^t = [S_1, S_2, S_3, \ldots, S_K] \tag{4.8}$$

where

$$S_k = e^{ju(2k-K-1)} \tag{4.9}$$

$$u = \frac{\pi d}{\lambda} \sin \theta. \tag{4.10}$$

The components of input beam-steering column vector B* are related to the components of W_q by constants b_k, so that

$$\mathbf{B}^{*t} = [B_1^*, B_2^*, B_3^*, \ldots, B_3^* \tag{4.11}$$

where

$$B_k^* = b_k W_{qk}. \tag{4.12}$$

The b_k will be evaluated in the following section, where it is shown that they are determined by the quiescent servo gain factor.

Voltage outputs from the correlator filters are represented by column vector V, so that we can define an adaptive weight column vector W for the configuration of Fig. 24:

$$W = \begin{bmatrix} W_1 \\ W_2 \\ W_3 \\ \vdots \\ W_K \end{bmatrix} = [\mathbf{B}^* - \mathbf{V}] = \begin{bmatrix} B_1^* \\ B_2^* \\ B_3^* \\ \vdots \\ B_K \end{bmatrix} - \begin{bmatrix} V_1 \\ V_2 \\ V_3 \\ \vdots \\ V_K \end{bmatrix} \tag{4.13}$$

where V_k is the voltage output from the kth correlator filter.

Analysis of multiloop adaptive arrays requires some familiarity with the theory of linear differential equations, matrix algebra, and the solution of eigenvalue problems. References 22 and 23 are recommended for readers who desire to review the mathematics.

4.1. Adaptive Weight Equations

The adaptive servo loops in Fig. 24 are the same as the single loop in Fig. 8, which was described in Sec. 3, so that formulation of the adaptive weight equations can proceed in much the same manner. Thus, weight W_k associated with the kth element is equal to beam-steering signal B_k^* minus output V_k of the associated correlator filter, so that

$$W_k = B_k^* - V_k. \tag{4.14}$$

The averaged correlation mixer voltage $\bar{X}_k$ is again the averaged product of element signal E_k^* with the summed output of the array,

$$\bar{X}_k = k^2 \overline{\left(E_k^* \sum_{i=1}^{K} W_i E_i \right)}, \tag{4.15}$$

and voltage V_k will obey the same RC filter differential equation, Eq. (3.12) and will result in the similar averaged value expression,

$$\tau_0 \frac{dV_k}{dt} + V_k = \gamma \overline{\left(E_k^* \sum_{i=1}^{K} W_i E_i \right)} \tag{4.16}$$

where

$$\gamma = k^2 G. \tag{4.17}$$

The quantity γ is defined as a conversion-factor gain constant, assumed to be the same for each of the servo loops. However, whereas Eq. (3.12) contains only one unknown and can be solved immediately, the above equation contains K unknowns and must be handled as a member of a set of K simultaneous linear differential equations, one for each adaptive loop. For convenience, let us use Eq. (4.14) to convert from V_k to W_k, noting that

$$\frac{dW_k}{dt} = -\frac{dV_k}{dt}. \tag{4.18}$$

whereupon Eq. (4.16) may be rewritten in terms of W_k as

$$\tau_0 \frac{dW_k}{dt} + W_k = B_k^* - \gamma \overline{\left(E_k^* \sum_{i=1}^{K} W_i E_i \right)}. \tag{4.19}$$

The complete set of these weight equations for subscript k values of 1 through K may then be expressed, in terms of the more convenient matrix notation, as

$$\tau_0 \frac{d\mathbf{W}}{dt} + \mathbf{W} = \mathbf{B}^* - \gamma [\overline{\mathbf{E}^* \mathbf{W}^t \mathbf{E}}] \tag{4.20}$$

where $\mathbf{W}^t$ is the transpose of matrix $\mathbf{W}$. Recall from matrix multiplication that

$$(\mathbf{W}^t \mathbf{E}) = (\mathbf{E}^t \mathbf{W}) = \sum_{i=1}^{K} W_i E_i, \tag{4.21}$$

so that the product of the three matrixes in Eq. (4.20) may also be written as

$$\overline{[\mathbf{E}^* \mathbf{W}^t \mathbf{E}]} = \overline{[\mathbf{E}^* \mathbf{E}^t \mathbf{W}]} = \overline{[\mathbf{E}^* \mathbf{E}^t]} \mathbf{W}. \tag{4.22}$$

The averaged product of the conjugate of signal column vector $\mathbf{E}^*$ and its transpose results in a matrix whose components represent the correlations between the various element channel signals or, in other words, the covariance matrix of the set of system inputs. Define this covariance matrix as M;

$$\mathbf{M} = [\overline{\mathbf{E}^*\mathbf{E}^t}] = \begin{bmatrix} \overline{E_1^*E_1} & \overline{E_1^*E_2} & \overline{E_1^*E_3} & \cdots \\ \overline{E_2^*E_1} & \overline{E_2^*E_2} & \overline{E_2^*E_3} & \cdots \\ \overline{E_3^*E_1} & \overline{E_3^*E_2} & \overline{E_3^*E_3} & \cdots \\ \cdots & \cdots & \cdots & \cdots \\ \overline{E_k^*E_1} & \overline{E_k^*E_2} & \overline{E_k^*E_3} & \cdots \end{bmatrix}. \tag{4.23}$$

Note that the components of matrix M may be obtained from the channel signals defined in Eq. (4.2), whereupon these averaged correlations are found to be

$$(\overline{E_k^*E_l}) = \sum_{i=1}^{I} |\bar{J}_i|^2 e^{j2u_i(l-k)} \qquad \text{for } l \neq k \tag{4.24}$$

or

$$(\overline{E_k^*E_l}) = |\bar{E}_k|^2 = (|\bar{n}_k|^2 + \sum_{i=1}^{I} |\bar{J}_i|^2 \quad \text{for } l = k, \tag{4.25}$$

where Eq. (4.25) represents the diagonal elements of M. It is evident that the covariance matrix may be written as the sum of quiescent receiver noise matrix $\mathbf{M}_q$ plus individual interference source matrixes $\mathbf{M}_i$, such that

$$\mathbf{M} = \mathbf{M}_q + \sum_{i=1}^{I} \mathbf{M}_i \tag{4.26}$$

where

$$\mathbf{M}_q = \begin{bmatrix} |\bar{n}_1|^2 & 0 & 0 & \cdots \\ 0 & |\bar{n}_2|^2 & 0 & \cdots \\ 0 & 0 & |\bar{n}_3|^2 & \cdots \\ \vdots & \vdots & \vdots & \ddots \end{bmatrix} \tag{4.27}$$

and

$$\mathbf{M}_i = |J_i|^2 \begin{bmatrix} 1 & e^{j2u_i} & e^{j4u_i} & \cdots \\ e^{-j2u_i} & 1 & e^{j2u_i} & \cdots \\ e^{-j4u_i} & e^{-j2u_i} & 1 & \cdots \\ \cdot & \cdot & \cdot & \cdot \\ \cdot & \cdot & \cdot & \cdot \\ \cdot & \cdot & \cdot & \cdot \end{bmatrix}. \tag{4.28}$$

Note that M is a positive, definite, Hermitian matrix.

Substituting M into Eq. (4.20) and rearranging, we obtain a concise final form of the adaptive-weight matrix equation,

$$\tau_0 \frac{d\mathbf{W}}{dt} + [\mathbf{I} + \gamma\mathbf{M}]\,\mathbf{W} = \mathbf{B}^*, \tag{4.29}$$

where I is the identity matrix, such that

$$\mathbf{I} = [\delta_{ij}] = \begin{bmatrix} 1 & 0 & 0 & \cdots \\ 0 & 1 & 0 & \cdots \\ 0 & 0 & 1 & \cdots \\ \cdot & \cdot & \cdot & \cdot \\ \cdot & \cdot & \cdot & \cdot \\ \cdot & \cdot & \cdot & \cdot \end{bmatrix}. \tag{4.30}$$

The solution of Eq. (4.29) can be accomplished via a special transformation which consists of the eigenvectors of the covariance matrix. From the theory of matrixes, we know that a positive, definite, Hermitian matrix such as M can be diagonalized by a nonsingular, orthonormal, modal matrix transformation which shall be defined as matrix Q. Furthermore, we know that the resulting diagonal components are the eigenvalues of matrix M. In accordance with the usual eigenvalue problem statements,

$$|\mathbf{M} - \beta_i^2\mathbf{I}| = 0 \quad \text{and} \quad \mathbf{M}\mathbf{e}_i = \beta_i^2\mathbf{e}_i. \tag{4.31}$$

the β_i^2 are the eigenvalues (real, positive numbers) of M, and $\mathbf{e}_i$ are the associated eigenvectors,

$$\mathbf{e}_i = \begin{bmatrix} e_{i1} \\ e_{i2} \\ e_{i3} \\ \cdot \\ \cdot \\ e_{ik} \end{bmatrix}. \tag{4.32}$$

These eigenvectors, which are normalized to unit Hermitian length and are orthogonal to one another, make up the rows of the Q matrix:

$$\mathbf{Q} = \begin{bmatrix} e_{11} & e_{12} & e_{13} & \cdots \\ e_{21} & e_{22} & e_{23} & \cdots \\ e_{31} & e_{32} & e_{33} & \cdots \\ \vdots & \vdots & \vdots & \ddots \\ e_{k1} & e_{k2} & e_{k3} & \end{bmatrix}. \tag{4.33}$$

Diagonalization of M by the Q-matrix transformation is expressed in the form

$$[\mathbf{Q}^*\mathbf{M}\mathbf{Q}^t] = [\beta_i^2\delta_{ij}] = \begin{bmatrix} \beta_1^2 & 0 & 0 & \cdots \\ 0 & \beta_2^2 & 0 & \cdots \\ 0 & 0 & \beta_3^2 & \cdots \\ \vdots & \vdots & \vdots & \ddots \\ \vdots & \vdots & \vdots & \ddots \end{bmatrix}. \tag{4.34}$$

Since M is a product of the conjugate of signal vector E and its transpose, Eq. (4.23), it is evident that Eq. (4.34) may be written as

$$[\mathbf{Q}^*\mathbf{M}\mathbf{Q}^t] = [\mathbf{Q}^*\mathbf{E}^*\mathbf{E}^t\mathbf{Q}^t] = [\hat{\mathbf{E}}^*\hat{\mathbf{E}}^t]$$

or

$$[\hat{\mathbf{E}}^*\hat{\mathbf{E}}^t] = [\beta_i^2\delta_{ij}] \tag{4.35}$$

where

$$\hat{\mathbf{E}} = \mathbf{Q}\mathbf{E}. \tag{4.36}$$

Thus, the Q matrix transforms real signal vector E into new orthonormal signal vector $\hat{\mathbf{E}}$. The components of $\hat{\mathbf{E}}$ are determined by the eigenvectors of M; i.e., from Eq. (4.33),

$$\hat{\mathcal{E}}_k = (\mathbf{e}_k{}^t\mathbf{E}). \tag{4.37}$$

Note that these components have two special characteristics. They are decorrelated, so that

$$\overline{(\hat{E}_k^*\hat{E}_l)} = 0 \quad \text{for } l \neq k, \tag{4.38}$$

and their amplitudes are the square root of the eigenvalues, so that

$$\overline{(\hat{E}_k^* \hat{E}_l)} = \beta_k^2 \quad \text{for} \quad l = k$$

or

$$|\hat{E}_k| = \beta_k. \tag{4.39}$$

The transformation is equivalent to the operation of an orthogonal beam-forming network, and this analogy is pursued further in Sec. 4.3 in terms of physical antenna feed networks.

The transformation of the **E** vector in Eq. (4.36) suggests that a similar transformation may be performed on input beam-steering vector $\mathbf{B}^*$ defined in Eq. (4.12), since this vector can be viewed as the conjugate of an equivalent signal vector **B**. Therefore, define transformed beam-steering vector $\hat{\mathbf{B}}^*$ as

$$\hat{\mathbf{B}} = \mathbf{QB} \quad \text{or} \quad \hat{\mathbf{B}}^* = \mathbf{Q}^*\mathbf{B}^* \tag{4.40}$$

where the kth component is determined by the kth eigenvector,

$$\hat{B}_k^* = (\mathbf{e}_k^{*t}\mathbf{B}^*). \tag{4.41}$$

The **Q**-transformation operations on both **E** and $\mathbf{B}^*$ suggest an equivalent circuit representation for the system illustrated in Fig. 24, in which **Q**-transformation networks would be used to achieve an "orthonormal adaptive array" system. This new equivalent circuit representation is shown in Fig. 25, alongside a simplified schematic diagram of the real system. There will be a new set of weights $\hat{\mathbf{W}}$ in the orthonormal system, and if one develops the adaptive weight matrix equation in a manner similar to Eq. (4.29), it will be found that

$$\tau_0 \frac{d\hat{\mathbf{W}}}{dt} + [\mathbf{I} + \gamma\hat{\mathbf{M}}]\hat{\mathbf{W}} = \hat{\mathbf{B}}^* \tag{4.42}$$

where

$$\hat{\mathbf{M}} = \overline{[\hat{\mathbf{E}}^*\hat{\mathbf{E}}^t]} = [\beta_i^2 \delta_{ij}]. \tag{4.43}$$

Thus, in the orthonormal system we obtain a set of independent linear differential equations, each of which has a solution if the eigenvalues can be determined. Each of the orthonormal servo loops will behave as if the other loops did not exist, because the $\hat{E}_k$ signals are orthogonalized and have zero correlation. The kth servo loop, then, can be viewed in much the same manner as the single servo loop discussed in Sec. 3, and from Eq. (4.42) its weight equation will be

$$\tau_0 \frac{d\hat{W}_k}{dt} + (1 + \gamma\beta_k^2)\hat{W}_k = \hat{B}_k^*. \tag{4.44}$$

The first important similarity to note is the equivalent servo gain factor, which may be defined from the above equation as

$$\mu_k = \gamma\beta_k^2 \tag{4.45}$$

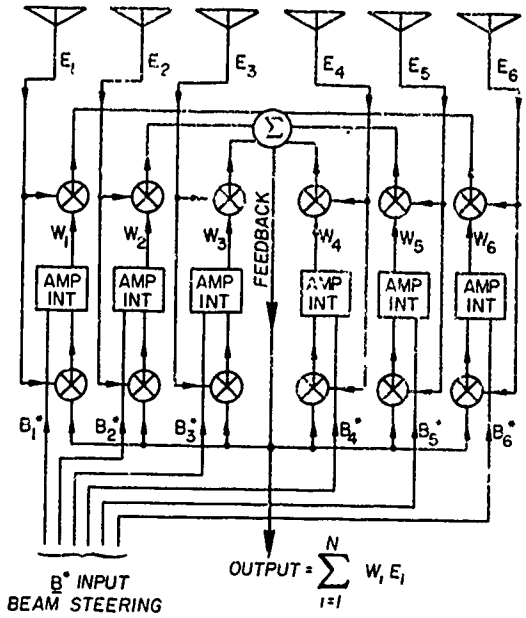

(a) Real-system circuit

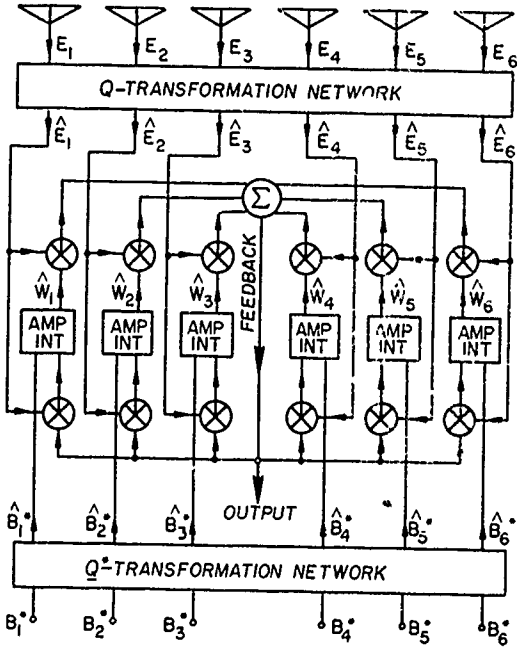

(b) Equivalent orthonormal-system circuit

Fig. 25—Equivalent circuit representations for six-element adaptive array configuration

so that our equivalent servo gain factors are now determined by the eigenvalues of the covariance matrix. When compared against Eq. (3.29), note that positive, real eigenvalues β_k^2 correspond to the square of a signal voltage amplitude. This analogy is carried further in Sec. 4.3, where it is shown that any given eigenvalue is proportional to the power appearing at its orthonormal network output port.

There is also an optimum weight $\hat{W}_{ok}$, which will be derived in Sec. 4.2 and found to be equal to

$$\hat{W}_{ok} = \left(\frac{1}{\mu_k}\right)\hat{B}_k^* . \tag{4.46}$$

If we substitute μ_k and $\hat{W}_{ok}$, into Eq. (4.44), it can be rewritten in the form

$$\tau_0 \frac{d\hat{W}_k}{dt} + (1 + \mu_k)\hat{W}_k = \mu_k \hat{W}_{ok} . \tag{4.47}$$

This equation is now of exactly the same form as Eq. (3.21), and for a step-function change in the input signal a similar solution may be written:

$$\hat{W}_k = [\hat{W}_k(0) - \hat{W}_k(\infty)]\, e^{-\alpha_k t} + \hat{W}_k(\infty) \tag{4.48}$$

where

$$\hat{W}_k(\infty) = \left(\frac{\mu_k}{1 + \mu_k}\right)\hat{W}_{ok} \tag{4.49}$$

$$\alpha_k = \left(\frac{1 + \mu_k}{\tau_0}\right). \tag{4.50}$$

Also, $\hat{W}_k(\infty)$ is the steady-state weight, $\hat{W}_k(0)$ is the initial weight value at $t=0$, and α_k is the transient decay factor. The transient responses will now be determined by the eigenvalues. This kth orthonormal servo loop may be modeled as the simple Type-0 follower servo shown in Fig. 26.

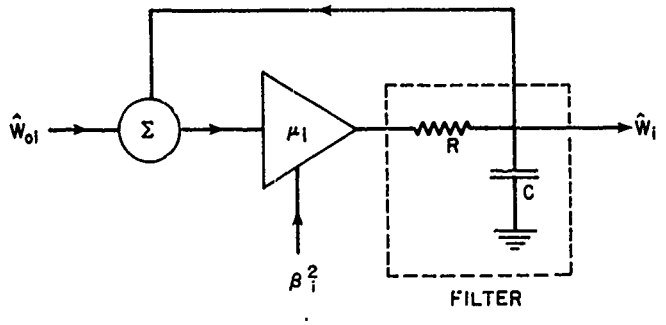

Fig 26—Type-zero follower servo model for the ith orthonormal adaptive control loop

The next step is to relate these $\hat{W}_k$ solutions to real weights W_k. Note that the outputs of the two systems shown in Fig. 25 must be identical; i.e.,

$$\sum_{k=1}^{K} W_k E_k = \sum_{k=1}^{K} \hat{W}_k \hat{E}_k \tag{4.51}$$

$$\mathbf{W}^t\mathbf{E} = \hat{\mathbf{W}}^t\hat{\mathbf{E}} = \hat{\mathbf{W}}^t\mathbf{Q}\mathbf{E}.$$

Thus,

$$\mathbf{W}^t = \hat{\mathbf{W}}^t\mathbf{Q} \quad \text{or} \quad \mathbf{W} = \mathbf{Q}^t\hat{\mathbf{W}}, \tag{4.52}$$

and the solution for the kth real weight becomes

$$W_k = (e_{1k}\hat{W}_1 + e_{2k}\hat{W}_2 + e_{3k}\hat{W}_3 + \cdots + e_{Kk}\hat{W}_K). \tag{4.53}$$

Each real weight is therefore a summation of all the orthonormal weights.

Using Eq. (4.52), we can go back to Eq. (4.29) to verify the orthonormal Eq. (4.42). Substituting for W in Eq. (4.29) results in

$$\tau_0 \frac{d}{dt}[\mathbf{Q}^t\hat{\mathbf{W}}] + [\mathbf{Q}^t + \gamma\mathbf{M}\mathbf{Q}^t]\hat{\mathbf{W}} = \mathbf{B}^*. \tag{4.54}$$

Multiplying through on the left by $\mathbf{Q}^*$, we get

$$\tau_0 \frac{d}{dt}[\mathbf{Q}^*\mathbf{Q}^t\hat{\mathbf{W}}] + [\mathbf{Q}^*\mathbf{Q}^t + \gamma\mathbf{Q}^*\mathbf{M}\mathbf{Q}^t]\hat{\mathbf{W}} = \mathbf{Q}^*\mathbf{B}^*. \tag{4.55}$$

Because of the orthonormal properties of the eigenvectors in the Q matrix,

$$[\mathbf{Q}^*\mathbf{Q}^t] = \mathbf{I}, \tag{4.56}$$

and by Eq. (4.34) the covariance matrix will be diagonalized by the Q transformations, which results in

$$\tau_0 \frac{d\hat{\mathbf{W}}}{dt} + [(1 + \gamma\beta_i^2)\delta_{ij}]\hat{\mathbf{W}} = \hat{\mathbf{B}}^*.$$

Next evaluate the b_k coefficients which relate $\mathbf{B}^*$ to $\mathbf{W}_q$ (Eq. (4.12)). To do this in a simple manner, assume quiescent conditions in which only receiver noise is present, so that the element channel signals are decorrelated and there is no difference between transformed weights and real weights; i.e., the quiescent Q matrix would be an identity matrix,

$$\text{quiescent } \mathbf{Q} = \mathbf{Q}_q = \mathbf{I}. \tag{4.58}$$

The quiescent covariance matrix $\mathbf{M}_q$ from Eq. (4.27) is already diagonalized, and if we further assume that the receiver noise power in all element channels is equal and denoted by $|\overline{n_0}|^2$, then from Eq. (4.34)

$$\mathbf{Q}_q^* \mathbf{M}_q \mathbf{Q}_q^t = [\beta_0^2 \delta_{ij}]$$

or

$$\beta_0^2 = |\overline{n}_0|^2, \tag{4.59}$$

so that we have a smallest eigenvalue β_0^2 equal to the receiver noise channel power. This smallest eigenvalue then defines a minimum servo gain factor μ_0, from Eq. (4.45):

$$\mu_0 = \gamma \beta_0^2. \tag{4.60}$$

Since quiescent steady-state weight $\mathbf{W}(\infty)$ must be equal to $\mathbf{W}_q$ by definition, we can apply Eqs. (4.49), (4.46), and (4.12) to get

$$W_{qk} = \left(\frac{1}{1+\mu_0}\right) B_k^* = \left(\frac{b_k}{1+\mu_0}\right) W_{qk}$$

or

$$b_k = (1+\mu_0). \tag{4.61}$$

Thus, the coefficients of the input beam-steering signal $\mathbf{B}^*$ are always greater than the coefficients of $\mathbf{W}_q$ by the factor $(1+\mu_0)$.

Combining Eqs. (4.49), (4.46), (4.41), (4.12), and (4.61), one can rewrite $\hat{W}_k(\infty)$ in terms of $\mathbf{W}_q$ to obtain

$$\hat{W}_k(\infty) = \left(\frac{1+\mu_0}{1+\mu_k}\right) \hat{W}_{qk} \tag{4.62}$$

where

$$\hat{W}_{qk} = \left(\mathbf{e}_k^{*t} \mathbf{W}_q\right). \tag{4.63}$$

$\hat{W}_{qk}$ is the kth component of quiescent beam-steering weight vector $\mathbf{W}_q$ in orthonormal space.

If we assume quiescent conditions up to time $t = 0$, with only receiver noise present, so that the external interference sources are switched on at $t = 0$, then

$$\hat{W}_k(0) = \hat{W}_{qk}, \tag{4.64}$$

and Eq. (4.48) may be manipulated into the convenient form

$$\hat{W}_k = \hat{W}_{qk} - (1 - e^{-\alpha_k t}) \left(\frac{\mu_k - \mu_0}{\mu_k + 1}\right) \hat{W}_{qk}. \tag{4.65}$$

This equation is convenient because $(\mu_k - \mu_0)$ will be zero for all eigenvalues that are equal to β_0^2, and those terms are thus eliminated from the computation. The expression will be used in following sections.

4.2. Signal-to-Noise Optimization

It is well known that a uniformly weighted array gives the maximum signal-to-noise ratio when the noise contributions from the element channels have equal power and are uncorrelated. These conditions are approximately valid when receiver noise and uniformly distributed sky noise are the predominant noise contributions; they pertain exactly in linear array antennas with half-wave spacing. However, when there is directional interference from other in-band transmitters, from jammers, or from natural phenomena, the noise out of the element channels will be correlated, and uniform weighting will not optimize signal-to-noise ratio. The solution to the general problem is readily obtained by the elegant mathematical approach of maximizing ratios of quadratic forms. References 24, 25, and 26 are recommended for a discussion of the optimization procedure and a more detailed mathematical treatment. Other optimization procedures and alternate performance measures may also be found described in the literature [14,21,27-39].

Maximum signal-to-noise (S/N) ratio per se is not really the desired object of our optimization, because we are willing to compromise on S/N ratio to buy some control over the quiescent steered-beam characteristics. For example, it may be desirable to control the main-beam shape, sidelobe levels, pattern null placements, or array phase center. Since these desired constraints, or controls, must be incorporated in the input beam-steering vector $\mathbf{B}^*$, it follows that one should optimize on equivalent signal vector $\mathbf{B}$. Thus, let us assume that the array output signal power desired is given by the equivalent expression

$$s = |\mathbf{W}^t\mathbf{B}|^2. \tag{4.66}$$

The array output noise power is assumed to derive from the quiescent receiver channel noise plus the noise signals received from external sources of interference, as defined in Eq. (4.2) for the element channel components of $\mathbf{E}$. Output noise power is therefore given by

$$n = \overline{|\mathbf{W}^t\mathbf{E}|^2}, \tag{4.67}$$

and we can formulate our signal-to-noise performance index as a ratio of these two quadratic forms:

$$\frac{s}{n} = \frac{|\mathbf{W}^t\mathbf{B}|^2}{\overline{|\mathbf{W}^t\mathbf{E}|^2}}. \tag{4.68}$$

Equation (4.68) can be manipulated readily into a ratio of Hermitian matrix forms, as

$$\frac{s}{n} = \frac{[\mathbf{W}^t\mathbf{B}]^*[\mathbf{B}^t\mathbf{W}]}{[\overline{\mathbf{W}^t\mathbf{E}}]^*\overline{[\mathbf{E}^t\mathbf{W}]}} = \frac{\mathbf{W}^{*t}[\mathbf{B}^*\mathbf{B}^t]\mathbf{W}}{\mathbf{W}^{*t}\overline{[\mathbf{E}^*\mathbf{E}^t]}\mathbf{W}}$$

or

$$\frac{s}{n} = \frac{\mathbf{W}^{*t}\mathbf{A}\mathbf{W}}{\mathbf{W}^{*t}\mathbf{M}\mathbf{W}}, \tag{4.69}$$

where A is a positive, semidefinite, Hermitian matrix (a one-term dyad) and M is the positive, definite, Hermitian covariance matrix described in Eqs. (4.23) through (4.28). In accordance with the procedure outlined in Ref. 26, the optimization of Eq. (4.69) results in the eigenvalue expression

$$\mathbf{A}\mathbf{W} = \frac{s}{n}\mathbf{M}\mathbf{W}, \tag{4.70}$$

where s/n now represents an eigenvalue. The maximum value of s/n which shall be denoted with a zero subscript, as $(s/n)_0$, is the largest eigenvalue of Eq. (4.70). Furthermore, because of the properties of the matrixes involved, it also happens to be the only nonzero eigenvalue. The unique eigenvector $\mathbf{W}_0$ associated with eigenvalue $(s/n)_0$ therefore represents the optimum element weights. Thus we have

$$\mathbf{A}\mathbf{W}_0 = \left(\frac{s}{n}\right)_0 \mathbf{M}\mathbf{W}. \tag{4.71}$$

Substituting for $(s/n)_0$ from Eq. (4.69) and cancelling the common term $(\mathbf{B}^t\mathbf{W}_0)$, one obtains

$$\mathbf{B}^* = \left(\frac{\mathbf{W}_0^{*t}\mathbf{B}^*}{\mathbf{W}_0^{*t}\mathbf{M}\mathbf{W}_0}\right)\mathbf{M}\mathbf{W}_0. \tag{4.72}$$

The quotient on the right-hand side is just a complex number, which we shall denote by C. The desired optimum weight vector is then obtained by inversion of Eq. (4.72), or

$$\mathbf{W}_0 = \frac{1}{C}[\mathbf{M}^{-1}\mathbf{B}^*]. \tag{4.73}$$

Hence, the optimum weights may be obtained directly by inverting the known (or estimated) covariance matrix.

It is interesting to examine Eq. (4.72) under the assumption of quiescent conditions, whereby the covariance matrix would be $\mathbf{M}_q$, as in Eq. (4.27), and the "optimum" weight must be $\mathbf{W}_q$, from Eq. (4.4), by definition. The quotient term reduces to unity for

$$\mathbf{B}^* = \mathbf{M}_q\mathbf{W}_q, \tag{4.74}$$

and Eq. (4.72) is then identical to Eq. (4.74). This establishes the optimum relationship for $\mathbf{B}^*$ when $\mathbf{W}_q$ has been chosen to satisfy desired quiescent beam characteristics. For the simple quiescent noise conditions assumed in this discussion, $\mathbf{M}_q$ is a diagonal matrix

and results in $\mathbf{B}^*$ components being equal to the $\mathbf{W}_q$ components multiplied by constants. Recall that these constants were denoted as b_k in Eq. (4.12) and that we evaluated the b_k in Eq. (4.61).

If Eq. (4.74) is substituted into Eq. (4.72) for the general case, our control law for optimum weights becomes

$$B^* = \mathbf{M}_q \mathbf{W}_q = C\mathbf{M}\mathbf{W}_0 \tag{4.75}$$

where

$$C = \left(\frac{\mathbf{W}_0^{*t}\mathbf{M}_q\mathbf{W}_q}{\mathbf{W}_0^{*t}\mathbf{M}\mathbf{W}_0}\right). \tag{4.76}$$

This optimum control law can be converted into orthonormal system variables by multiplying through from the left with $\mathbf{Q}^*$ and substituting for $\mathbf{W}_0$ from Eq. (4.52), whereupon

$$\mathbf{Q}^*\mathbf{B}^* = C\mathbf{Q}^*\mathbf{M}\mathbf{Q}^t\hat{\mathbf{W}}_0$$

$$\hat{\mathbf{B}}^* = C[\beta_i^2\delta_{ij}]\hat{\mathbf{W}}_0$$

or

$$\hat{\mathbf{W}}_0 = \frac{1}{C}\left[\frac{\delta_{ij}}{\beta_i^2}\right]\hat{\mathbf{B}}^*. \tag{4.77}$$

Equation (4.77) is the basis for the $\hat{W}_{ok}$ defined in Eq. (4.46), since the kth component of the above $\mathbf{W}_0$ vector may be written as

$$\hat{W}_{ok} = \left(\frac{\gamma}{C}\right)\left(\frac{1}{\mu_k}\right)\hat{B}_k^* \tag{4.78}$$

where $\mu_k = \gamma\beta_k^2$. The constant γ/C may be ignored, since $\mathbf{W}_0$ may be multiplied by any nonzero constant without changing the value of $(s/n)_0$. Thus, we have derived the necessary relationships for calculating the optimum weights from a known (or estimated) covariance matrix.

4.3. Q-Transformation Physical Network Analogy

The Q-matrix transformation as defined in Eq. (4.33) is a rather complicated mathematical matrix operator composed of normalized and mutually orthogonal eigenvectors. References 22 and 23 discuss the related eigenvalue problem and the procedures for finding these eigenvectors from known covariance matrix M. Fortunately, computer programs are available for carrying out the laborious calculations involved. Despite the complexity associated with their mathematical evaluation, however, Q-matrix eigenvectors have a relatively simple interpretation in terms of physical feed networks, and this interpretation will be presented here to give a better insight into the operation of adaptive arrays.

Essentially, the components of the eigenvectors may be interpreted as array element weights, giving rise to a set of orthogonal, normalized eigenvector beams. The ith eigenvector beam may be expressed in the form

$$g_i(\theta) = (\mathbf{S}^t \mathbf{e}_i) = \sum_{k=1}^{K} e_{ik} S_k \tag{4.79}$$

where S and its components S_k were defined in Eqs. (4.8) and (4.9), respectively. Next define a variable Z, related to spatial angle θ as

$$Z = e^{j2u} \tag{4.80}$$

where $u = (\pi d/\lambda) \sin \theta$, as defined in Eq. (4.10). The locus of Z is the unit circle in the complex Z plane. If we factor out the term S_1 from the summation of Eq. (4.79), $g_i(\theta)$ may be rewritten in the variable Z as

$$g_i(\theta) = \left(\frac{1}{\sqrt{Z}}\right)^{K-1} [e_{i1} + e_{i2}Z + e_{i3}Z^2 + \cdots + e_{iK}Z^{K-1}], \tag{4.81}$$

which expresses the eigenvector beam in familiar array polynomial form wherein the eigenvector components become the coefficients of the array polynomial.

From the work of Schelkunoff [40], we know that an array space factor $F(Z)$ has the two related forms

$$F(Z) = a_0 + a_1 Z + a_2 Z^2 + a_3 Z^3 + \cdots + a_{K-1} Z^{K-1} \tag{4.82}$$

or

$$F(Z) = a_{K-1}(Z - Z_1)(Z - Z_2)(Z - Z_3) \cdots (Z - Z_{K-1}); \tag{4.83}$$

i.e., it may be expressed either in the polynomial form or as the product of zero factors containing the roots of the polynomial. The roots $Z_1, Z_2, Z_3, \ldots, Z_{K-1}$ are the zeros or null points of the array space-factor pattern. Knowing the null points, one can solve for the array polynomial coefficients, or conversely, knowing the coefficients one can find the null points. All of the (K-1) null points will be located on the Z-plane unit circle.

Schelkunoff's null-point concept is particularly applicable to the patterns associated with adaptive arrays for the following reasons:

1. Adaptive arrays form nulls in the directions of interference sources.

2. An array of K elements possesses (K-1) degrees of freedom, which are represented by the (K-1) nulls. The behavior of adaptive arrays relates to how many degrees of freedom (or nulls) are "captured" by the interference environment.

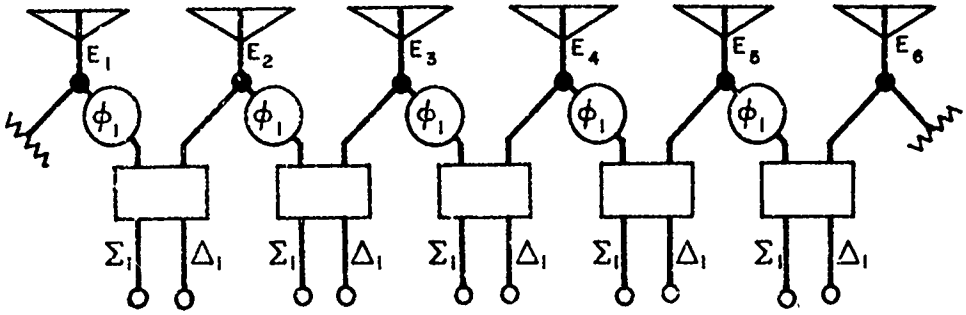

(a) Constraint of one null

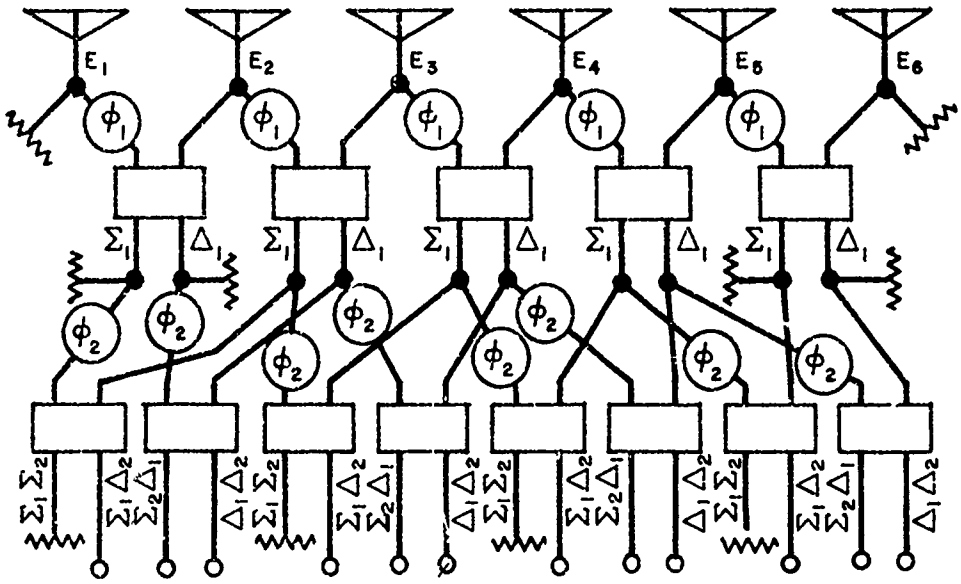

(b) Constraint of two nulls

Fig. 27—Davies null-control networks

3. Controlled null placement may be incorporated into the input beam-steering array weights.

4. Constrained null positions are usually associated with the eigenvector beams.

Networks in which independent control of pattern nulls is readily achieved have been described in the literature [41], and it is instructive to review their operation for a simple six-element array. Consider first the network shown in Fig. 27a, wherein one degree of freedom is consumed to accommodate the constraint of placing one null. We form an array of (K-1) "elements" in which the new "elements" are subapertures consisting of adjacent element pairs phased by ϕ_1 to the direction of an interference source. Each subaperture has a Σ_1 (sum) and Δ_1 (difference) output port. All of the Σ_1 ports contain power from the source, but the Δ_1 ports would receive little or no power because of the null being directed toward the source.

The network shown in Fig. 27b consumes two degrees of freedom to accommodate the constraint of placing two nulls. We now form an array of $(K\text{-}2)$ "elements" in which the new "elements" are subapertures consisting of three adjacent elements phased by ϕ_1 and ϕ_2 to the directions of two interference sources. Each subaperture has three outputs of interest, labeled $\Sigma_1\Delta_2$, $\Sigma_2\Delta_1$, and $\Delta_1\Delta_2$. The $\Sigma_1\Delta_2$ ports receive power from the source at θ_1 but none from the source at θ_2, and vice-versa for the $\Sigma_2\Delta_1$ ports. The unique $\Delta_1\Delta_2$ ports receive little or no power from either source because of the two directed nulls.

This network implementation of controlled nulls can be continued until all $(K\text{-}1)$ degrees of freedom have been consumed, whereupon one obtains a complete "Davies tree" matrix network, as shown in Fig. 28. The network has six output ports of interest to our discussion, and we can write the associated array pattern functions by inspection for half-wavelength element spacing, because Σ_j and Δ_j are simple cosine and sine functions:

$$\begin{aligned}
g_1'(\theta) &\approx (\Sigma_1\Delta_2\Delta_3\Delta_6\Delta_5) \\
g_2'(\theta) &\approx (\Delta_1\Sigma_2\Delta_3\Delta_4\Delta_6) \\
g_3'(\theta) &\approx (\Delta_1\Delta_2\Sigma_3\Delta_4\Delta_5) \\
g_4'(\theta) &\approx (\Delta_1\Sigma_2\Sigma_3\Delta_3\Delta_2) \\
g_5'(\theta) &\approx (\Sigma_1\Delta_2\Sigma_3\Delta_3\Delta_1) \\
g_6'(\theta) &\approx (\Delta_1\Delta_2\Delta_3\Delta_4\Delta_5)
\end{aligned} \tag{4.84}$$

where

$$\begin{aligned}
\Sigma_j &= \cos(u - u_j) \\
\Delta_j &= \sin(u - u_j).
\end{aligned} \tag{4.85}$$

We have K beams which may be used to resolve up to $(K\text{-}1)$ interference point sources. Note that the last beam $g_6'(\theta)$ is unique in that it alone contains all $(K\text{-}1)$ controlled nulls. This network represents an intuitive first approximation to the operation of the Q-matrix transformation because it is capable of achieving a shaped spatial coverage incorporating constrained null suppression of interference sources up to the limits of its degrees of freedom. However, except for those special cases involving orthogonal sets of uniform illumination beams, the network cannot serve as an exact analogy because all of the beams represented in Eq. (4.84) are tied together in a fixed relationship by the same $(K\text{-}1)$ null points, i.e., by the same phase shifters. This restrictive relationship prevents the beam array vectors from possessing the optimizing characteristics associated with true eigenvectors.

To achieve an exact representation for the Q-matrix transformation, each eigenvector must have its own $(K\text{-}1)$ null-controlled network, i.e., a network similar to the one associated with beam $g_6'(\theta)$ in Eq. (4.84). In addition, a multiplicative constant must be added to permit normalization. Figure 29 illustrates a simplified schematic of such a network for the ith eigenvector, where the orthonormal output voltage is $\hat{E}_i$ and the eigenvector beam may be written as

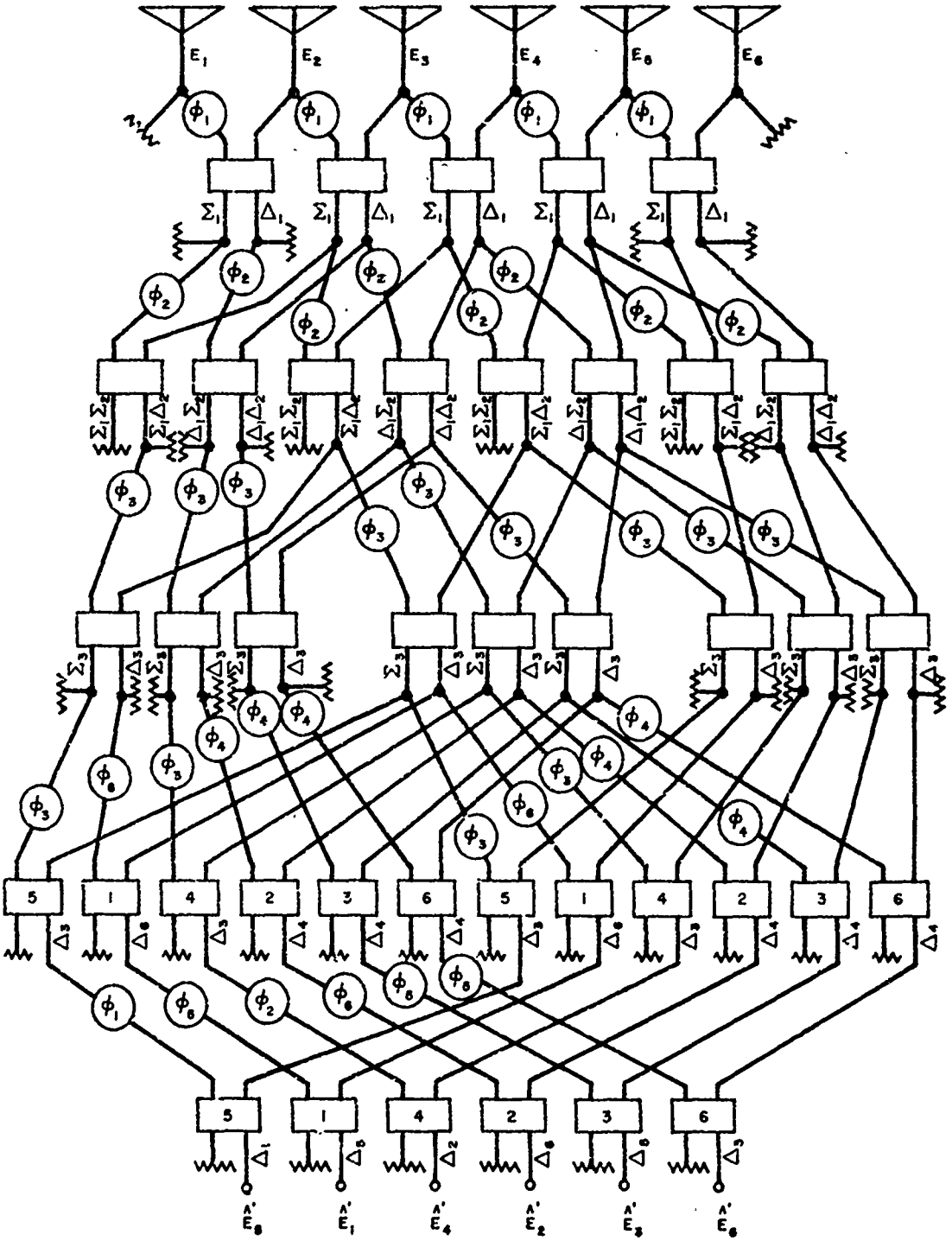

Fig. 28—Complete Davies null-control matrix network for six elements

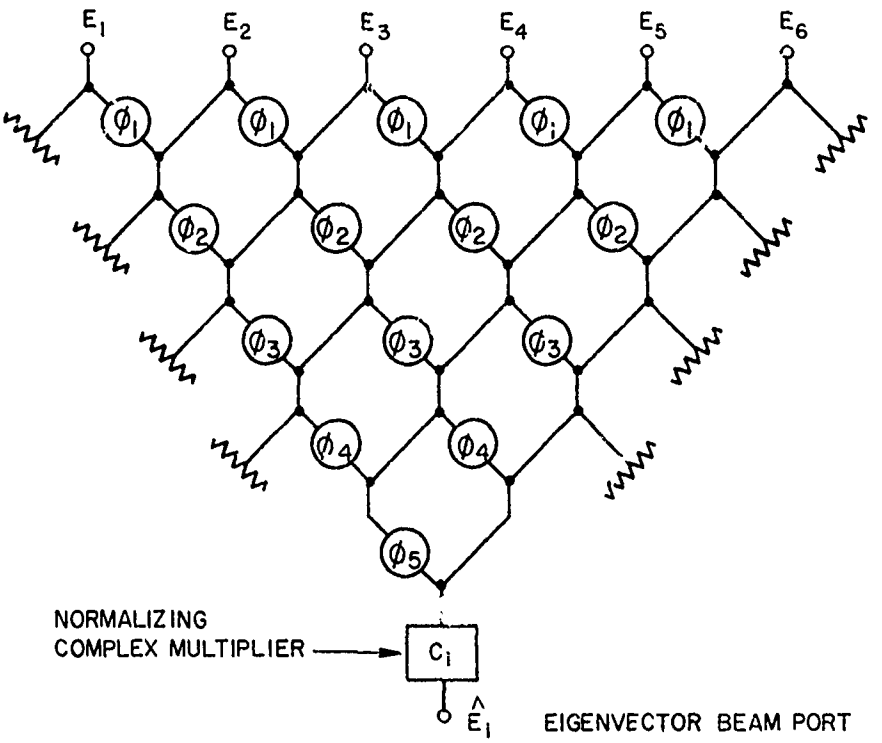

Fig. 29—Simplified schematic of $(K-1)$ controlled-null network representing one eigenvector of the Q-matrix transformation

$$g_i(\theta) = C_i\Delta_1\Delta_2\Delta_3\Delta_4\Delta_5 \,. \tag{4.86}$$

The output power from this network will be exactly equal to the eigenvalue β_i^2; recall from Eq. (4.39) that

$$(\hat{E}_i^*\hat{E}_i) = \beta_i^2. \tag{4.87}$$

Each null in Eq. (4.86) corresponds to a zero of the associated array space factor polynomial located on the Z-plane unit circle. If we denote Z_r as the rth zero, then from Eq. (4.80),

$$\begin{aligned}(Z - Z_r) &= e^{j2u} - e^{j2u_r} \\ &= j2e^{j(u+u_r)} \sin(u - u_r)\,,\end{aligned} \tag{4.88}$$

and we can readily convert Eq. (4.86) into the form of products of zero factors:

$$g_i(\theta) = \frac{C_i\zeta_i}{(2\sqrt{Z})^5}[(Z - Z_1)(Z - Z_2)(Z - Z_3)(Z - Z_4)(Z - Z_5)] \tag{4.89}$$

where

$$\zeta_i = e^{-j(u_1+u_2+u_3+u_4+u_5)}. \tag{4.90}$$

To demonstrate an application of the eigenvector network of Fig. 29, let us take the case of a single narrowband source located at angle θ_1. Eq. (4.31) shows that this single source would result in only one unique eigenvalue β_1^2; the other eigenvalues would be multiple roots assumed equal to β_0^2, the output receiver noise power (Eq. (4.59)). There would be only one unique eigenvector $\mathbf{e}_1$ associated with β_1^2; the other $(K-1)$ eigenvectors are not unique. Eigenvector $\mathbf{e}_1$ is found to be equal to

$$\mathbf{e}_1^t = \frac{1}{\sqrt{6}}\left[e^{j5u_1}, e^{j3u_1}, e^{ju_1}, e^{-ju_1}, e^{-j3u_1}, e^{-j5u_1}\right] \tag{4.91}$$

where

$$u_1 = \frac{\pi}{2} \sin\theta_1. \tag{4.92}$$

Note that the eigenvector phasing is simply the complex conjugate of the element signals received from the single source interference. From Eqs. (4.81) and (4.83), one obtains, for unique eigenvector beam $g_1(\theta)$,

$$g_1(\theta) = (\mathbf{S}^t\mathbf{e}_1) = \frac{1}{\sqrt{6(Z')^5}} F(Z') \tag{4.93}$$

$$F(Z') = 1 + Z' + (Z')^2 + (Z')^3 + (Z')^4 + (Z')^5 \tag{4.94}$$

or

$$F(Z') = (Z' - Z_0)(Z' - Z_0^2)(Z' - Z_0^3)(Z' - Z_0^4)(Z' - Z_0^5) \tag{4.95}$$

where

$$Z' = \left(\frac{Z}{Z_1}\right) = e^{j2(u-u_1)} \quad \text{and} \quad Z_0 = \left(\frac{Z_2}{Z_1}\right) = e^{j\pi/3}. \tag{4.96}$$

Equation (4.94) is recognized as a uniform-illumination array factor, and one can readily convert $g_1(\theta)$ to the familiar trigonometric form

$$g_1(\theta) = \frac{1}{\sqrt{6}} \frac{\sin 6\,(u - u_1)}{\sin\,(u - u_1)}. \tag{4.97}$$

Thus, the unique eigenvector beam is a uniform-illumination beam centered on the source at θ_1. Figure 30 shows the Z-plane unit circle with source point S_1 plus all five null points equally spaced around the circle by $2\pi/K$ rad. If the network phase shifters in Fig. 29 are set to produce the null points shown in Fig. 30, the correct eigenvector beam will be obtained.

The formation of the remaining nonunique eigenvectors can be accomplished easily for this single-source case by using the null points of Fig. 30 to successively center uniform

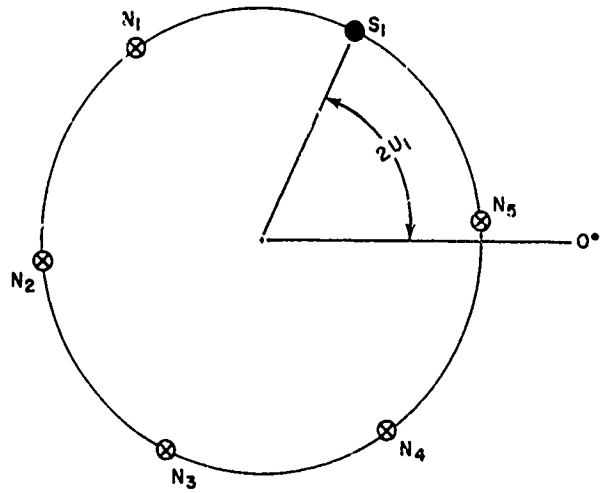

Fig. 30—Z-plane unit circle null locations for single-source case

illumination beams at N_1, N_2, N_3, N_4, and N_5. Note that each of these beams incorporates constrained null point S_1, which is the location of the jammer. This will result in a set of orthogonal, uniform illumination beams such as that obtained from a Butler matrix feed network. The associated eigenvectors are similar to $\mathbf{e}_1$ and result in the following complete $\mathbf{Q}$ matrix:

$$\mathbf{Q} = \frac{1}{\sqrt{6}} \begin{bmatrix} e^{j5u_1} & e^{j3u_1} & e^{ju_1} & e^{-ju_1} & e^{-j3u_1} & e^{-j5u_1} \\ e^{j5u_2} & e^{j3u_2} & e^{ju_2} & e^{-ju_2} & e^{-j3u_2} & e^{-j5u_2} \\ e^{j5u_3} & e^{j3u_3} & e^{ju_3} & \cdot & \cdot\cdot & \cdot \\ e^{j5u_4} & \cdot & \cdot & \cdot & \cdot & \cdot \\ e^{j5u_5} & \cdot & \cdot & \cdot & \cdot & \cdot \\ e^{j5u_6} & \cdot & \cdot & \cdot & \cdot & \cdot \end{bmatrix} . \tag{4.98}$$

If we use element signal components as defined for Eq. (4.2) with the single source located at θ_1, i.e., if

$$E_k = n_k + J_1 e^{ju_1(2k-7)}, \tag{4.99}$$

then the transformed orthonormal output signals are

$$\hat{\mathbf{E}} = \mathbf{QE} = \begin{bmatrix} (n_{01} + \sqrt{6}\, J_1) \\ n_{02} \\ n_{03} \\ n_{04} \\ n_{05} \\ n_{06} \end{bmatrix}, \tag{4.100}$$

where n_{0i} represents the summation of quiescent receiver noise voltages n_k at the ith output port. Define an input noise vector N consisting of the n_k,

$$\mathbf{N}^t = [n_1, n_2, n_3, n_4, n_5, n_6]\,. \tag{4.101}$$

Then

$$\hat{\mathbf{N}} = \mathbf{QN} \quad \text{or} \quad n_{0i} = (\mathbf{e}_i^t \mathbf{N}). \tag{4.102}$$

Cross-correlating any two of the output noise voltages, results in

$$\begin{aligned} \overline{(n_{0i}^* n_{0j})} &= \overline{(\mathbf{e}_i^{*t}\mathbf{N}^*)(\mathbf{N}^t\mathbf{e}_j)} \\ &= \mathbf{e}_i^{*t}\,[\overline{\mathbf{N}^*\mathbf{N}^t}]\,\mathbf{e}_j \\ &= \mathbf{e}_i^{*t}\,[|\bar{n}_k|^2\delta_{kl}]\,\mathbf{e}_j. \end{aligned} \tag{4.103}$$

If we assume equal magnitudes of receiver noise power in each channel, such that $|\bar{n}_k|^2 = |\bar{n}_0|^2$ for all k, then Eq. (4.103) may be written as

$$\overline{(n_{0i}^* n_{0j})} = |\bar{n}_0|^2(\mathbf{e}_i^{*t}\mathbf{e}_j) = \begin{cases} |\bar{n}_{0i}|^2 & \text{for } i = j \\ 0 & \text{for } i \neq j \end{cases}. \tag{4.104}$$

Thus, although each output-port noise consists of a mixture of all the input noise voltages, the outputs have zero cross-correlation because of the orthogonality of the Q-matrix eigenvectors. Also, the noise power at any output port equals the input receiver noise power, since eigenvectors are normalized to unity Hermitian length:

$$|\bar{n}_{0i}|^2 = \overline{(n_{0i}^* n_{0i})} = |\bar{n}_0|^2. \tag{4.105}$$

The squares of the absolute values of the orthonormal output signals in Eq. (4.100) equal the eigenvalues of the covariance matrix,

$$\begin{aligned} \beta_1^2 &= (|\bar{n}_0|^2 + 6|\bar{J}_1|^2) \\ \beta_i^2 &= |\bar{n}_0|^2 = \beta_0^2 \quad \text{for } i \neq 1, \end{aligned} \tag{4.106}$$

where we note that the power from the interference source appears at only one output port for this single-source case.

It is also of interest to see what is obtained for transformed input beam-steering vector $\hat{\mathbf{B}}^*$, from Eqs. (4.98) and (4.41). Since the eigenvectors are all uniform-illumination array factors, we have, from Eqs. (4.12), (4.61), and (4.5),

$$\begin{aligned}\hat{B}_i^* &= (\mathbf{e}_i^{*t}\mathbf{B}^*) \\ &= (1+\mu_0)(\mathbf{e}_i^{*t}\mathbf{W}_q) \\ &= \frac{1+\mu_0}{\sqrt{6}} \sum_{k=1}^{6} a_k e^{j(u_i-u_0)(2k-7)}. \end{aligned} \tag{4.107}$$

From Eq. (4.7), we see that the summation equals the value of the quiescent beam pattern at angle θ_i, or $G_q(\theta_i)$, so that $\hat{\mathbf{B}}^*$ is simply

$$\hat{\mathbf{B}}^* = \mathbf{Q}\mathbf{B}^* = \left(\frac{1+\mu_0}{\sqrt{6}}\right)\begin{bmatrix} G_q(\theta_1) \\ G_q(\theta_2) \\ G_q(\theta_3) \\ \vdots \\ G_q(\theta_6) \end{bmatrix}. \tag{4.108}$$

So we find that the components of $\hat{\mathbf{B}}^*$ are proportinal to the quiescent beam pattern sampled at the orthogonal eigenvector beam positions.

We have evaluated the complete $\mathbf{Q}$ transformation for the case of a single source of interference and have interpreted the eigenvalues and eigenvectors in terms of the physical network analogy of Fig. 29. Further application of this concept will be made in following sections for more complicated distributions of interference sources.

4.4. Retrodirective Eigenvector Beam Concept

A valuable insight into a fundamental principle of operation for adaptive arrays may be gained by examining the formation of retrodirective beams, as illustrated in Fig. 1. We saw in the previous section that for a single narrowband source of interference, we obtain one unique eigenvalue and one unique eigenvector which produces a uniform-illumination, retrodirective eigenvector beam centered on the source at θ_1, as given in Eq. (4.97). Note that even though a complete set of K orthogonal uniform-illumination beams was set up by the $\mathbf{Q}$-matrix transformation network, only one of those beams was retrodirective toward the jammer, and it was produced by the one unique eigenvector. It will be shown in this section that adaptive array pattern performance can be characterized by considering only the *unique*, *retrodirective* eigenvector beams; the arbitrary, nonunique eigenvector beams are not essential and need not be evaluated.

The necessary array output pattern function $G(\theta, t)$ can be derived most readily by considering the output of the orthonormal system of Fig. 25b for array input signal vector S, defined in Eq. (4.8) and recalling that the output must be identical for both the real system and the orthonormal system; i.e.,

$$G(\theta, t) = \sum_{i=1}^{K} W_i S_i = \sum_{i=1}^{K} \hat{W}_i \hat{S}_i \tag{4.109}$$

or

$$G(\theta, t) = (\hat{\mathbf{W}}^t \hat{\mathbf{S}}). \tag{4.110}$$

The vector $\hat{\mathbf{S}}$ of course results from the **Q**-matrix transformation operating on the input signal vector S:

$$\hat{\mathbf{S}} = \mathbf{Q}\mathbf{S}. \tag{4.111}$$

From Eq. (4.33) we see that ith component $\hat{S}_i$ would be given by

$$\hat{S}_i = (\mathbf{e}_i^t \mathbf{S}) = \sum_{k=1}^{K} e_{ik} S_k. \tag{4.112}$$

But this summation defines the ith eigenvector beam as in Eq. (4.79), so that

$$\hat{S}_i = (\mathbf{e}_i{}^t \mathbf{S}) = g_i(\theta) \tag{4.113}$$

or

$$G(\theta, t) = \sum_{i=1}^{K} \hat{W}_i g_i(\theta).$$

Thus, our output pattern function is a summation of the K eigenvector beams weighted by the orthonormal system adaptive weights.

A convenient equation for $\hat{W}_i$ has already been developed in Sec. 4.1 under the assumption that quiescent noise conditions hold up to time $t = 0$, when the external sources of interference are suddenly switched on. Repeating Eqs. (4.65) and (4.63), it was found that W_i may be written as

$$\hat{W}_i = \hat{W}_{qi} - (1 - e^{-\alpha_i t}) \left(\frac{\mu_i - \mu_0}{\mu_i + 1} \right) \hat{W}_{qi} \tag{4.114}$$

where

$$\hat{W}_{qi} = (\mathbf{e}_i^{*t}\mathbf{W}_q) = \sum_{k=1}^{K} e_{ik}^{*} W_{qk}. \tag{4.115}$$

$\hat{W}_{qi}$ is the Hermitian scalar product of the quiescent beam-steering vector $\mathbf{W}_q$ and the ith eigenvector. It represents the ith component of $\mathbf{W}_q$ in transformed orthonormal space. Note that at time $t = 0$, Eq. (4.114) reduces to $\hat{W}_i = \hat{W}_{qi}$, and Eq. (4.113) results in

$$G(\theta,0) = \sum_{i=1}^{K} \hat{W}_{qi} g_i(\theta) = (\hat{W}_q{}^t \hat{\mathbf{S}}) = (\hat{\mathbf{W}}_q{}^t \mathbf{Q}\mathbf{S}). \tag{4.116}$$

But from Eq. (4.52) we see that

$$\mathbf{W}_q{}^t = \hat{\mathbf{W}}_q{}^t \mathbf{Q} \tag{4.117}$$

or

$$G(\theta,0) = (\mathbf{W}_q{}^t \mathbf{S}) = G_q(\theta), \tag{4.118}$$

where quiescent beam pattern $G_q(\theta)$ was defined in Eq. (4.7). This result could be anticipated, of course, from the sampling properties of the orthonormal eigenvectors or merely from the fact that the quiescent outputs from the two systems must be identical.

The final step, then, is to substitute Eqs. (4.114) and (4.118) into Eq. (4.113), whereupon we obtain the desired relationship,

$$G(\theta,t) = G_q(\theta) - \sum_{i=1}^{K} (1 - e^{-\alpha_i t}) \left(\frac{\mu_i - \mu_0}{\mu_i + 1}\right) \hat{W}_{qi} g_i(\theta). \tag{4.119}$$

Recall that

$$\alpha_i = \frac{1 + \mu_i}{\tau_0},$$

$$\mu_i = \gamma \beta_i{}^2,$$

and

$$\mu_0 = \gamma \beta_0{}^2.$$

Thus, the output pattern function of our adaptively controlled linear array consists of two parts. The first part is quiescent beam pattern $G_q(\theta)$, and the second part, which

is subtracted from $G_q(\theta)$, is a summation of weighted, orthogonal, eigenvector beams. An important point in the weighting is that the numerator $(\mu_i - \mu_0)$ will be zero for all eigenvalues that are equal to quiescent eigenvalue β_0^2.

Therefore, one may disregard all β_0^2 associated eigenvector beams in the summation, retaining only the unique eigenvector beams, which also happen to be retrodirective. Another important point in the weighting is that the transient response time of the unique eigenvector beams is controlled by α_i, which is proportional to the eigenvalue. A large eigenvalue implies a fast transient response for its associated eigenvector beam, whereas a small eigenvalue results in slow response.

Let us first apply the above pattern function to the case of the single narrowband source located at angle θ_1, which was discussed in the previous section. Since there is only one unique eigenvalue β_1^2, we have only one nonzero term in the summation, so that Eq. (4.119) reduces to

$$G(\theta, t) = G_q(\theta) - (1 - e^{-\alpha_1 t})\left(\frac{\mu_1 - \mu_0}{\mu_1 + 1}\right) \hat{W}_{q1} g_1(\theta), \tag{4.120}$$

where $\alpha_1 = (1 + \mu_1/\tau_0)$ and $\mu_1 = \gamma\beta_1^2$. From Eq. (4.97) in the previous section,

$$g_1(\theta) = \frac{1}{\sqrt{K}}\left[\frac{\sin K(u - u_1)}{\sin (u - u_1)}\right], \tag{4.121}$$

and from Eqs. (4.107) and (4.7),

$$\hat{W}_{q1} = \frac{G_q(\theta_1)}{\sqrt{K}}. \tag{4.122}$$

From Eq. (4.106), β_1^2 was evaluated; it can be used to convert the servo gain factor term to a more meaningful form:

$$\beta_1^2 = (|\bar{n}_0|^2 + K|\bar{J}_1|^2)$$

$$\frac{\mu_1}{\mu_0} = \frac{\gamma(|\bar{n}_0|^2 + K|\bar{J}_1|^2)}{\gamma|\bar{n}_0|^2} = (1 + KP_1), \tag{4.123}$$

where P_1 is now the ratio of jammer power to receiver noise power at the preamplifiers. If μ_0 is set equal to unity, which would be normal practice for the circuit of Fig. 24, the servo gain term becomes

$$\left(\frac{\mu_1 - \mu_0}{\mu_1 + 1}\right) = \left(\frac{KP_1}{2 + KP_1}\right), \tag{4.124}$$

and Eq. (3.120) can be rewritten as

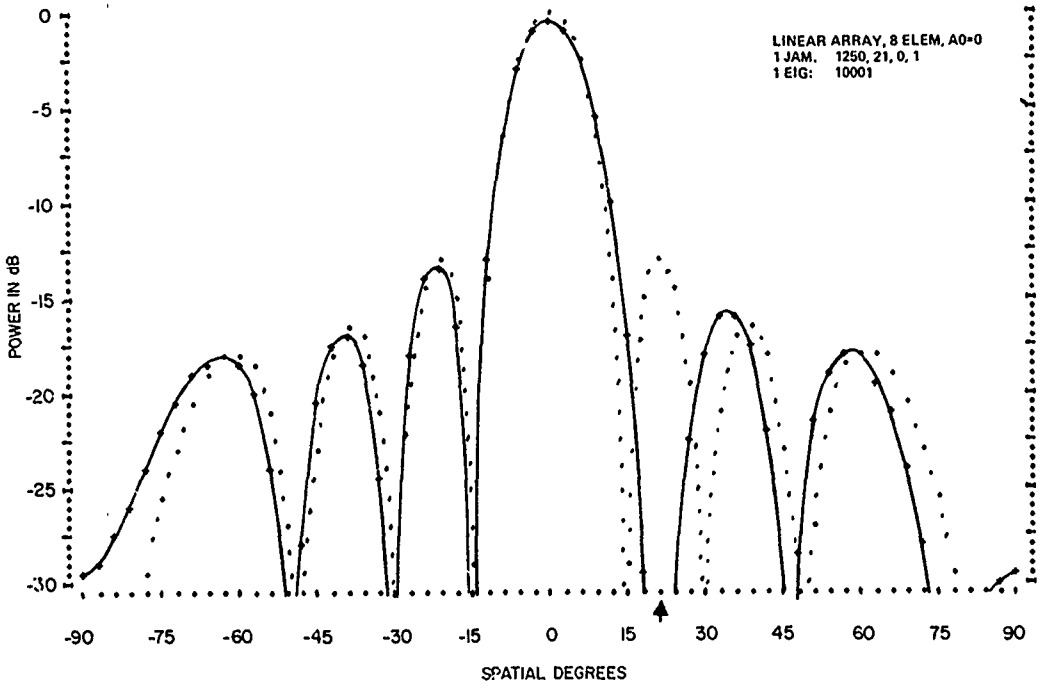

Fig. 31—Steady-state adapted pattern for single source, Case A; power ratio P_1 = 1,250, located at $\theta_1 = 21°$

$$G(\theta, t) = G_q(\theta) - (1 - e^{-\alpha_1 t})\left(\frac{P_1 G_q(\theta_1)}{2 + KP_1}\right)\left(\frac{\sin K(u - u_1)}{\sin (u - u_1)}\right). \tag{4.125}$$

This gives us the performance for the single-jammer case in easily understood variables, without any need for either eigenvalues or eigenvectors.

To illustrate the use of Eq. (4.125), Fig. 31 is a plot of the quiescent $G_q(\theta)$ pattern (dotted line) and the steady-state adapted pattern (solid line) computed for an eight-element linear array (K=8) with a jammer of power ratio P_1 = 1250 in the first sidelobe, at $\theta_1 = 21°$. $G_q(\theta)$ was chosen as a uniform-illumination pattern steered to broadside. Figure 32 illustrates the two parts of the adapted pattern on an expanded angular scale: the quiescent $G_q(\theta)$ pattern (dotted line) and the retrodirective eigenvector beam pattern $g_1'(\theta)$ (solid line) which has been multiplied by its weighting factors, i.e.,

$$g_1'(\theta) = \left(\frac{P_1}{2 + KP_1}\right) G_q(\theta_1)\left(\frac{\sin K(u - u_1)}{\sin (u - u_1)}\right). \tag{4.126}$$

Note that the weighting factors cause the peak of the retrodirective eigenvector beam to become alined exactly with the sidelobe magnitude corresponding to the angular position of the jammer. This produces the deep null in the adapted pattern when the two parts

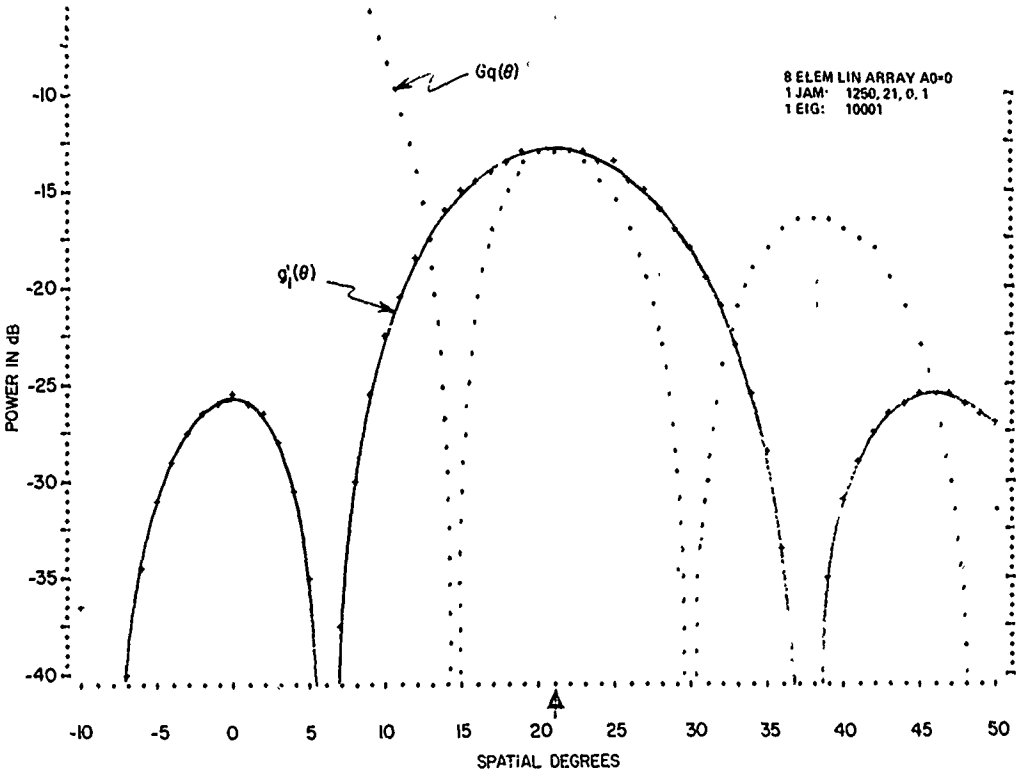

Fig. 32—Retrodirective eigenvector beam $g_1'(\theta)$ for single source, Case A

are subtracted, of course, and one can readily compute the depth of that null at the jammer position from Eq. (4.125):

$$\left(\frac{\sin K(u-u_1)}{\sin (u-u_1)}\right) = K \quad \text{for} \quad \theta = \theta_1$$

or

$$G(\theta_1, t) = \left[1 - (1 - e^{-\alpha_1 t})\left(\frac{KP_1}{2 + KP_1}\right)\right] G_q(\theta_1). \tag{4.127}$$

In the steady state $t = \infty$, Eq. (4.127) will reduce even further to the simple form

$$G(\theta_1, \infty) = \left(\frac{2}{2 + KP_1}\right) G_q(\theta_1). \tag{4.128}$$

Thus, for strong jammers the gain is reduced by the considerable factor of the square of KP_1 in the direction of the jammer, effectively eliminating the jammer power from the output of the adapted array.

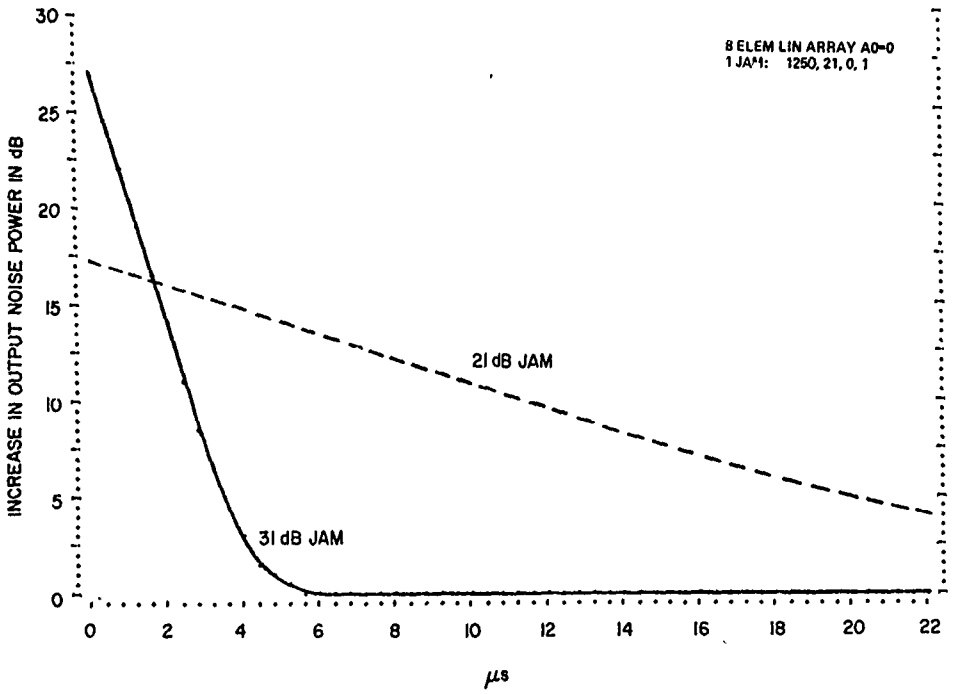

Fig. 33—Transient response for single source, Case A, for source power ratios of 21 dB and 31 dB; eigenvalues 1,001 and 10,001, respectively

Transient response can be shown conveniently by plotting the increase in output noise power, proportional to $P_1[G(\theta_1, t)]^2$ for this case, vs time. The values of $G(\theta_1, t)$ are calculated from Eq. (4.127). Figure 33 illustrates such a transient response (solid line) where $P_1 = 1{,}250$ and $T_0 = 12{,}750$ μs, which result in $\alpha_1 = 0.784$. The dashed-line plot was computed for 10 dB less jammer power $P_1 = 125$, whereby $\alpha_1 = 0.078$ and the convergence time is correspondingly ten times longer.

Next apply Eq. (4.119) to the case of two narrowband interference sources of nearly equal power ratios $P_1 = 1{,}250$ and $P_2 = 1{,}200$, close together in the first sidelobe of the quiescent pattern, at $\theta_1 = 18°$ and $\theta_2 = 22°$, respectively. If one forms the covariance matrix (Eq. (4.26)) for this case and solves for the unique eigenvalues and eigenvectors, the solutions listed in Table 1 are obtained. The exact procedure for arriving at these solutions will be discussed in Sec. 4.5. Note that there are two unique eigenvalues and two associated unique eigenvectors, but that the ratio of the two eigenvalues bears no relationship to the jammer powers, which are essentially equal in this case. Such widely different eigenvalue solutions will be found to be typical of situations in which sources are close together in terms of array beamwidth. Using the solutions for β_1^2, β_2^2, $\mathbf{e}_1$, and $\mathbf{e}_2$ from Table 1, we can evaluate the associated μ_i, α_i, $\hat{W}_{qi}$, and $g_i(\theta)$ for substitution into Eq. (4.119). Figure 34a illustrates the resulting steady-state adapted pattern (solid line) for our eight-element array, and Fig. 34b shows an expanded plot of the sidelobes in the immediate vicinity of the jammers.

Table 1
Eigenvalues and Eigenvectors for a Two-Source Case*

Eigenvector Coefficient	Amplitude	Phase Angle (deg)
1,1	0.340120	69.7477
1,2	0.351501	8.3626
1,3	0.359156	-53.03
1,4	0.363004	245.573
1,5	0.363004	184.175
1,6	0.359156	122.778
1,7	0.351501	61.3852
1,8	0.340120	0
2,1	0.537157	250.308
2,2	0.387808	188.701
2,3	0.234347	126.989
2,4	0.078413	64.5464
2,5	0.078413	185.762
2,6	0.234347	123.319
2,7	0.387808	61.607
2,8	0.537157	0

*Unique eigenvalues: 18,544.4 and 1,057.58.

Note that the pattern nulls are very closely alined with the positions of the two strong jammers in this case. In later examples, we will see cases where the nulls are not so well alined.

Figure 35 shows the components of the adapted pattern on an expanded angular scale: the quiescent $G_q(\theta)$ pattern (dotted line) and the two retrodirective eigenvector beam patterns $g_1'(\theta)$ (solid line) and $g_2'(\theta)$ (dashed line):

$$g_1'(\theta) = \hat{W}_{q1} g_1(\theta) \tag{4.129}$$

$$g_2'(\theta) = \hat{W}_{q2} g_2(\theta). \tag{4.130}$$

Beam $g_1(\theta)$ covers both sources in the manner of a centered sum beam, and its power gain of approximately 7.57 at the source locations leads to a total output power equal to the first eigenvalue:

$$\left(\frac{\beta_1^2}{\beta_0^2}\right) = 1 + P_1 g_1^2(\theta_1) + P_2 g_1^2(\theta_2)$$

$$= 1 + (1250 + 1200)7.57$$

$$= 18{,}544. \tag{4.131}$$

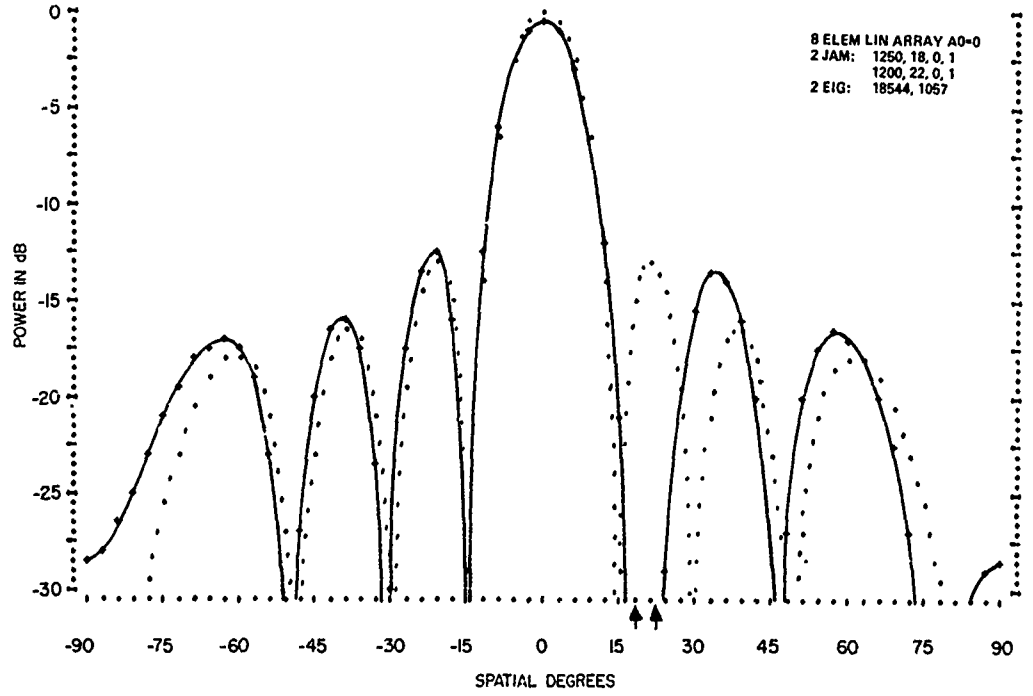

(a) Normal scale plot

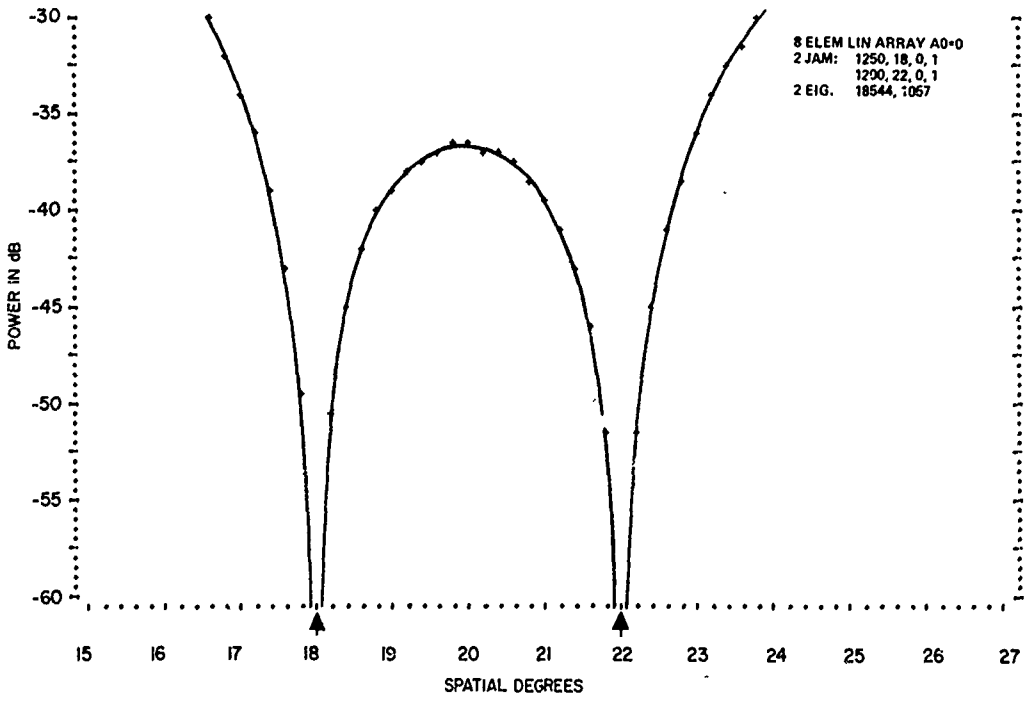

(b) Expanded sidelobe plot in source region

Fig. 34—Steady-state adapted pattern for two sources, Case B

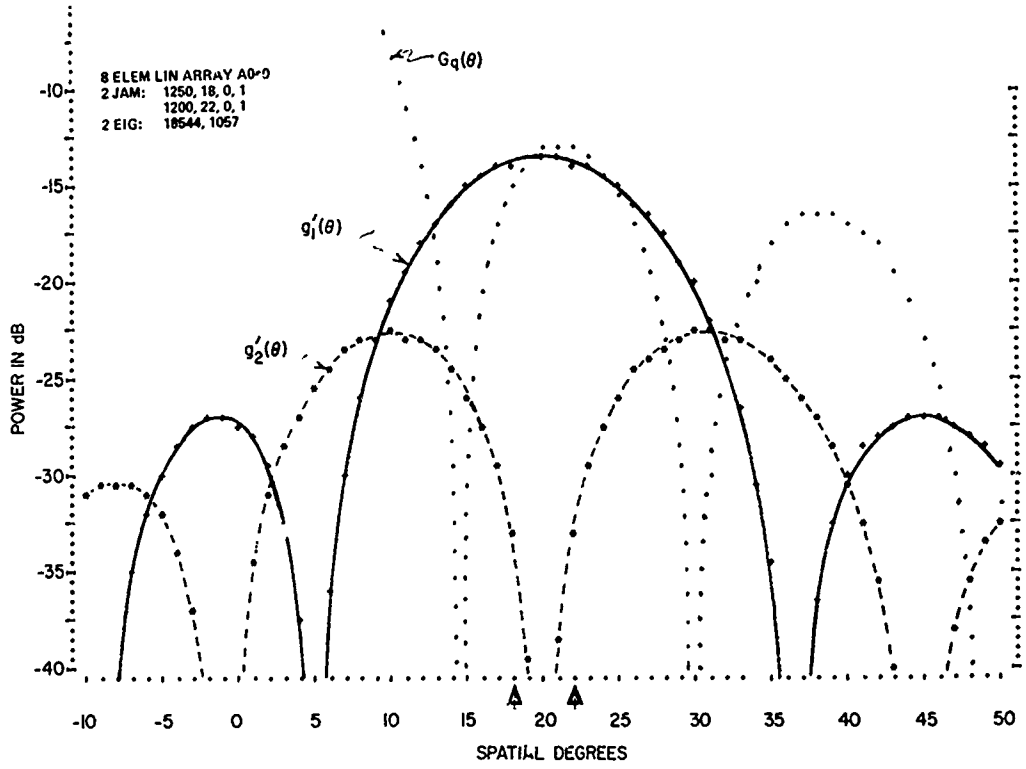

Fig. 35—Retrodirective eigenvector beams $g_1'(\theta)$ and $g_2'(\theta)$ for two sources, Case B

Note that the weighting factor $\hat{W}_{q1}$ does not aline the peak of $g_1(\theta)$ exactly with the sidelobe magnitude of either source, although it comes close enough that its subtraction would cause a null structure close to the final nulls in that sidelobe region. Eigenvector beam $g_2(\theta)$ splits the sources in the manner of a difference beam, and its power gain of approximately 0.43 at the source locations leads to a total output power equal to the second eigenvalue:

$$\left(\frac{\beta_2^2}{\beta_0^2}\right) = 1 + P_1 g_2^2(\theta_1) + P_2 g_2^2(\theta_2)$$

$$= 1 + (1{,}250 + 1{,}200)\,0.43$$

$$= 1{,}057. \qquad (4.132)$$

An interesting point here is that both eigenvector beams contain power from both of the sources, so that one may be curious as to how decorrelation is accomplished. To explain this, we start with the ith eigenvector beam output from Eq (4.37) and substitute the E vector components from Eq. (4.2):

$$\hat{E}_i = (\mathbf{e}_i^t \mathbf{E})$$

$$= (\mathbf{e}_i^t \mathbf{N}) + \sum_{r=1}^{2} J_r \sum_{k=1}^{K} e_{ik} e^{ju_r(2k-K-1)} \tag{4.133}$$

where N is the quiescent receiver noise vector defined in Eq. (4.101). The noise part is n_{0i}, as defined in Eq. (4.102), and from Eqs. (4.79) and (4.9) we see that the summation in k is simply the value of the eigenvector beam pattern at angle θ_r, or

$$g_i(\theta_r) = \sum_{k=1}^{K} e_{ik} e^{ju_r(2k-K-1)} \tag{4.134}$$

where

$$u_r = \frac{\pi d}{\lambda} \sin \theta_r.$$

Thus,

$$\hat{E}_i = n_{0i} + \sum_{r=1}^{2} J_r g_i(\theta_r). \tag{4.135}$$

From Eqs. (4.104, (4.39), and (4.59), the averaged correlations from (4.135) become

$$\overline{(\hat{E}_i^* \hat{E}_i)} = \beta_i^2 = |\bar{n}_0|^2 + \sum_{r=1}^{2} |\bar{J}_r|^2 g_i^2(\theta_r)$$

or

$$\left(\frac{\beta_i^2}{\beta_0^2}\right) = 1 + \sum_{r=1}^{2} P_r g_i^2(\theta_r) \tag{4.136}$$

$$\overline{(\hat{E}_1^* \hat{E}_2)} = 0 = |\bar{J}_1|^2 g_1(\theta_1) g_2(\theta_1) + |\bar{J}_2|^2 g_1(\theta_2) g_2(\theta_2). \tag{4.137}$$

Equation (4.137) shows that the zero cross-correlation can be related to the products of the voltage patterns; i.e., the product of $[g_1(\theta) g_2(\theta)]$ is positive when $\theta = \theta_1$ but negative when $\theta = \theta_2$. This equation may be further generalized to a summation for R jammer sources:

$$(\hat{E}_i^* \hat{E}_j) = |n_0|^2 \sum_{r=1}^{R} P_r g_i(\theta_r) g_i(\theta_r) = 0. \quad i \neq j \tag{4.138}$$

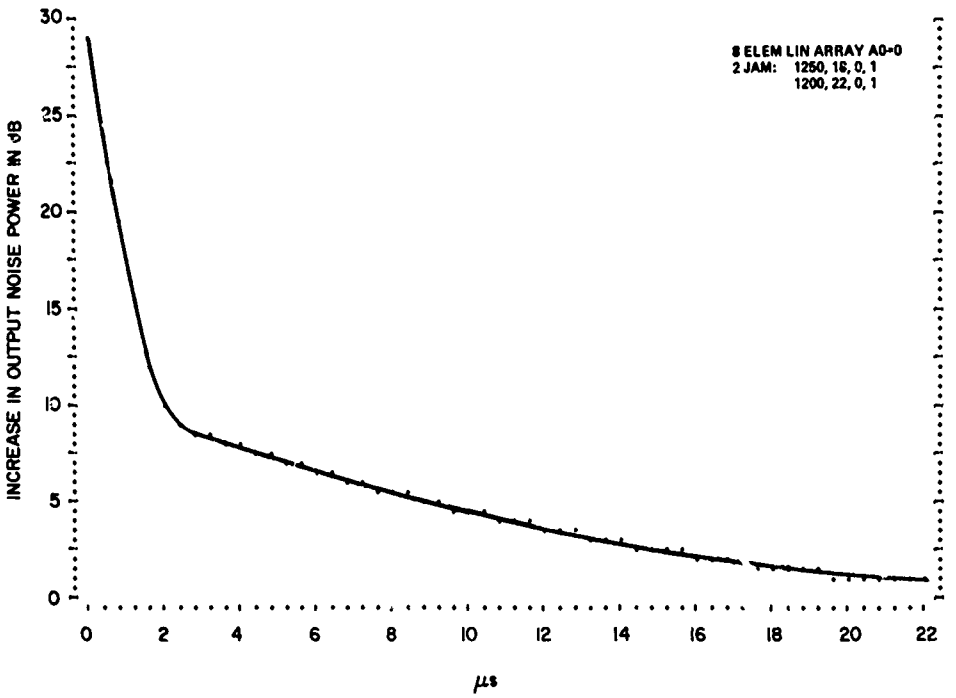

Fig. 36—Transient response for two sources, Case B; eigenvalues 18,544 and 1,058

Equation (4.136) is the basis for Eqs. (4.131) and (4.132). Since all of the terms in its summation must be positive or zero, the nonunique eigenvector beams that would result in $\beta_i^2 = \beta_0^2$ must incorporate nulls located precisely on the jammer positions.

Figure 36 shows the transient response for this two-jammer case, and one can readily see the two distinct slopes associated with the two different eigenvalues. The increase in output noise power for this case is proportional to

$$P_1 G^2(\theta_1, t) + P_2 G^2(\theta_2, t). \tag{4.139}$$

Eigenvector beam $g_1(\theta)$, with $\alpha_1 = 1.45$, attenuates both terms rapidly to the point where second eigenvector beam $g_2(\theta)$, with $\alpha_2 = 0.083$, takes over and completes the attenuation at its slower rate. An exact expression for the output noise power will be developed in the next section.

4.5. Performance Characteristics

Initial Conditions and Assumptions—The performance characteristics are calculated from the equations developed in Secs. 4.1 and 4.4. One initial condition already mentioned is that quiescent receiver noise is assumed to be the only system noise present up to time $t = 0$, when the entire selected distribution of external interference noise sources is switched on in a single step function. Another assumption already discussed is that the

receiver noise rms voltage in all element channels is equal and denoted by n_0, such that quiescent eigenvalue β_0^2 is the square of its rms value, as in Eq. (4.59), and thereby defines minimum, quiescent servo gain factor μ_0, as in Eq. (4.60). Repeating these for convenience, we have

$$\beta_0^2 = |\bar{n}_0|^2 \tag{4.140}$$

$$\mu_0 = \gamma\beta_0^2 = k^2 G|\bar{n}_0|^2 . \tag{4.141}$$

For the circuit of Fig. 24, it is convenient to choose unity for the value of μ_0, and we assume that amplifier gains G will be set accordingly.

Once μ_0 has been defined, it is convenient to express μ_i from Eq. (4.45) as a ratio of eigenvalues, such that

$$\frac{\mu_i}{\mu_0} = \left(\frac{\beta_i^2}{\beta_0^2}\right) \tag{4.142}$$

or

$$\mu_i = \mu_0\left(\frac{\beta_i^2}{\beta_0^2}\right).$$

This expression can be converted to jammer power ratios by Eq. (4.136), so that

$$\mu_i = \mu_0\left[1 + \sum_{r=1}^{R} P_r g_i^2(\theta_r)\right]; \tag{4.143}$$

This gives an expression similar to Eq. (3.49).

The next initial condition is to specify quiescent steered-beam pattern $G_q(\theta)$ and its associated set of quiescent weights $\mathbf{W}_q$, as defined in Eqs. (4.4) through (4.7). For purposes of this report, $G_q(\theta)$ is chosen to be a simple uniform-illumination beam formed by an eight-element linear array with elements spaced $\lambda/2$ apart;

$$K = 8 \text{ elements}$$

$$d = \lambda/2 \text{ element spacing}$$

$$a_k = 1 \text{ for all elements}$$

and

$$G_q(\theta) = \left(\frac{\sin 8\,(u - u_0)}{\sin\,(u - u_0)}\right) \tag{4.144}$$

where

$$u = \frac{\pi}{2} \sin\theta$$

$$W_{qk} = e^{-ju_0(2k-9)}.$$

Then the coefficients of input beam-steering vector $\mathbf{B}^*$ may be evaluated from Eqs. (4.61) and (4.12) as

$$b_k = (1 + \mu_0) = 2$$

$$B_k^* = b_k W_{qk} = 2e^{-ju_0(2k-9)}. \tag{4.145}$$

The maximum power condition must be considered in a manner similar to the single-loop case discussed in Sec. 3.2, and a relationship similar to Eq. (3.47) can be derived for the orthonormal servo loops of Fig. 25b, wherein the maximum servo gain factor μ_m is given by

$$\mu_m = \mu_0\left(\frac{\beta_m^2}{\beta_0^2}\right) = \left(\frac{\pi B_c \tau_0}{10}\right) - 1, \tag{4.146}$$

where β_m^2 represents the maximum eigenvalue to be handled, or the maximum power to be delivered, at any of the orthonormal output ports. Channel bandwidth B_c and basic filter time constant τ_0 are assumed to be the same for all element channel servo loops. Thus solving for τ_0 yields

$$\tau_0 = \left(\frac{10}{\pi B_c}\right)\left[1 + \mu_0\left(\frac{\beta_m^2}{\beta_0^2}\right)\right] \tag{4.147}$$

or

$$\tau_0 = \left(\frac{10}{\pi B_c}\right)\left[1 + \mu_0 + \mu_0 \sum_{r=1}^{R} P_r g_m^2(\theta_r)\right]. \tag{4.148}$$

Note that the maximum power, or maximum eigenvalue, will be much larger than jammer-to-receiver-noise power ratios P_r because the P_r are multiplied by the power gain of the retrodirective eigenvector beams. For example, in the single-source case discussed in connection with Fig. 32, $P_1 = 1{,}250$, and from Eq. (4.121),

$$g_1^2(\theta_1) = K = 8$$

or

$$\left(\frac{\beta_1^2}{\beta_0^2}\right) = [1 + P_1 g_1^2(\theta_1)] = 10{,}001.$$

Similarly, in the two-source case discussed in the previous section, we saw in Eq. (4.131) that the largest eigenvalue was 18,544, whereas P_1 was 1,250 and P_2 was 1,200.

For the cases to be considered, a value of 20,000 for μ_m will cover the largest eigenvalues, and if channel bandwidth B_c is kept at 5 Mc as in the single-loop case, then the value for τ_0 from Eq. (4.146) should be approximately 12,750 μs. Summarizing these selected constants, we have

$$\begin{aligned} \mu_m &= \left(\frac{\beta_m^2}{\beta_0^2}\right) \approx 20{,}000 \\ B_c &= 5 \text{ Mc} \\ \tau_0 &= 12{,}750 \ \mu\text{s}. \end{aligned} \tag{4.149}$$

Output Noise Power and S/N Degradation—The performance factor of ultimate interest in an adaptive array is the improvement in output signal-to-noise ratio as compared to a conventional array subject to the same interference conditions. In this ratio, the output noise power is fundamental to the improvement obtained and usually is sufficient by itself for illustrating the transient behavior of the system. To calculate it, we take advantage of the fact that the receiver noise is statistically independent of the external interference noise sources, so that we can add their separate output powers linearly.

Starting with receiver noise, the output contribution can be expressed in terms of either the real system or the orthonormal system in Fig. 25:

$$|Y_{0n}(t)|^2 = \sum_{k=1}^{K} |W_k n_k|^2 = \sum_{i=1}^{K} |\hat{W}_i n_{0i}|^2 \tag{4.150}$$

where n_{0i} was defined in Eq. (4.102). Substituting for $\hat{W}_i$ from Eq. (4.65) and for n_{0i} from Eq. (4.105) results in

$$|Y_{0n}(t)|^2 = |n_0|^2 \sum_{i=1}^{K} \left[1 - (1 - e^{-\alpha_i t})\left(\frac{\mu_i - \mu_0}{\mu_i + 1}\right)\right]^2 |\hat{W}_{qi}|^2 \tag{4.151}$$

or

$$|Y_{0n}(t)|^2 = |\bar{n}_0|^2 \sum_{i=1}^{K} [1 - A_i(t)]^2 |\hat{W}_{qi}|^2 \tag{4.152}$$

where

$$A_i(t) = (1 - e^{-\alpha_i t})\left(\frac{\mu_i - \mu_0}{\mu_i + 1}\right). \tag{4.153}$$

$A_i(t)$ will be zero for $t = 0$ and for $\mu_i = \mu_0$; i.e., for the nonunique eigenvalues. For quiescent conditions at $t = 0$, note that

$$|Y_{0n}(0)|^2 = |\bar{n}_0|^2 \sum_{i=1}^{K} |\hat{W}_{qi}|^2 = |\bar{n}_0|^2 \sum_{k=1}^{K} |W_{qk}|^2, \tag{4.154}$$

since the noise power output must be the same for either system. Thus, Eq. (4.152) may be rewritten as

$$|Y_{0n}(t)|^2 = |\bar{n}_0|^2 \sum_{k=1}^{K} |W_{qk}|^2 - \sum_{i=1}^{K} [2 - A_i(t)]\, A_i(t) |\hat{W}_{qi}|^2 \ . \tag{4.155}$$

This form is convenient because the $\hat{W}_{qi}$ associated with nonunique eigenvectors need not be evaluated, since $A_i(t) = 0$ for them.

The noise power contributed by R external interference sources is simply a summation of their output power pattern levels,

$$|Y_{0j}(t)|^2 = |\bar{n}_0|^2 \sum_{r=1}^{R} P_r G^2(\theta_r, t), \tag{4.156}$$

where P_r is the power ratio of the rth source, θ_r is its location, and $G(\theta_r, t)$ is given by Eq. (4.119).

Total output noise power is the summation of Eqs. (4.155) and (4.156), and the increase in output noise power is the ratio of these two to quiescent noise in Eq. (4.154):

$$\left(\frac{|Y_0(t)|^2}{|Y_{0n}(0)|^2}\right) = 1 + \left\{ \frac{\sum_{r=1}^{R} P_r G^2(\theta_r, t) - \sum_{i=1}^{K} [2 - A_i(t)]\, A_i(t) |\hat{W}_{qi}|^2}{\sum_{k=1}^{K} |W_{qk}|^2} \right\}. \tag{4.157}$$

This increase in output noise power is the quantity usually plotted for illustrating the transient behavior of the system. Figures 33 and 36 are examples of its application. A pertinent characteristic of this performance index is that it indicates the general magnitude of the adapted weights upon convergence to steady-state conditions; i.e., Eq. (4.157) can also be expressed in a form using the real weights,

$$\left(\frac{|Y_0(t)|^2}{|Y_{0n}(0)|^2}\right) = \left\{ \frac{\sum_{r=1}^{R} P_r G^2(\theta_r, t) + \sum_{k=1}^{K} |W_k|^2}{\sum_{k=1}^{K} |W_{qk}|^2} \right\}, \tag{4.158}$$

in which the effect of the magnitudes of the weights is obvious.

To normalize the effect of adapted-weight magnitude level, one can calculate the degradation D_{sn} in the S/N ratio. This is simply the quiescent S/N ratio divided by the adapted S/N ratio and leads to the convenient expression

$$D_{sn} = \left(\frac{G_q^2(\theta_s)}{G^2(\theta_s, t)}\right)\left(\frac{|Y_0(t)|^2}{|Y_{0n}(0)|^2}\right) \tag{4.159}$$

where the ratio in the second term is Eq. (4.157) or (4.158), the increase in output noise power. Thus, we simply multiply the previous performance index by the ratio of the power pattern values in the direction of the signal θ_s.

Covariance Matrix, Eigenvalues, and Eigenvectors—The eigenvalues and eigenvectors of the covariance matrix are evaluated as solutions to Eq. (4.31):

$$|M - \beta_i^2 \mathrm{I}| = 0 \quad \text{and} \quad \mathrm{M}\mathbf{e}_i = \beta_i^2 \mathbf{e}_i, \tag{4.158}$$

where the Hermitian covariance matrix $\underline{\mathrm{M}}$ is formed as indicated in Eqs. (4.23) through (4.28). Receiver noise power is assigned a level of unity for convenience in computation, since all noise powers are expressed as ratios to receiver noise power. Thus, quiescent noise matrix M_q becomes an identity matrix, and the individual rth-jammer covariance matrix is then multiplied by its power ratio P_r,

$$\mathrm{M}_q = \mathrm{I} \tag{4.159}$$

$$\mathrm{M} = \mathrm{I} + \sum_{r=1}^{R} P_r \mathrm{M}_r. \tag{4.160}$$

To incorporate bandwidth into the interference sources, the summation in Eq. (4.160) is further refined by dividing the jammer power spectrum into a number of discrete spectral lines as described in Sec. 3.3. We assume a uniform amplitude spectrum of uncorrelated lines spaced apart by a constant frequency increment, as illustrated in Fig. 17. If B_r denotes the percent bandwidth of the rth jammer and L_r its total number of spectrum lines, the power ratio and frequency offset of the lth line are given by

$$P_{rl} = \left(\frac{P_r}{L_r}\right) = \text{power ratio of spectrum line} \tag{4.161}$$

$$\Delta f_l = \left(\frac{B_r}{100}\right)\left[-\frac{1}{2} + \left(\frac{l-1}{L_r - 1}\right)\right] = \text{frequency offset} \tag{4.162}$$

The element spacing of half a wavelength in Eq. (4.144) must now be defined in terms of wavelength λ_0, which corresponds to the RF bandwidth center frequency f_0, and a new phase factor for the lth spectrum line is obtained,

$$d = \frac{\lambda_0}{2}. \tag{4.163}$$

Thus,

$$u_{rl} = \frac{f_l}{f_0}\frac{\pi}{2}\sin\theta_r = 1 + \frac{\Delta f_l}{f_0}\frac{\pi}{2}\sin\theta_r$$

or

$$u_{rl} = \left(1 + \left(\frac{B_r}{100}\right)\left[-\frac{1}{2} + \left(\frac{l-1}{L_r - 1}\right)\right]\right)\frac{\pi}{2}\sin\theta_r. \tag{4.164}$$

The covariance matrix may now be rewritten as a summation of the spectrum line matrixes $\mathbf{M}_{rl}$,

$$\mathbf{M} = \mathbf{I} + \sum_{r=l}^{R}\sum_{l=1}^{L_r} P_{rl}\mathbf{M}_{rl} \tag{4.165}$$

$$\mathbf{M}_{rl} = [\mathbf{S}_{rl}^{*}\mathbf{S}_{rl}^{t}] = \begin{bmatrix} 1 & e^{j2u_{rl}} & e^{j4u_{rl}} & \cdots \\ e^{-j2u_{rl}} & 1 & e^{j2u_{rl}} & \cdots \\ e^{-j4u_{rl}} & e^{-j2u_{rl}} & 1 & \cdots \\ \cdot & \cdot & \cdot & \cdot \\ \cdot & \cdot & \cdot & \cdot \\ \cdot & \cdot & \cdot & \cdot \end{bmatrix} \tag{4.166}$$

where

$$S_{rlk} = \exp\left[ju_{rl}(2k - K - 1)\right], \tag{4.167}$$

with u_{rl} defined in Eq. (4.164) and P_{rl} defined in Eq. (4.161). If m denotes the row and n the column, the mnth component of the $\mathbf{M}_{rl}$ matrix is equal to

$$(M_{rl})_{mn} = (S_{rlm}^{*}S_{rln}) = e^{j2u_{rl}(n-m)}. \tag{4.168}$$

Note that the calculations require four data values to be specified for each jammer:

P_r = ratio of total jammer power to receiver noise power,

θ_r = spatial angle location off boresight,

B_r = percent bandwidth of spectrum,

L_r = number of discrete spectrum lines.

Since the system cannot respond to noise outside of its element channel receiver bandwidth B_c, it is assumed that B_r would not be chosen to exceed B_c.

Having formed the complete covariance matrix for some chosen distribution of interference sources enables us to solve it for the eigenvalues and eigenvectors, using the Fortran computer program CMPLXEIG. This program was developed at the University of Wisconsin Computing Center [42].

Program CMPLXEIG prints out the eigenvalues and their corresponding eigenvectors. For a K-element array, there will be K eigenvalues and K eigenvectors. The minimum value β_0^2 that the eigenvalues can have is unity, which corresponds to receiver noise power level, and many selected distributions of sources result in multiple roots (eigenvalues) equal to unity. Such unity solutions for the eigenvalues are called *nonunique** eigenvalues, and the corresponding eigenvectors printed out are generally meaningless vectors. The useful eigenvectors printed out are those associated with the *unique* eigenvalues and, for CMPLXEIG, these are defined as eigenvalues greater than 1.01, which corresponds to an eigenvector beam delivering jammer power not less than 20 dB below the receiver noise level. This limit for qualifying the unique eigenvalues is a matter of judgment and may be selected within rather wide limits of perhaps 1.001 to 1.1 for our purposes. Based on this limit criterion, the unique eigenvectors corresponding to the unique eigenvalues are culled from the CMPLXEIG output, normalized to obtain unit vectors in the Hermitian sense, and then saved in a data file. All vector data output corresponding to the nonunique unity eigenvalues is discarded at this point; Table 1 in Sec. 3.4 is a typical illustration of the unique eigenvalue and unique eigenvector data saved from the output of CMPLXEIG. All performance characteristics are then computed from the saved data.

Although the nonunique eigenvectors are unnecessary for calculating system performance, situations may arise in which it becomes desirable to operate with a filled **Q** matrix. For these situations, one must construct the missing arbitrary, nonunique eigenvectors. A convenient approach to accomplishing this task is outlined in Appendix B.

Selected Distribution of Interference Sources—The performance characteristics of several selected distributions of interference sources have been calculated to demonstrate the behavior of our eight-element linear adaptive array. The distributions selected are listed in Table 2, where they are identified by case symbols A through H. For each case, the covariance matrix is formed as described above, and the associated unique eigenvalues and eigenvectors are computed. From these, output pattern function $G(\theta, t)$ is evaluated by using Eq. (4.119), under the assumptions discussed above. The transient performance is usually evaluated from the increase in output noise power, given by Eq. (4.157) or a modification thereof to include bandwidth. If the magnitude of the adapted weights changes appreciably, however, transient performance is evaluated on the basis of the degradation in the S/N ratio, given by Eq. (4.159).

Case A corresponds to a single narrowband source in the sidelobe region, one unique eigenvalue (10,001), and one unique eigenvector. This case was discussed in considerable detail in Sec. 4.3 and 4.4, with the adapted pattern shown in Fig. 31 and the transient performance shown in Fig. 33. It should be emphasized that these performance plots are very sensitive to the location of the jammer with respect to the quiescent steered-beam

*It is possible, though rare, to get nonunique eigenvalues (multiple roots) that are greater than unity. For such cases, the solutions must be retained as if they were unique.

Table 2
Selected Distributions of Interference Sources

Case	Interference Sources					Unique Eigenvalues	
	Number of Sources	Power Ratios	Location Angle (Deg)	Bandwidth (%)	Spectrum Lines	Number	Values
A	1	1,250	21	0	1	1	10,001
B	2	1,250	18	0	1	2	18,544
		1,200	22	0	1		1,058
C	2	1,250	18	0	1	2	10,812
		125	22	0	1		190
D	4	40	18	0	1	4	11,616
		125	25	0	1		2,486
		400	33	0	1		406
		1,250	42	0	1		16.5
E1	1	1,250	42	0	1	1	10,001
E2	1	1,250	42	2	3	2	9,986
							16.4
E3	1	1,250	42	15	16	3	9,529
							469
							4.7
F	1	1,250	5	0	1	1	10,001
G	3	1,100	36	26	11	6	13,316
		1,100	48	21	11		9,692
		1,100	66	19	11		3,091
							296
							10.5
							1.16
H	6	1,100	-66	19	11	8	13,532
		1,100	-48	21	11		13,386
		1,100	-36	26	11		12,619
		1,100	36	26	11		9,682
		1,100	48	21	11		3,224
		1,100	66	19	11		350
							14.7
							1.18

pattern. For example, if the single jammer happens to be located in a null of the quiescent pattern, then even though the one degree of freedom involved has been consumed, the single eigenvector beam will be deleted by the weighting factor $\hat{W}_{q1} = 0$, the adapted pattern will suffer no change from quiescent, and there will be no transient response. The position in Fig. 31, with the jammer located at the peak of the first sidelobe, represents a typical worst case for sidelobe jamming. The adapted pattern must shift its sidelobes to accommodate the jammer, but there is little distortion in the main beam because only one degree of freedom of the available seven has been consumed.

Case B has two narrowband sources in the sidelobe region, with almost equal power ratios and located close together; two unique eigenvalues (18,544 and 1,058); and unique eigenvectors (see Table 1). This case was discussed in detail in Sec. 4.4, with patterns shown in Figs. 34 and 35 and transient response shown in Fig. 36. Important points demonstrated by this case include the widely different eigenvalues, the two different eigenvector beams, and the relatively slow convergence time even though both jammers are strong.

Case C is the same as Case B except that the power ratio of the source at 22° is reduced 10 dB below that of the source at 18°; there are two unique eigenvalues (10,812 and 190). Note again that the ratio of the eigenvalues is much different from the ratio of the two jammer powers. Since the locations of the two sources are the same as in Case B, the steady-state adapted pattern for this case is almost exactly as in Fig. 34. The unique eigenvectors, however, are different and give rise to different retrodirective eigenvector beams, as shown in Fig. 37. Note that the beam shapes remain similar to those in Fig. 35, but that both $g_1'(\theta)$ and $g_2'(\theta)$ are shifted to the left so the respective peak and null fall very close to the position of the strongest source. This provides the proper power balance for achieving decorrelation between their outputs. The transient response shown in Fig. 38 is much slower than that of Fig. 36 because of the much smaller second eigenvalue.

Case D has four narrowband sources in the sidelobe region, unequal power ratios, and moderate spacing; there are four unique eigenvalues (11,616, 2,486, 406, and 17). The steady-state adapted pattern is shown in Figs. 39a and 39b, which include an expanded scale plot in the vicinity of the sources. Here we note that the four sources have "captured" four nulls, or four degrees of freedom out of seven available, and that this large percentage of null constraints causes an appreciable distortion of the main beam as well as of the remaining sidelobe region. This is a good illustration of the fact that adaptive pattern nulls usually do not aline themselves exactly on the source locations unless the sources are very strong. The retrodirective eigenvector beams are illustrated in Figs. 40a and 40b and are associated with the eigenvalues as listed below.

Eigenvalue	Eigenvector Beam
11,616	$g_1'(\theta) = \hat{W}_{q1} g_1(\theta)$
2,486	$g_2'(\theta) = \hat{W}_{q2} g_2(\theta)$
406	$g_3'(\theta) = \hat{W}_{q3} g_3(\theta)$
17	$g_4'(\theta) = \hat{W}_{q4} g_4(\theta)$

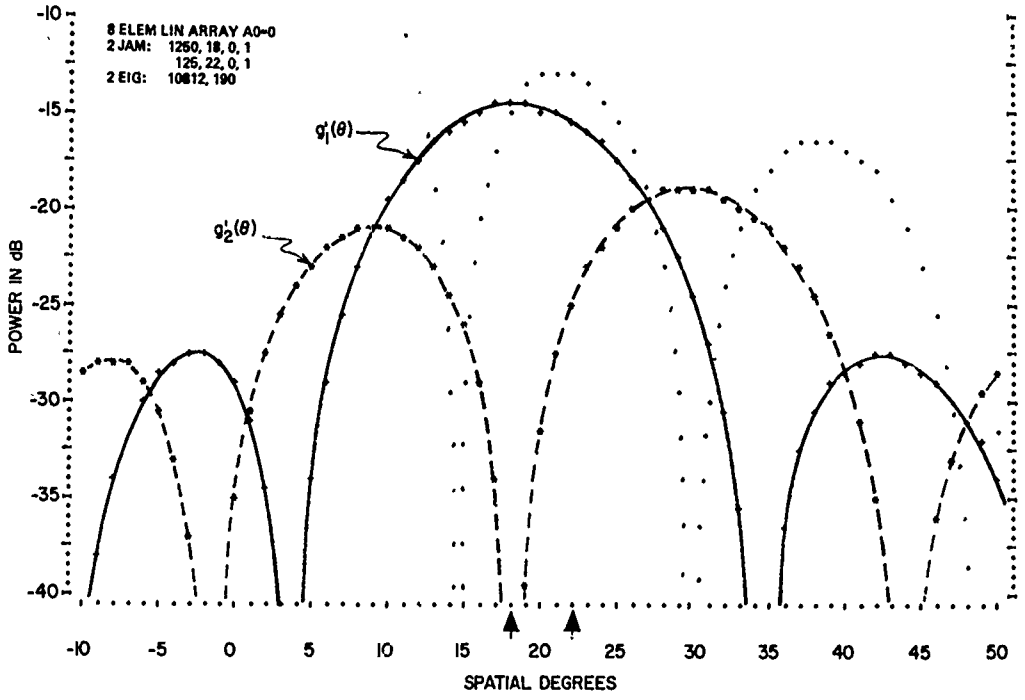

Fig. 37—Retrodirective eigenvector beams, $g_1'(\theta)$ and $g_2'(\theta)$, for two sources, Case C

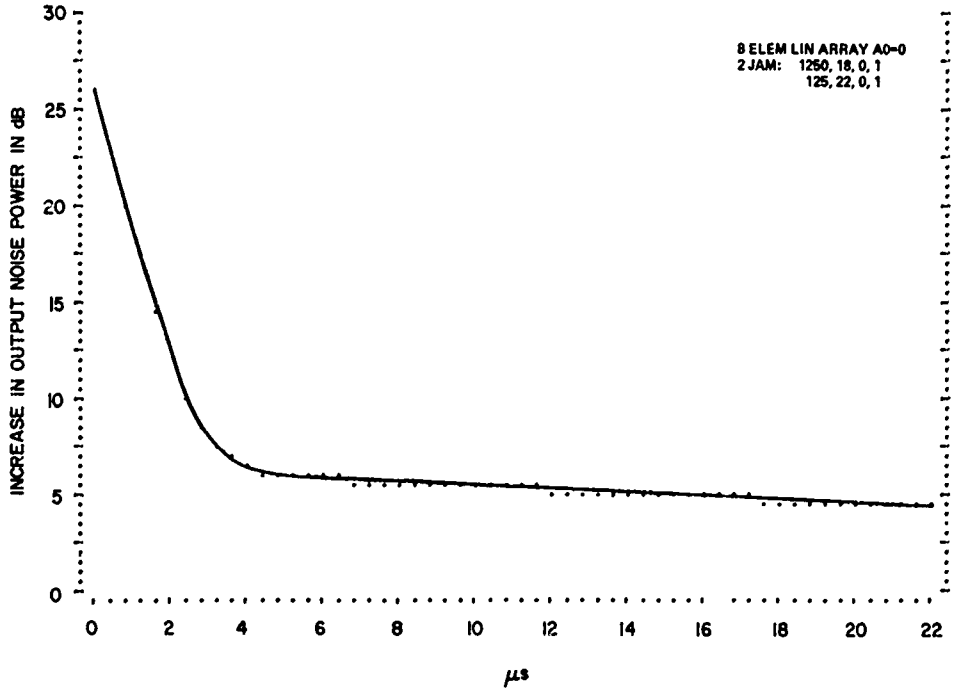

Fig. 38—Transient response for two sources, Case C; eigenvalues 10,812 and 190

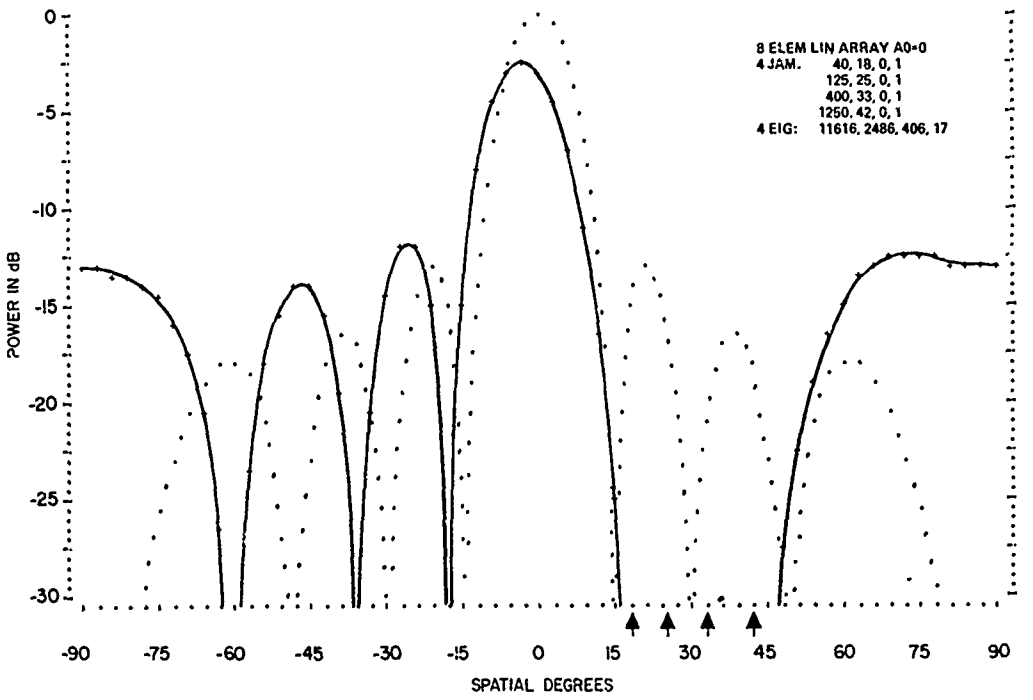

(a) Normal scale plot

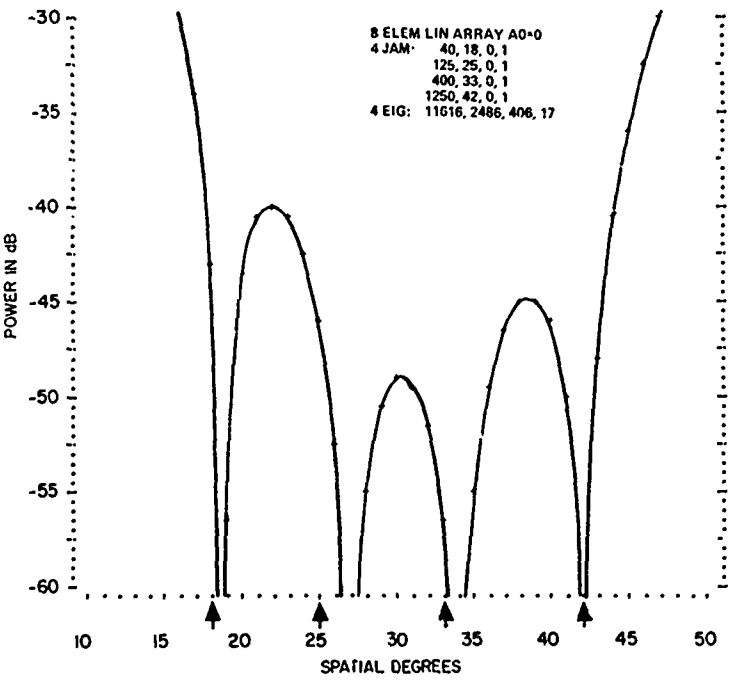

(b) Expanded sidelobe plot in source region

Fig. 39—Steady-state adapted pattern for four sources, Case D

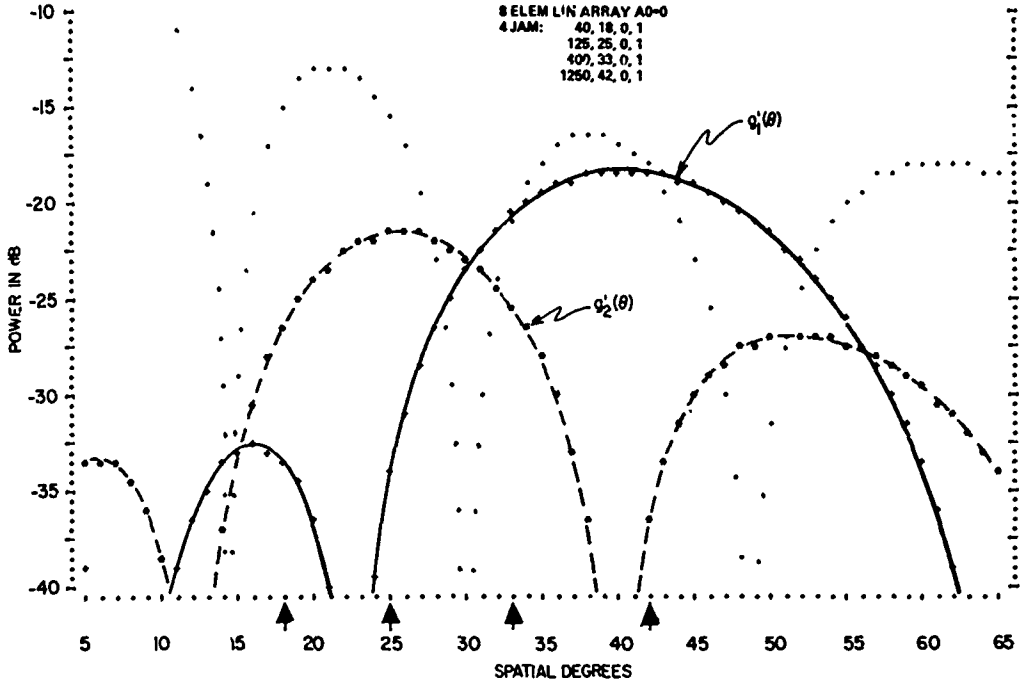

(a) Beams $g_1'(\theta)$ and $g_2'(\theta)$

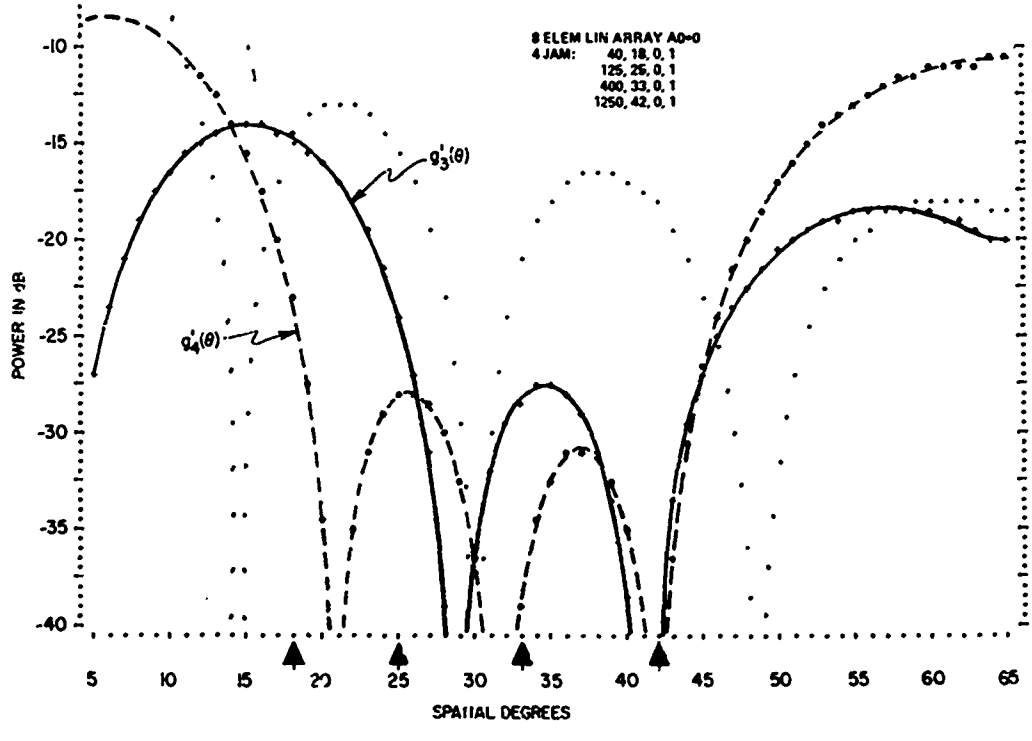

(b) Beams $g_3'(\theta)$ and $g_4'(\theta)$

Fig. 40—Retrodirective eigenvector beams for four sources, Case D

Beam $g_1(\theta)$ receives power from all four sources but functions essentially in the manner of a "sum" beam for the two strongest sources, thus accounting for the largest eigenvalue. Beam $g_2(\theta)$ also receives power from all four sources, but it functions essentially in the manner of a "difference" beam, which places its difference null so as to balance off the three weaker sources against the strong source. Beam $g_3(\theta)$ essentially nulls out the strongest source and favors the summation of the other three. It is a "single lobe in notch" type of pattern. Beam $g_4(\theta)$ brackets the four sources with a "double lobe in notch" pattern in which the two strongest sources are essentially nulled out. Its low gain on the remaining two weak sources accounts for the smallest eigenvalue.

Note that the eigenvector beams become progressively more complicated and less recognizable as to their function as we proceed toward the smaller eigenvalues. In fact, it seems meaningless to refer to beam $g_4(\theta)$ as a retrodirective beam since there is no main lobe as such, and none of its several high lobes points toward the sources. However, the dominant consideration is still its characteristics in the directions of the sources so as to satisfy Eqs. (4.136) and (4.138), and in that sense the pattern is retrodirective.

The transient response for this case is shown in Fig. 41, where it will be noted that D_{sn} is the ordinate because the weight magnitude drops about 25% for this case. Note also that the time scale is a combined linear and logarithmic scale with the transition point at $t = 6$ μs. The log scale permits better assessment of the long convergence time caused by the two smallest eigenvalues. Also note that the steady-state degradation in S/N is about 1.5 dB.

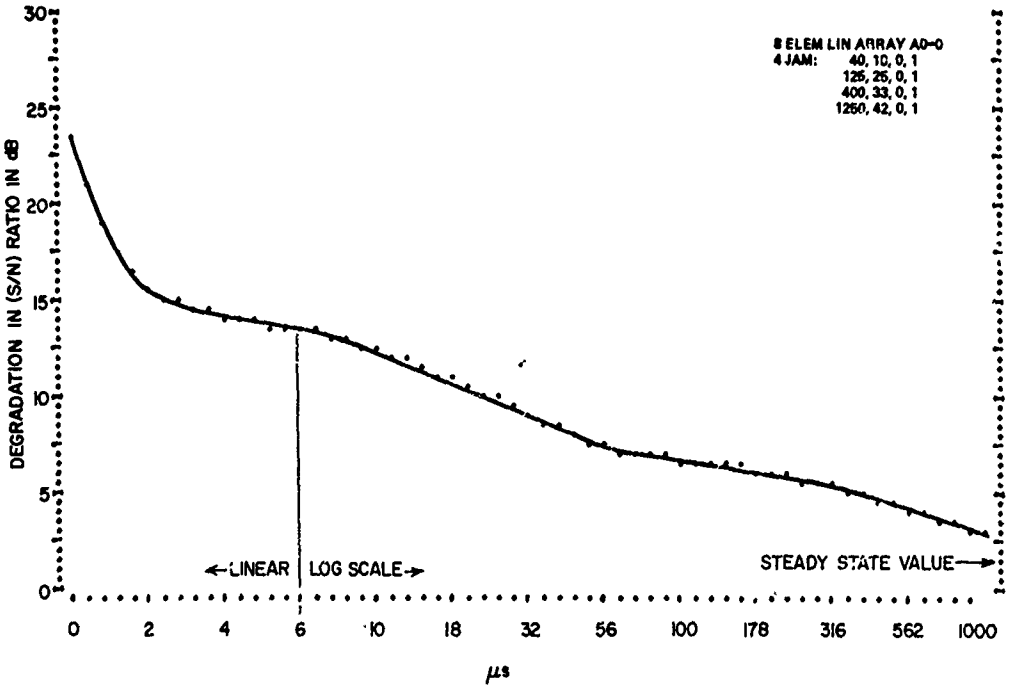

Fig. 41—Transient response for four sources, Case D; eigenvalues 11,616, 2,486, 406, and 17

Case E has a single source in the sidelobe region, 42° off array boresight; various bandwidths are used to demonstrate the effect of this parameter on our frequency-sensitive adaptive array.

E1 (zero bandwidth) has one unique eigenvalue (10,001). This narrowband case is the same as Case A except for source location angle, and the two cases may be compared to illustrate the dependence on location. The steady-state adapted pattern is shown in Fig. 42a and serves as the starting point in this bandwidth series of patterns. As in Case A, the source "captures" only one degree of freedom (one null), corresponding to the single, unique, uniform-illumination eigenvector beam.

Case E2 (2-percent bandwidth) has two unique eigenvalues (9,986 and 16). The steady-state adapted pattern is shown in Fig. 42b, where it is evident that a significant change has occurred in the sidelobe region. Even with this small amount of bandwidth, the single source has captured two degrees of freedom (two nulls), and the corresponding two unique eigenvector beams would be similar to those shown in Fig. 35 for Case B, i.e., a "sum" and a "difference" beam. A helpful property of this case is that the two eigenvector beams function effectively up to a source bandwidth of approximately 10 percent under the conditions assumed here, so that the extra captured degree of freedom results in considerable adjustment accommodation to changes in bandwidth. It provides the mechanism for obtaining a deep sidelobe notch of variable width.

Case E3 (15-percent bandwidth) has three unique eigenvalues (9,529, 469, and 5). The steady-state adapted pattern is shown in Figs. 43a and 43b, which include an expanded scale plot in the vicinity of the source. The equivalent spatial extent of the source is indicated for its 15% bandwidth. The single source has now captured three degrees of freedom (three nulls) out of seven available, and the resulting distortion in the adapted pattern is very evident. The corresponding three unique eigenvector beams are shown in Fig. 44 and are associated with the eigenvalues as follows.

Eigenvalue	Eigenvector Beam
9,529	$g_1'(\theta) = \hat{W}_{q1} g_1(\theta)$
469	$g_2'(\theta) = \hat{W}_{q2} g_2(\theta)$
5	$g_3'(\theta) = \hat{W}_{q3} g_3(\theta)$

The "sum" and "difference" beams, $g_1'(\theta)$ and $g_2'(\theta)$ respectively, are representative for any of the bandwidths tested in this series, from 2% to 20%; i.e., this pair of beams remains practically invariant. Beam $g_3'(\theta)$ is a "deep-notch" pattern which is similar to its counterpart in Fig. 40b except that the single lobe within the notch has a peak of −46 dB and thus does not show here. This third eigenvector beam comes into play at a bandwidth of roughly 7% and, except for the notch region and its lobe, the pattern undergoes very little change for the bandwidths tested, up to 20%.

The transient responses for four different values of source bandwidth are plotted in Fig. 45. In general, convergence rate slows down as bandwidth increases, because of the small eigenvalues generated. To compute these curves from the basic output noise power equation (Eq. (4.159)), we modified the source power summation to incorporate a

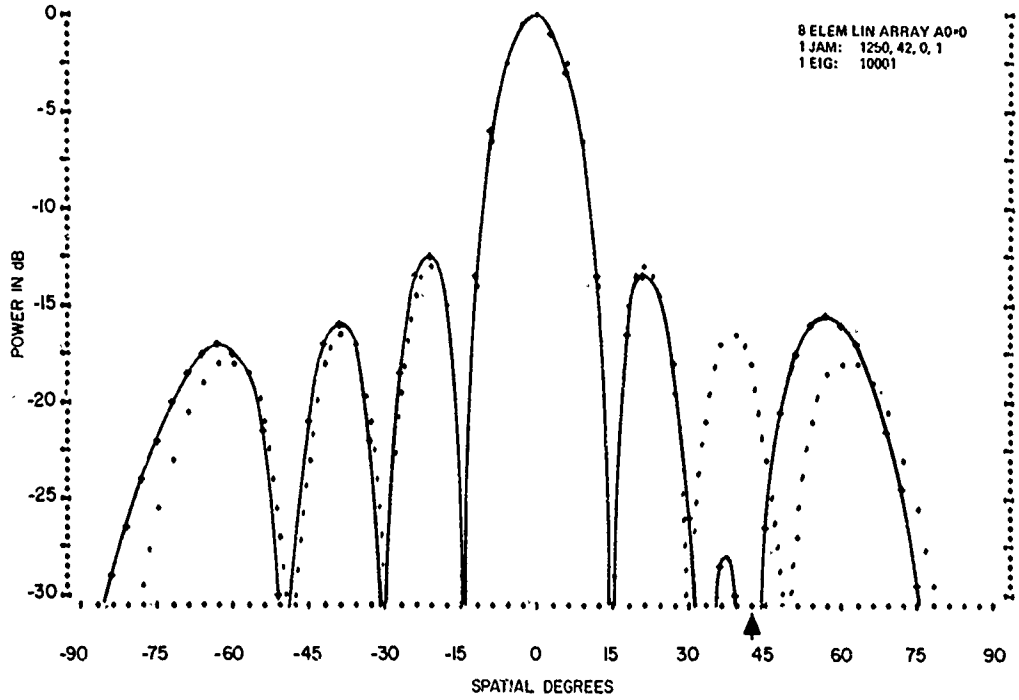

(a) Case E1—zero bandwidth

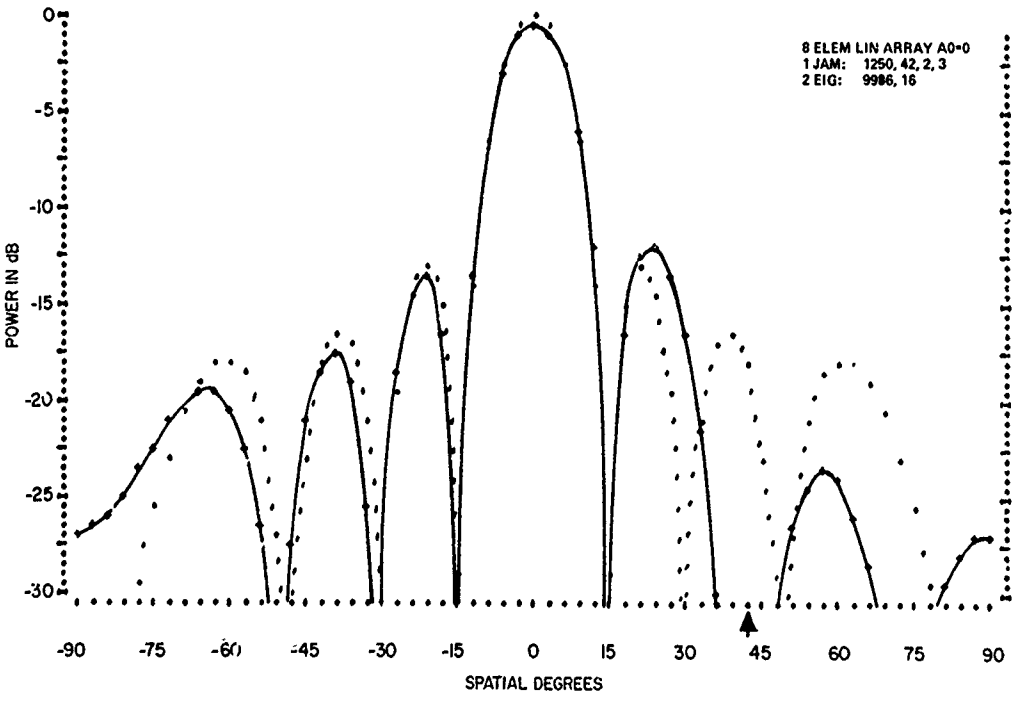

(b) Case E2—2% bandwidth

Fig. 42—Steady-state adapted pattern for single source with bandwidth, Case E

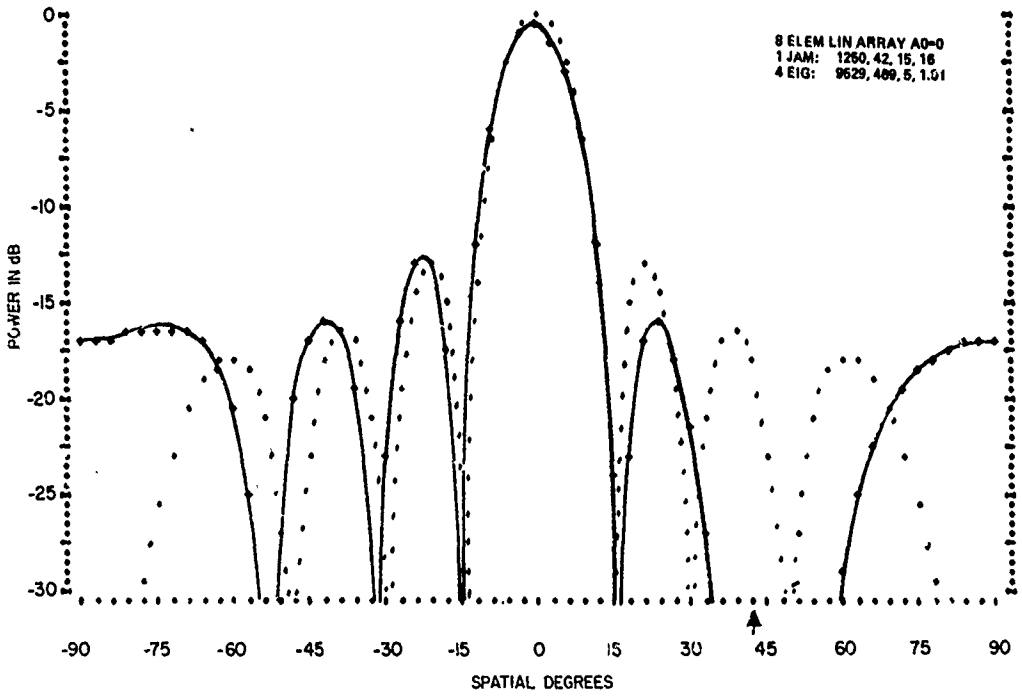

(a) Normal scale plot

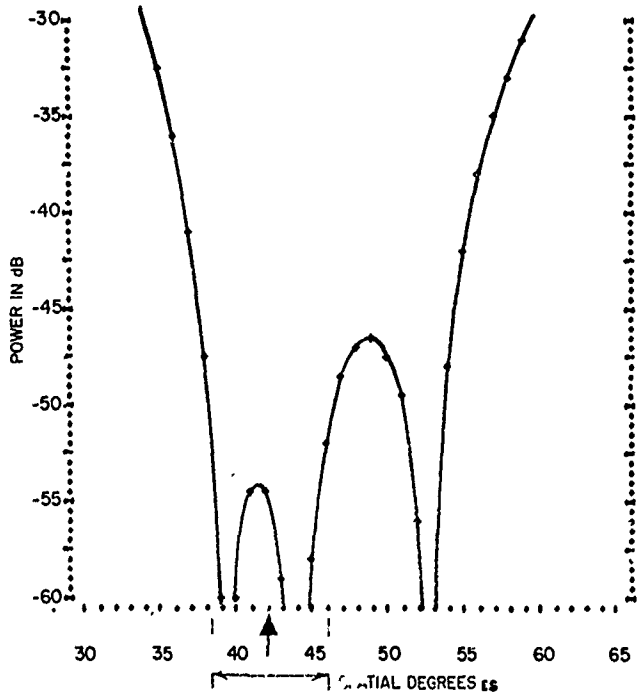

(b) Expanded sidelobe plot in source region

Fig. 43—Steady-state adapted pattern for single source with 15% bandwidth, Case E3

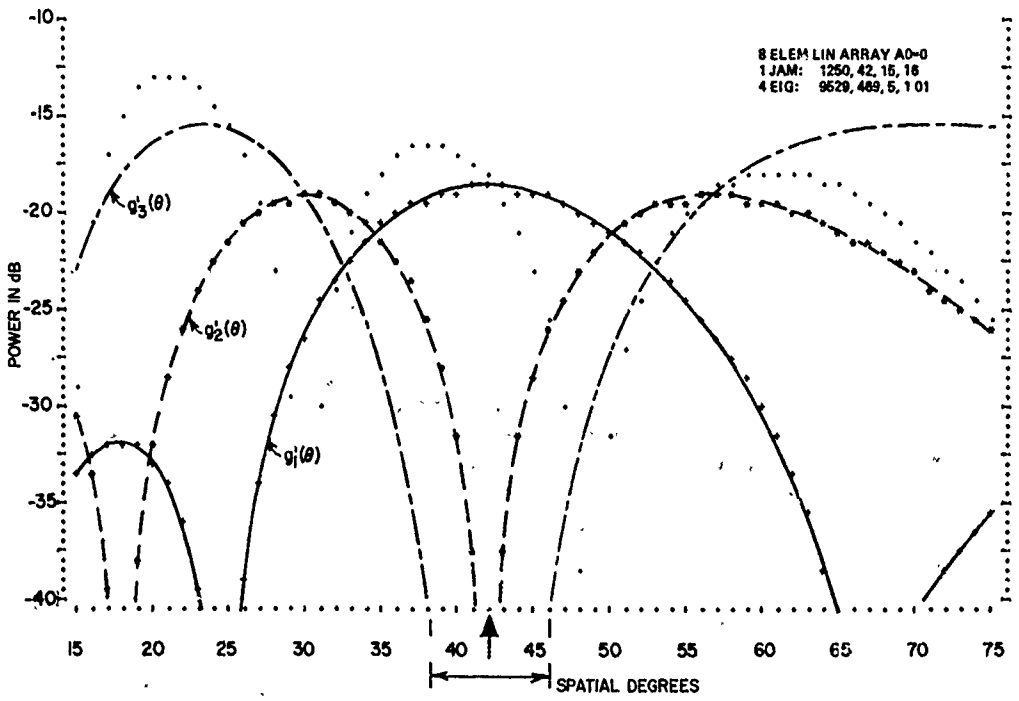

Fig. 44—Retrodirective eigenvector beams for single source with 15% bandwidth, Case E3

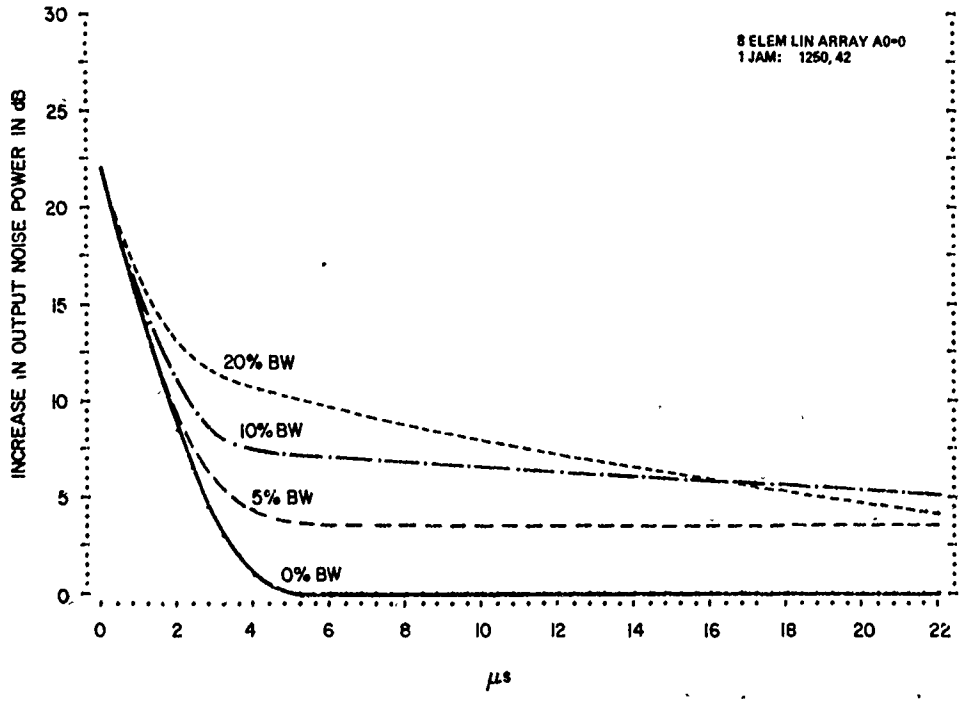

Fig. 45—Transient response for single source with bandwidth, Case E

summation of spectrum-line contributions over the bandwidth of the source, in the same manner as discussed in the previous subsection. Thus,

$$\text{source power} = \sum_{r=1}^{R} \sum_{l=1}^{L_r} P_{rl} G_l^2(\theta_r, t) \tag{4.169}$$

where P_{rl} is the spectrum-line power ratio given by Eq. (4.161) and $G_l(\theta_r, t)$ is the output pattern function for the lth spectrum line which requires the modified phase factor u_{rl}, given by Eq. (4.164), for its evaluation.

Case F has a single narrowband source in the main-beam region, 5° off array boresight; there is one unique eigenvalue (10,001). This case demonstrates the effects of main-beam jamming, but one should keep in mind that it is the same as Case A and Case E1 except for source location angle. The source captures only one degree of freedom (one null) corresponding to the unique, uniform-illumination eigenvector beam. The steady-state adapted pattern is shown in Fig. 46, where it is evident that main-beam jamming produces rather severe distortions in the output pattern. An inspection of Eq. (4.125), which specializes the output pattern function to the single narrowband source case, reveals that if the main-beam steering direction θ_0 happens to become alined with the source direction θ_1, then the main beam may practically disappear. In fact, if the quiescent pattern happens to be of uniform illumination, as we assumed for these calculations (Eq. (4.144)), then the entire output pattern function would indeed disappear (go to zero) for $\theta_0 = \theta_1$.

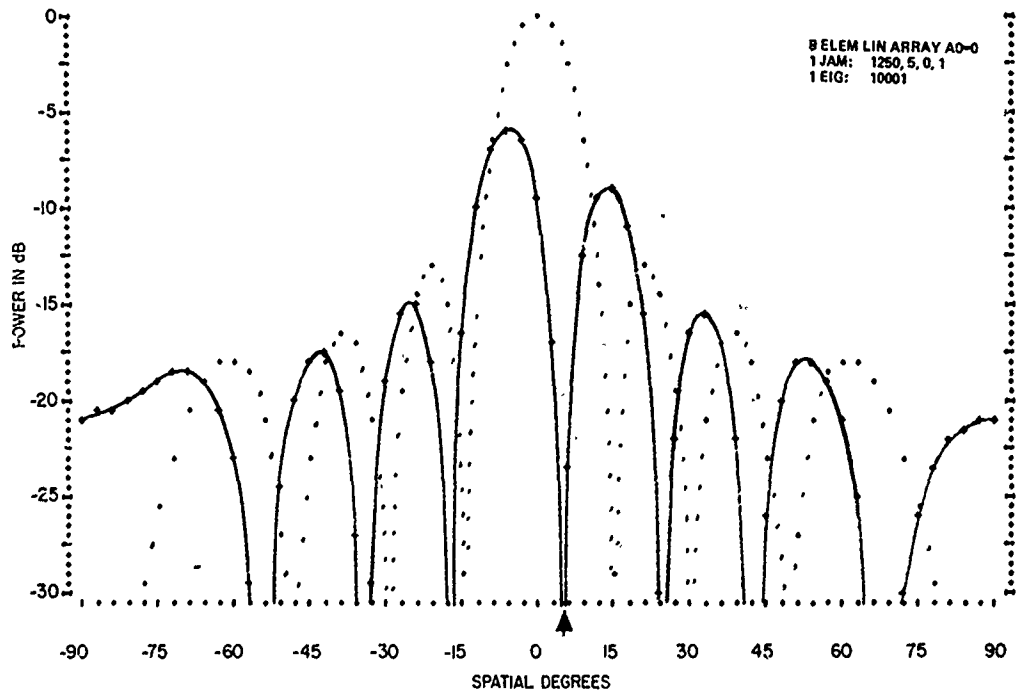

Fig. 46—Steady-state adapted pattern for single source, main-beam jammer, Case F

The transient response is shown in Fig. 47a. There are two characteristics to note, peculiar to main-beam jamming. The first is that the transient commences from a high power level for θ_1 close to θ_0, since the source gets the gain of the quiescent main beam at $t = 0$. The second is that the increase in output noise power typically drops below quiescent (0 dB) in the steady state, since the adapted weights are attenuated for θ_1 close to θ_0. The reason for the attenuation of the weights is that the unique eigenvector is closely alined with the quiescent weight vector, and this leads to small or zero magnitudes for the $\hat{W}_k$ in Eq. (4.65), which in turn results in small magnitudes for the real W_k weights. Such attenuation causes the increase in output noise power to be unsatisfactory as a performance index for main-beam jamming cases, so that it becomes desirable to consider the effect of the attenuation on the signal as well.

Signal effects may be incorporated by computing the degradation that occurs in the S/N ratio D_{sn}, formulated in Eq. (4.159). Figure 47b plots D_{sn} for this case for $\theta_s = 0°$, and we see that there is a net steady-state degradation of about 4.5 dB in output S/N ratio. Thus, although the output noise has decreased below quiescent, the output signal power drops even more and leads to a net degradation in S/N ratio for main-beam jamming.

Case G has three sources in the sidelobe region; the locations and bandwidths have been chosen to result in complete coverage of the sidelobe region from 30° to 90°. This is equivalent to spreading out 33 narrowband sources rather uniformly in sin θ spacing over this sidelobe region. Six unique eigenvalues are associated with this case. Although this case may not represent a practical interference situation, it demonstrates the remarkable effectiveness with which the adaptive array uses its degrees of freedom to cope with such widespread interference. Furthermore, it illustrates clearly that when interference sources are grouped in a continuous distribution, the eigenvector beams may be characterized by a family of harmonic pattern "modes." This case involves the first six modes of the set.

The steady-state adapted pattern is shown in Figs. 48a and 48b, which include an expanded-scale plot demonstrating the remarkably low sidelobe level achieved throughout the entire jamming region from 30° to 90°. With only seven degrees of freedom available, the array cannot respond to the 33 interference sources on an individual null basis, but it can respond on a resolution basis because of the close spacings of the sources. Thus, it depresses that entire sidelobe region by efficiently using six degrees of freedom, or six eigenvector beams.

Previous plots of the eigenvector beams have been shown in relationship to the quiescent pattern and, in fact, were adjusted in power level to the quiescent pattern via weighting factors $\hat{W}_{qi}$; i.e , the patterns plotted have been $g_i'(\theta) = \hat{W}_{qi} g_i(\theta)$. However, the eigenvector beams $g_i(\theta)$ are determined only by the covariance matrix and are completely independent of the quiescent pattern. Furthermore, these beams are characterized by certain shapes or modes that constitute a sort of harmonically related family. To stress the above two points and also to bring out the role of the $\hat{W}_{qi}$ weighting, the eigenvector beams for this case are plotted as $g_i(\theta)$ directly and the $\hat{W}_{qi}$ magnitudes are listed separately in the following tabulation, as associated with the six unique eigenvalues.

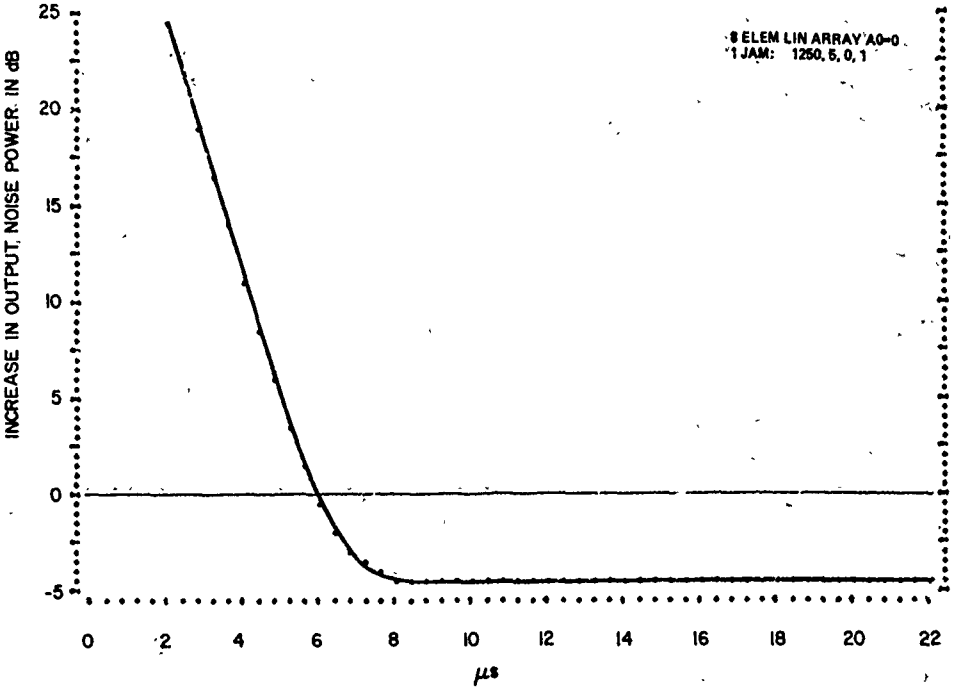

(a) Increase in output noise power

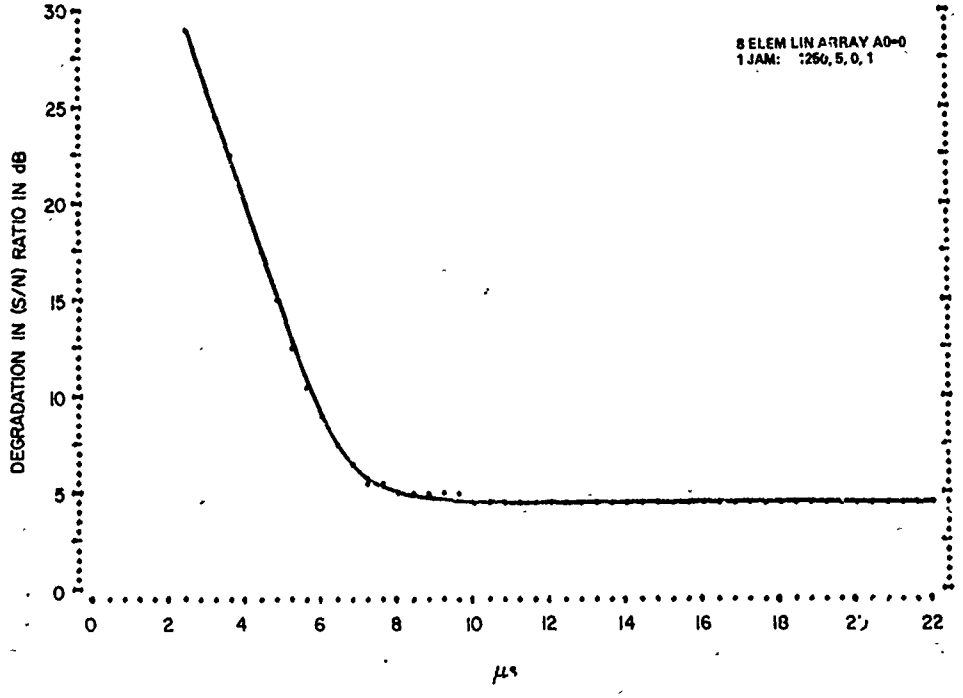

(b) Degradation in S/N ratio

Fig. 47—Transient response for single source, main-beam jammer, Case F

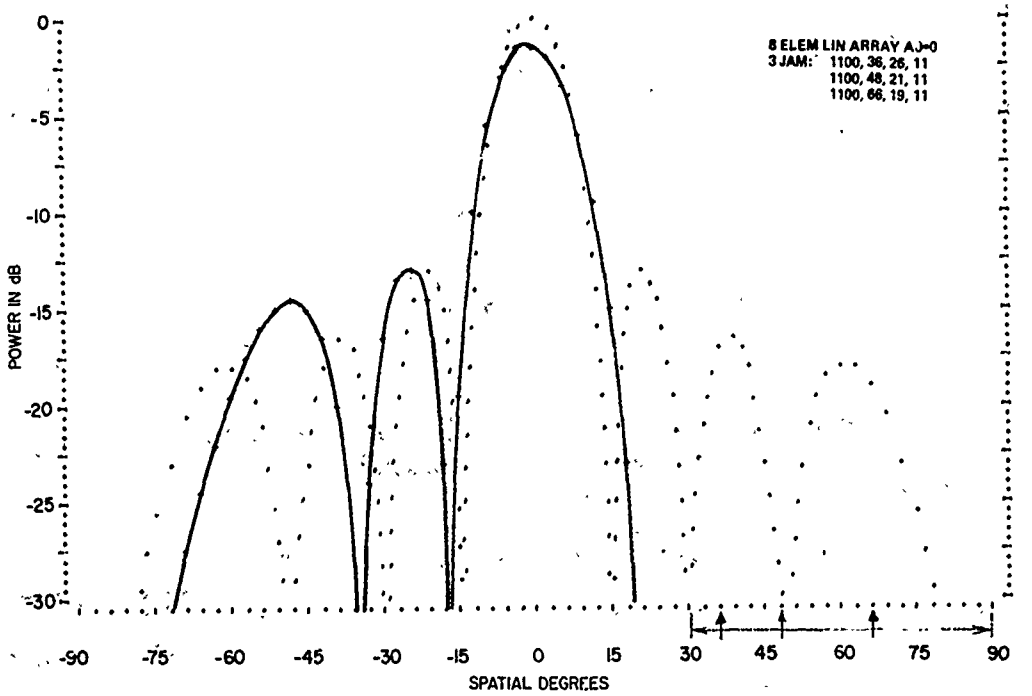

(a) Normal scale plot

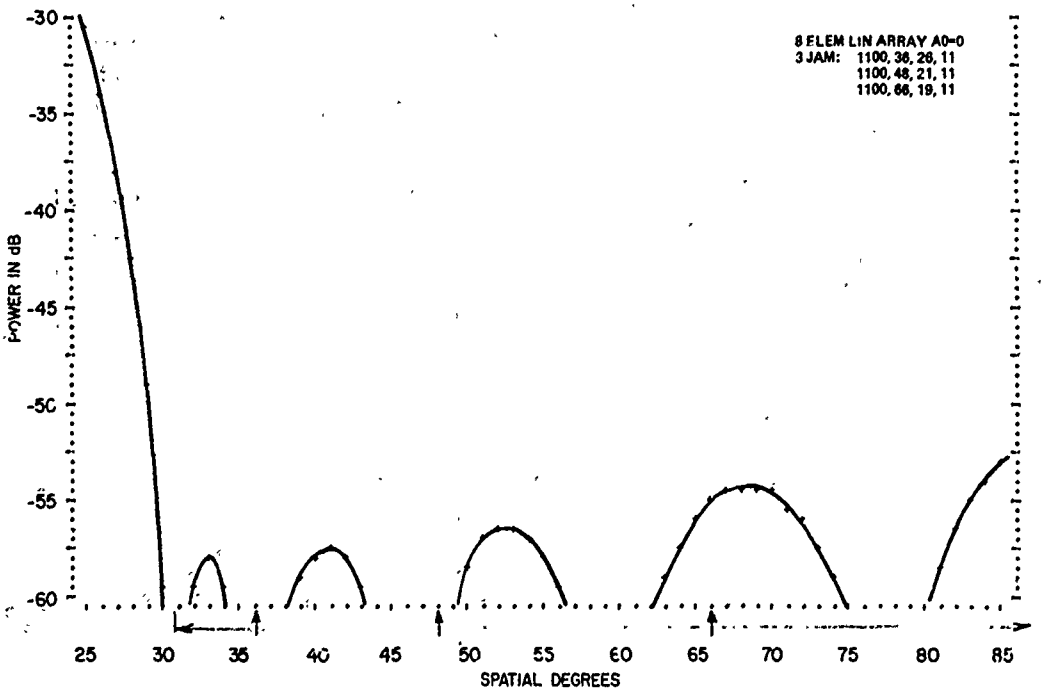

(b) Expanded sidelobe plot in source region

Fig. 48—Steady-state adapted pattern for continuous distribution sources, Case G

Unique Eigenvalue	Eigenvector Beam	$\lvert\hat{W}_{qi}\rvert$ Weighting
13,316	$g_1(\theta)$	0.083
9,692	$g_2(\theta)$	0.416
3,091	$g_3(\theta)$	0.07
296	$g_4(\theta)$	1.03
10.5	$g_5(\theta)$	0.64
1.16	$g_6(\theta)$	1.04

The six eigenvector beams are plotted in Figs. 49a – 49c, and their mode characteristics and $\hat{W}_{qi}$ weight relationship will be briefly discussed. Also, their role in the transient response shown in Fig. 50 will be pointed out.

Beam $g_1(\theta)$ is the sum beam mode with no nulls inside the source region. This beam sums all 33 sources with appreciable gain, thus resulting in the largest eigenvalue, and has the fastest transient response. However, note that the $\hat{W}_{qi}$ weighting is only 0.083, which relegates this high-power beam to a relatively minor role in determining transient response and adapted pattern.

Beam $g_2(\theta)$ is the "difference" beam mode with one null inside the source region. Except for the null region, this beam also sums the sources with appreciable gain and results in the second largest eigenvalue and the second fastest transient response. The $\hat{W}_{qi}$ weighting is 0.416, which means that this high-power beam has considerable effect upon both the transient response and adapted pattern. It accounts for most of the initial fast drop in the transient response.

Beam $g_3(\theta)$ is a "single lobe in notch" type with two nulls in the source region. This beam is obviously of lower gain than the first two and results in the third largest eigenvalue of 3,091. Note the approximate alinement of this beam with the first two. Its $\hat{W}_{q3}$ weighting of only 0.07 drops it into a minor role, even though it carries appreciable power. It is interesting at this point to look at the adapted pattern at time $t = 8$ μs, shown in Fig. 51a, which incorporates the contributions of $g_1(\theta)$, $g_2(\theta)$, and $g_3(\theta)$. Note that these first three eigenvector beams have already reduced the sidelobe level to –30 dB for most of the source region.

Beam $g_4(\theta)$ is a "double lobe in notch" type with three nulls in the source region. This beam is of low gain in the source region and results in the modest eigenvalue of 296. However, note that the $\hat{W}_{q4}$ weighting is a strong 1.03, which essentially places this beam in control of the transient response after the initial fast drop caused by $g_2(\theta)$. The slow decay so evident in Fig. 50 is dominated by this one beam. It also carried the adapted pattern quite far along toward its steady state, as shown in Fig. 51b for time $t = 120$ μs, which incorporates the contributions of the first four eigenvector beams.

Beam $g_5(\theta)$ is a "triple lobe in notch" type with four nulls in the source region. As shown in Fig. 49c, this beam is of very low gain in the source region and results in the small eigenvalue of 10.5. It does have a strong $\hat{W}_{q5}$ weighting factor of 0.64, however,

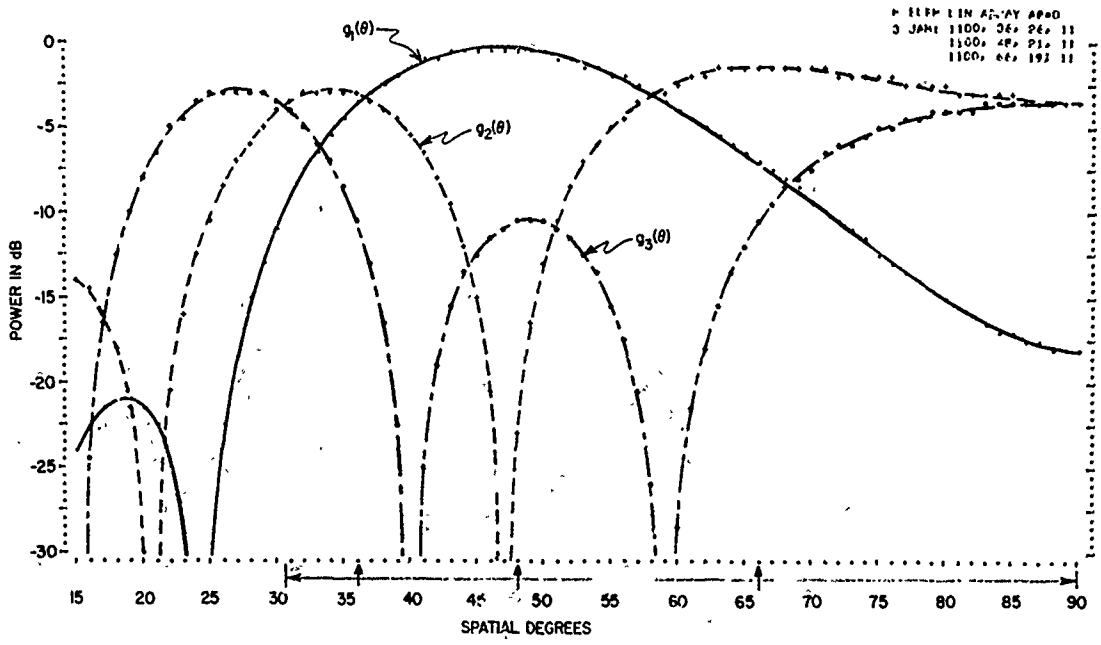

(a) Beams $g_1(\theta)$, $g_2(\theta)$, and $g_3(\theta)$

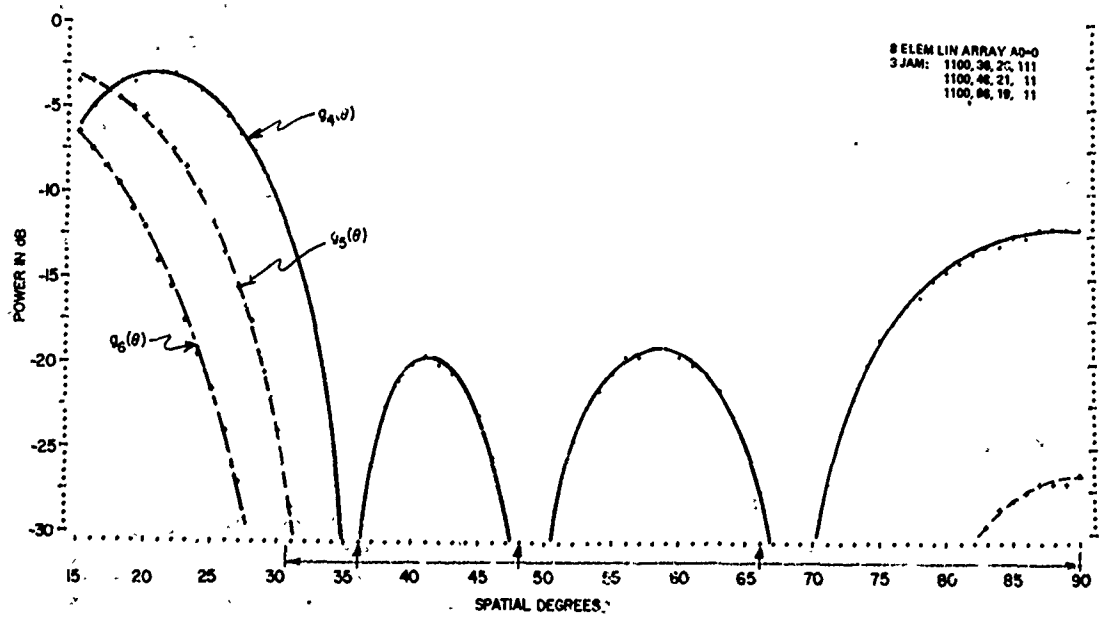

(b) Beams $g_4(\theta)$, $g_5(\theta)$, and $g_6(\theta)$

Fig. 49—Retrodirective eigenvector beams for continuous distribution sources, Case G

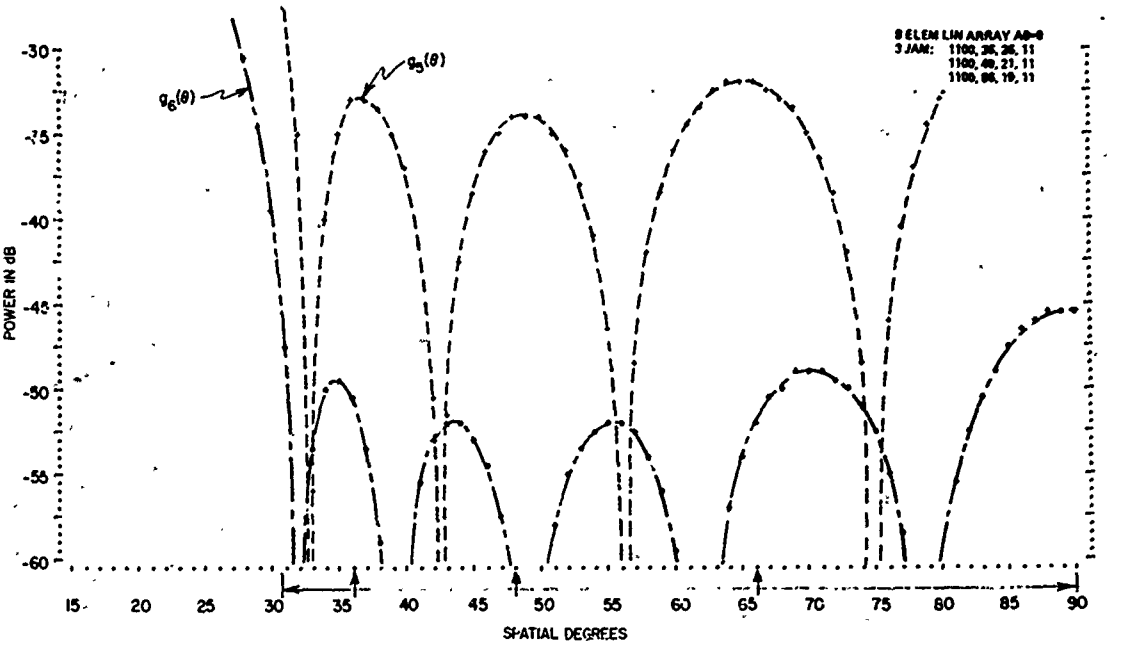

(c) Beams $g_5(\theta)$ and $g_6(\theta)$

Fig. 49 (Continued)—Retrodirective eigenvector beams for continuous distribution sources, Case G

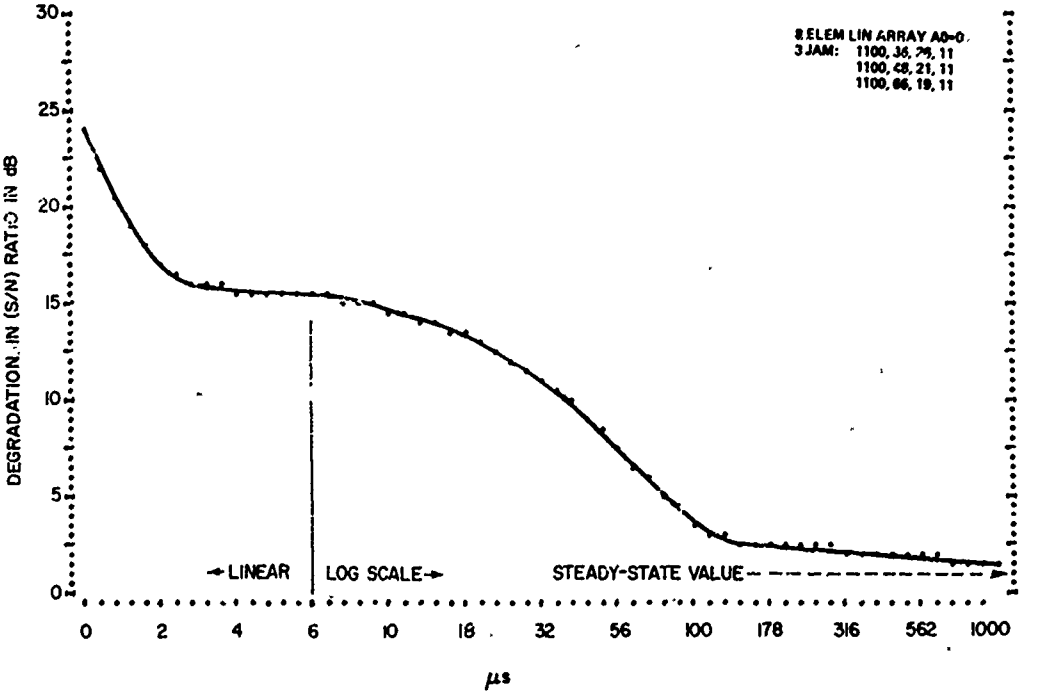

Fig. 50—Transient response for continuous-distribution sources, Case G

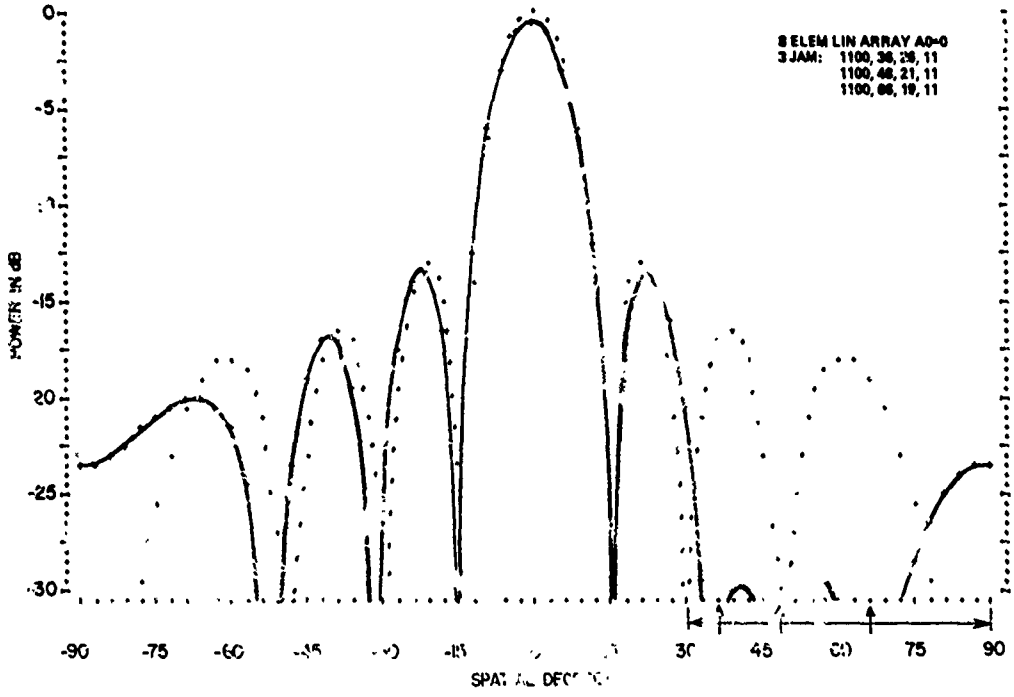

(c) $t \approx 8\ \mu s$

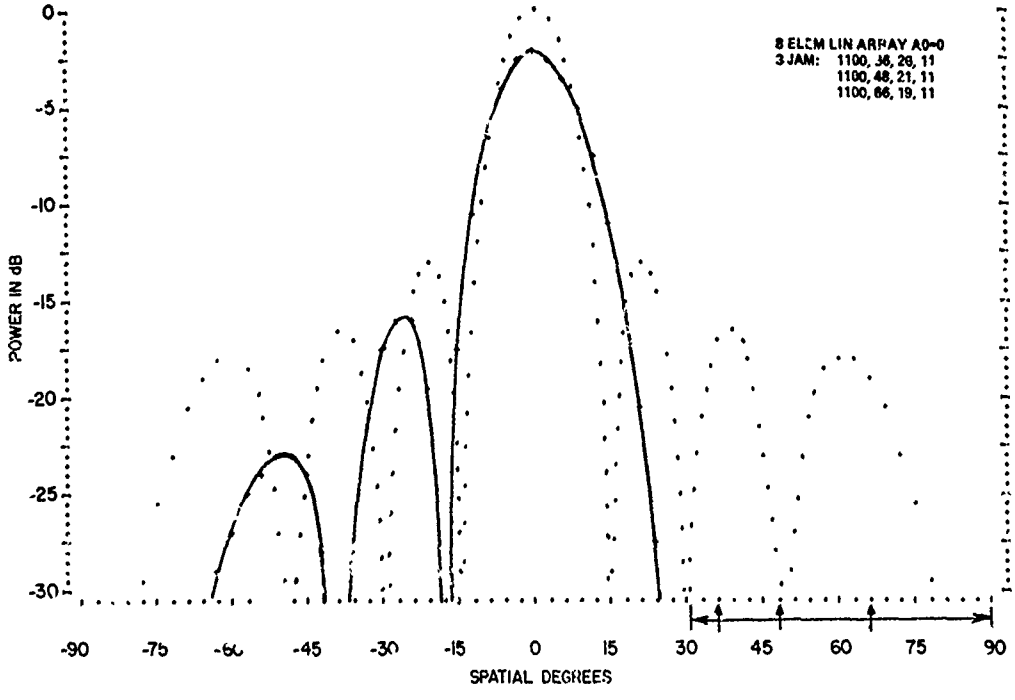

(b) $t = 120\ \mu s$

Fig. 51—Adaptive patterns at two different times for continuous-distribution sources, Case G

which gives it appreciable influence in the low sidelobe region, so that it causes the adapted pattern to slowly converge very close to steady state. It requires some 3000 μs for its transient response.

Beam $g_6(\theta)$ is a "four lobes in notch" type with five nulls in the source region. As shown in Fig. 49c, this beam is of extremely low gain in the source region and results in an eigenvalue of 1.16, barely above quiescent noise level. This small eigenvalue causes the servo gain term in Eq. (4.119) to have a value of only 0.075 and results in an almost negligible contribution from the beam, even though its $\hat{W}_{q6}$ weighting factor is a strong 1.04. For all practical purposes, this sixth eigenvector beam could be dispensed with, which means that the array is essentially devoting only five degrees of freedom to coping with the widespread interference.

Case H has six sources in the sidelobe region, in which the locations and bandwidths have been chosen to result in complete coverage of the sidelobe region from 30° to 90° on each side. It is essentially an application of the previous case's source distribution to both sides, to demonstrate how the array can take advantage of symmetry in the source distribution to better use its limited degrees of freedom in coping with a jamming situation which occupies 60% of its spatial coverage. All seven degrees of freedom are consumed.

The steady-state adapted pattern is shown in Figs. 52a and 52b, which include an expanded-scale plot, again demonstrating the remarkably low sidelobe level achieved throughout the entire jamming region from 30° to 90° on both sides (the patterns are symmetrical for this case). As in the previous case, the adaptive array is responding to the widespread jamming by depressing the entire sidelobe region. The transient response for this case is shown in Fig. 53.

A complete set of eight unique eigenvalues is associated with this case. They are listed below, together with the eigenvector beam identifications and the W_{qi} weighting magnitudes.

Unique Eigenvalues	Eigenvector Beam	$\lvert W_{qi}\rvert$ Weighting
13,532	$g_1(\theta)$	$7{\cdot}10^{-14}$
13,386	$g_2(\theta)$	0.024
12,619	$g_3(\theta)$	$8{\cdot}10^{-14}$
9,682	$g_4(\theta)$	0.60
3,224	$g_5(\theta)$	$2{\cdot}10^{-14}$
350	$g_6(\theta)$	1.42
14.7	$g_7(\theta)$	$3{\cdot}10^{-12}$
1.18	$g_8(\theta)$	2.37

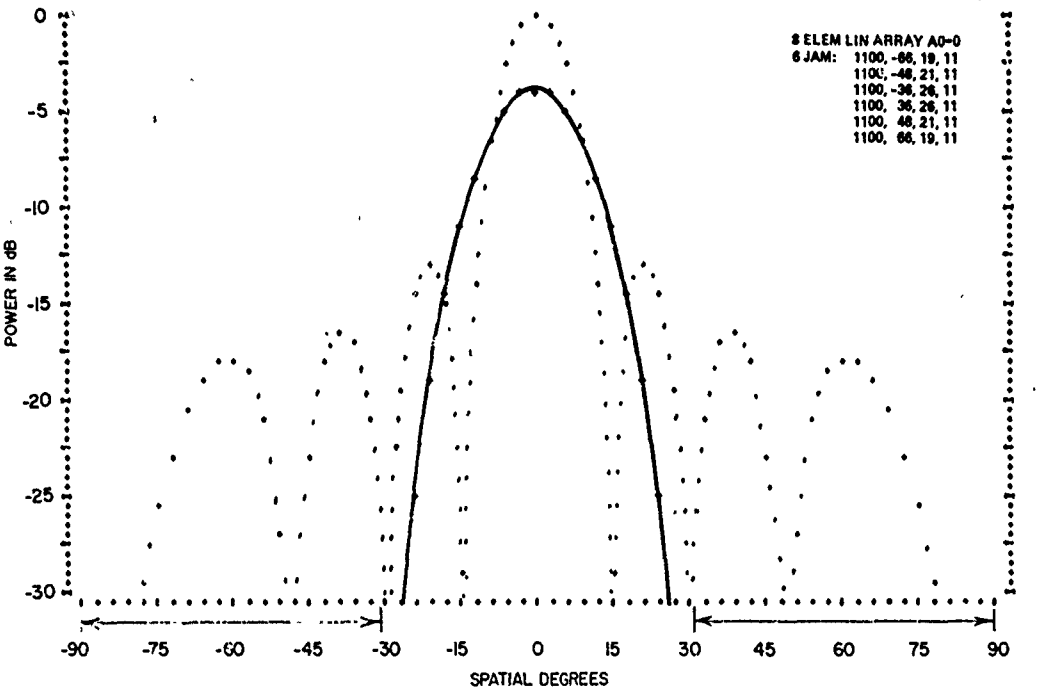

(a) Normal scale plot

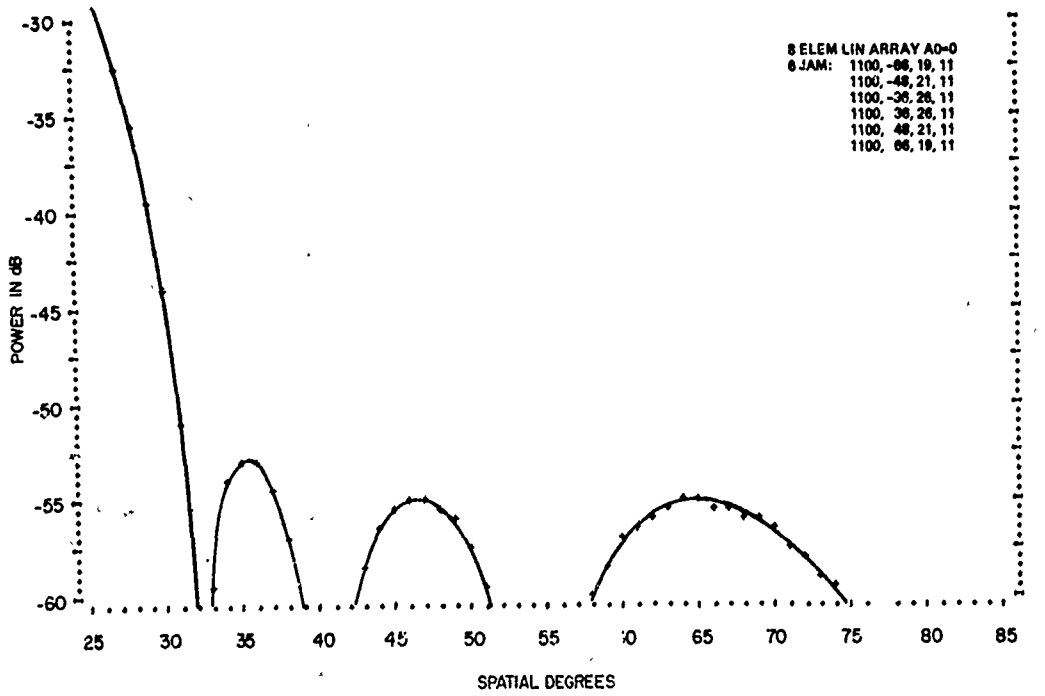

(b) Expanded sidelobe plot in source region

Fig. 52—Steady-state adapted pattern for continuous-distribution sources, Case H

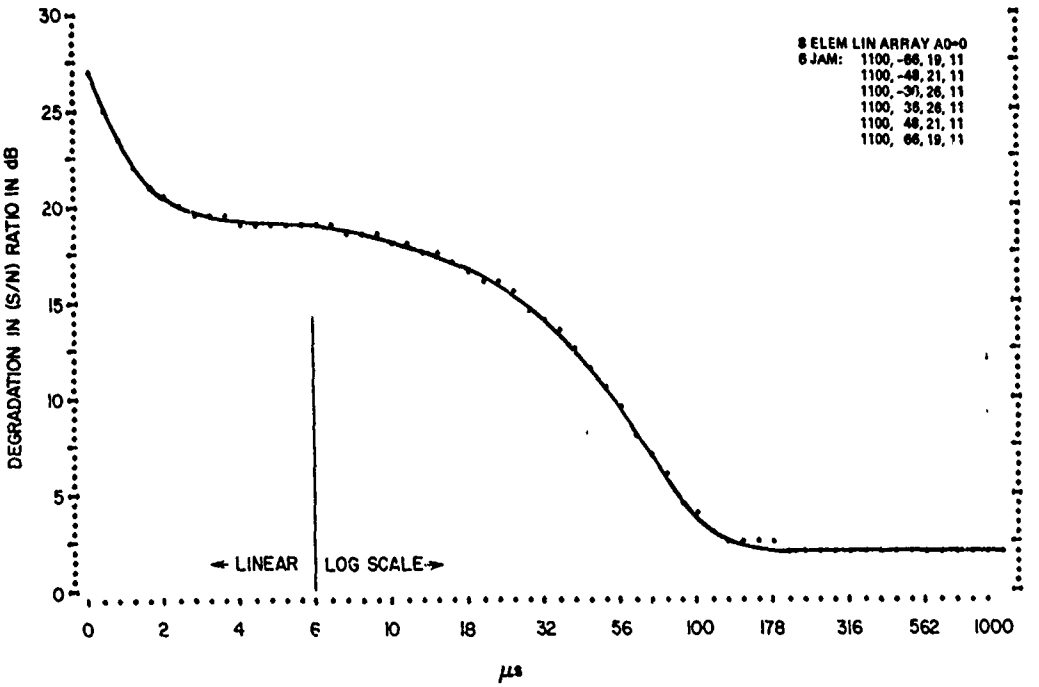

Fig. 53—Transient response for continuous-distribution sources, Case H

Note the severe attenuation in four of the $\hat{W}_{qi}$ weighting factors, which completely eliminates any contribution from those beams. Nonetheless, all eight eigenvector beams are shown in Figs. 54a and 54b and will be briefly discussed because of their departure from the usual harmonic-mode series which have characterized all of the previous cases. The reason for the departure is that the interference sources are not grouped in one continuous distribution, but are split into two distributions.

Beams $g_1(\theta)$, $g_2(\theta)$, $g_3(\theta)$ are of the sum mode type, each having appreciable major-lobe gain in the source regions, thus resulting in large eigenvalues. However, note that the $\hat{W}_{qi}$ weighting factors are so small that these high-power beams are eliminated from the transient response.

Beam $g_4(\theta)$ is of the difference mode type, with appreciable gain in the source regions to result in a large eigenvalue of 9,682. The $\hat{W}_{qi}$ weighting is also strong, 0.60, so that this beam alone controls the initial fast drop in the transient response of Fig. 53. The effect of this single beam on the adapted pattern is shown in Fig. 55, which is plotted at time $t = 8$ μs, and it is seen that sidelobes are already reduced to a level of about –28 dB by this time.

Beam $g_5(\theta)$ is of the "double lobe in notch" type, with modest gain in the source regions resulting in an eigenvalue of 3,223. Like the first three beams, its weighting factor is so small as to eliminate it from the transient response.

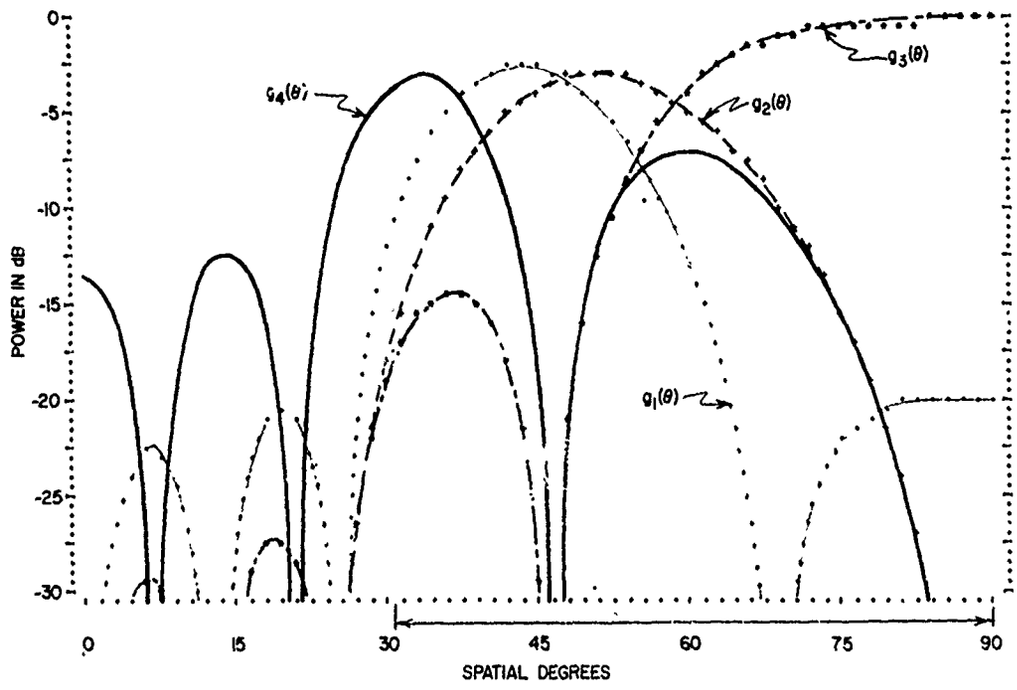

(a) Beams $g_1(\theta)$, $g_2(\theta)$, $g_3(\theta)$, and $g_4(\theta)$

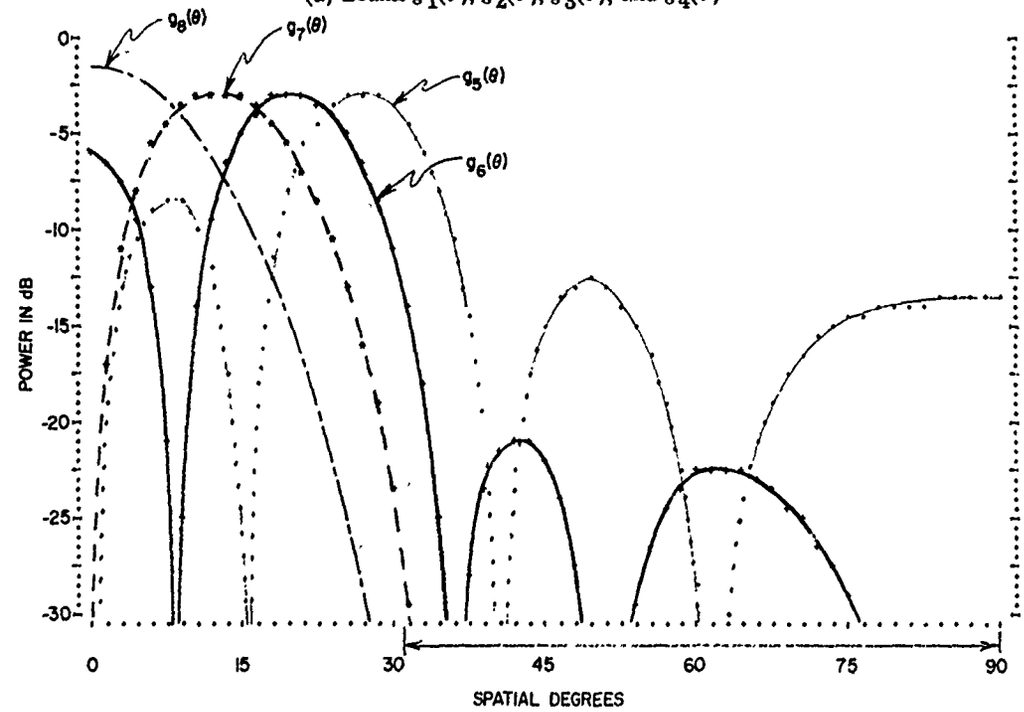

(b) Beams $g_5(\theta)$, $g_6(\theta)$, $g_7(\theta)$, and $g_8(\theta)$

Fig. 54—Retrodirective eigenvector beams for continuous-distribution sources, Case H

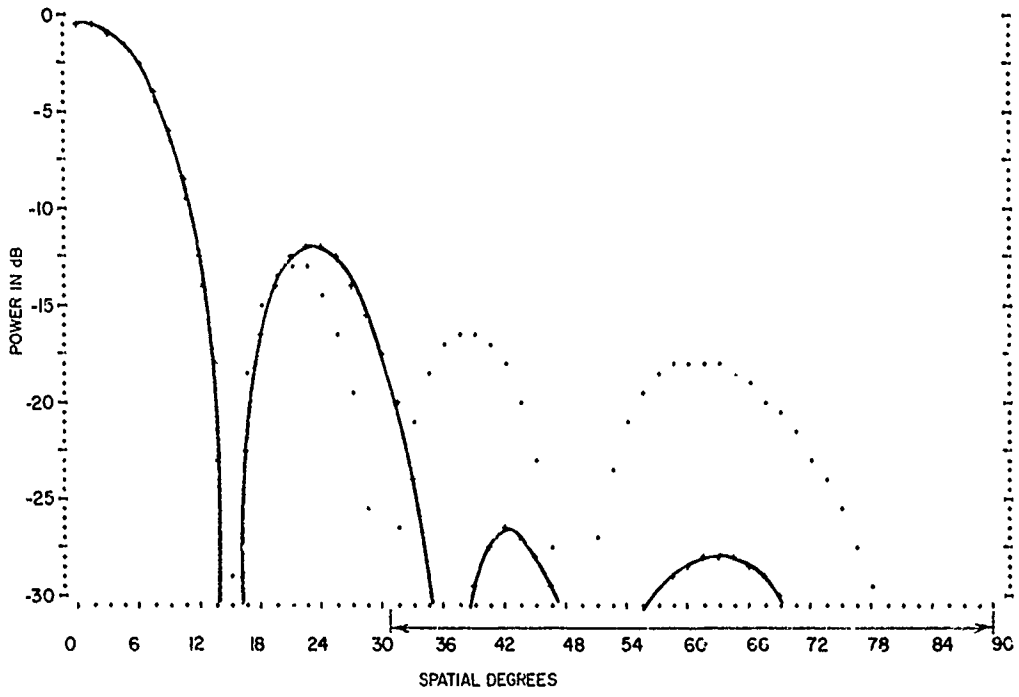

Fig. 55—Adaptive pattern at t = 8 μs for continuous-distribution sources, Case H

Beam $g_6(\theta)$ is of the "double lobe in notch" type, with low gain in the source regions resulting in a modest eigenvalue of 350. However, its weighting factor is a strong 1.42, which places this beam in complete control of the transient response after the initial fast drop due to $g_4(\theta)$. The slow decay noted in Fig. 53 is caused entirely by this one beam, and after its decay time of approximately 120 μs the adapted pattern will be virtually at its steady-state condition.

Beam $g_7(\theta)$ is of the "triple lobe in notch" type with very low gain in the source regions, resulting in the small eigenvalue of 14.7. Its weighting factor is very small, so it plays no part in the transient response.

Beam $g_8(\theta)$ is another "triple lobe in notch" type with an extremely low gain in the source regions, resulting in an eigenvalue of 1.18, barely above quiescent noise level. Because this eigenvalue is so close to unity, the servo gain term in Eq. (4.119) will have a value of only 0.083, resulting in almost negligible contribution to the transient, even though its weighting factor is a strong 2.37.

Although this beam does not contribute to the adapted pattern as expressed by Eq. (4.119), the reader should consider the fact that for this case the interference source distribution has consumed all seven available degrees of freedom, and jammer power is being delivered by all of the eigenvector beams except $g_8(\theta)$. If one observes the $\hat{W}_{qi}$ weighting for each beam and applies Eq. (4.65) for the $\hat{W}_k$ orthonormal weights, $g_8(\theta)$ will be the only beam capable of delivering signal power to the output of the orthonormal system,

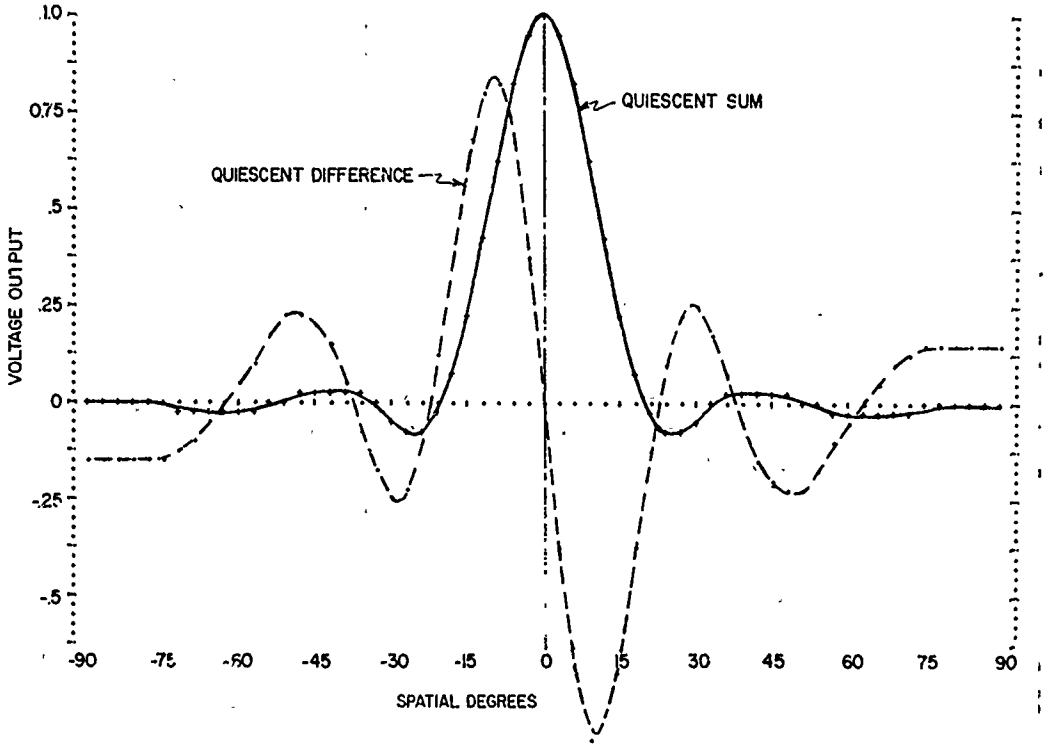

Fig. 56—Quiescent sum and difference tracking patterns

and therefore it must be identical to the steady-state adapted pattern shown in Fig. 52; i.e., for this case, $G(\theta, \infty) \approx \hat{W}_{q8} g_8(\theta)$.

Adaptive Tracking Patterns—It is of interest to see what happens to typical tracking patterns when both the sum and the difference pattern are instrumented to adapt to an interference environment. For the quiescent patterns, tapered sum and difference illuminations were chosen as follows:

Weight	Sum	Difference
W_{q1}	0.3	0.982
W_{q2}	0.604	0.847
W_{q3}	0.847	0.603
W_{q4}	0.982	0.3
W_{q5}	0.982	−0.3
W_{q6}	0.847	−0.603
W_{q7}	0.604	−0.847
W_{q8}	0.3	−0.982

These illuminations result in the quiescent patterns shown in Fig. 56, which are plotted on a linear voltage scale to emphasize the slope and crossover associated with the difference pattern.

From Table 2, Case D was chosen as an appropriate sidelobe interference distribution. It includes four narrowband sources of unequal power ratios and moderate spacing and results in the four unique eigenvalues 11,616, 2,486, 406, and 17. Its associated eigenvector beams were as shown in Fig. 40.

A time sequence for the adapting patterns is shown in Figs. 57a – 57d for times t = 12, 120, and 1,200 μs, and for the steady state. At time t = 12 μs, the sidelobe structure has changed considerably on the right-hand side, but the main-beam crossover region has not yet been affected much. This time would incorporate the effects of the first two eigenvector beams $g_1(\theta)$ and $g_2(\theta)$.

At time t = 120 μs, which would incorporate the effect of the third eigenvector beam $g_3(\theta)$, note that the negative half of the difference pattern is collapsing. This collapse changes both the crossover point and the slope at crossover. In addition, the sum pattern is distorted and shifted to the left.

At time t = 1,200 μs, which incorporates the effects of all four eigenvector beams, the collapse of the difference pattern is almost complete, the crossover point is 4° off, and the slope has changed considerably.

At steady-state adapted conditions, the distortion of the difference pattern is so severe as to render it useless.

This example illustrates that tracking patterns may undergo severe deterioration when they are made adaptive to sidelobe interference. One method for coping with this serious problem is to incorporate constraints on the patterns in their crossover region by sacrificing array degrees of freedom. For example, one might sacrifice a degree of freedom in order to force the difference pattern to always maintain a fixed crossover position regardless of sidelobe adaptation.

4.6. Hard-Limiter Modification

The dynamic range and transient response time of the configuration in Fig. 24 can be improved by incorporating a hard limiter or fast AGC (automatic gain control) in the conjugate signal branches, in the same manner as described in Sec. 3.4 for the single adaptive servo loop. The modified circuit schematic is shown in Fig. 58. Note that each servo loop is arranged in exactly the same manner as the single loop of Fig. 20. Reference 32 is recommended for a more rigorous mathematical development of the effects of envelope limiting in adaptive-array control loops.

The modification changes the output voltages from the correlation mixers, in that the amplitude variations in the conjugate signals are removed and only the phase variations are retained; i.e., Eq. (4.15) becomes

$$x_k' = k^2 h\left(\overline{\frac{E_k^*}{|E_k|}\sum_{i=1}^{K} W_i E_i}\right), \tag{4.171}$$

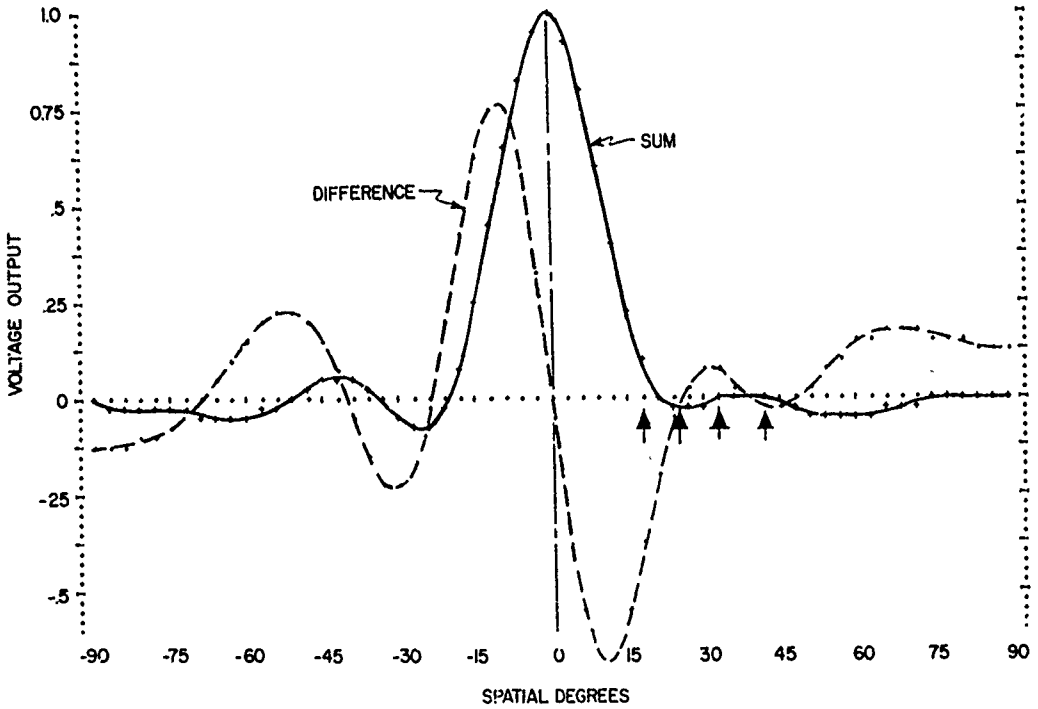

(a) t = 12 μs

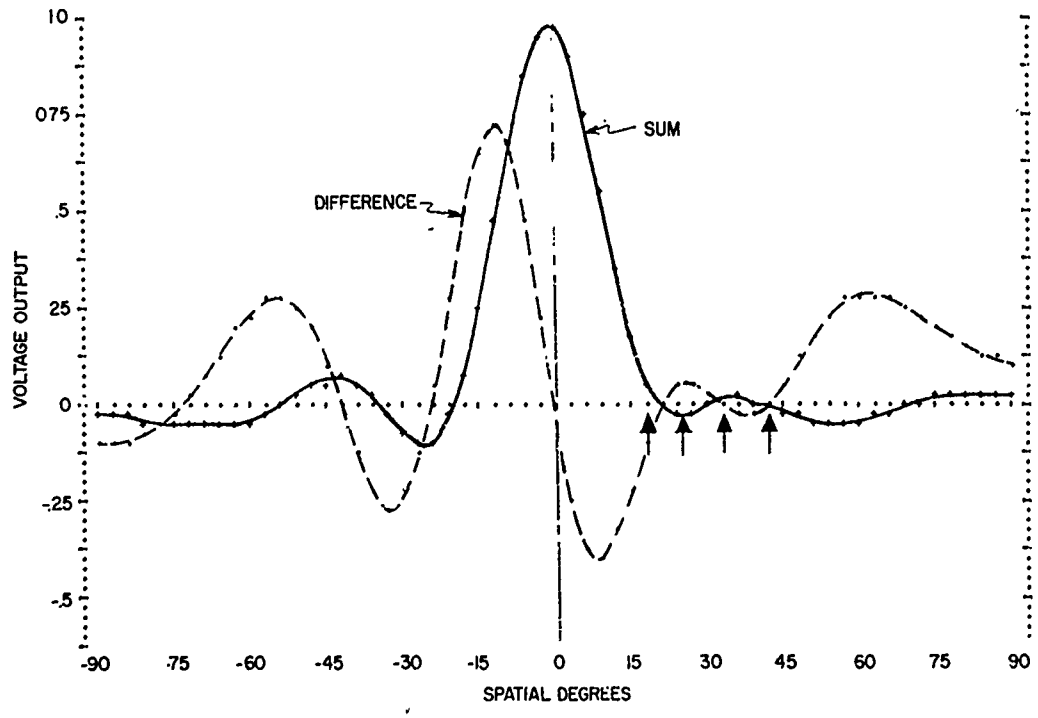

(b) t = 120 μs

Fig. 57—Adaptive sum and difference patterns during transient for four sources, Case D

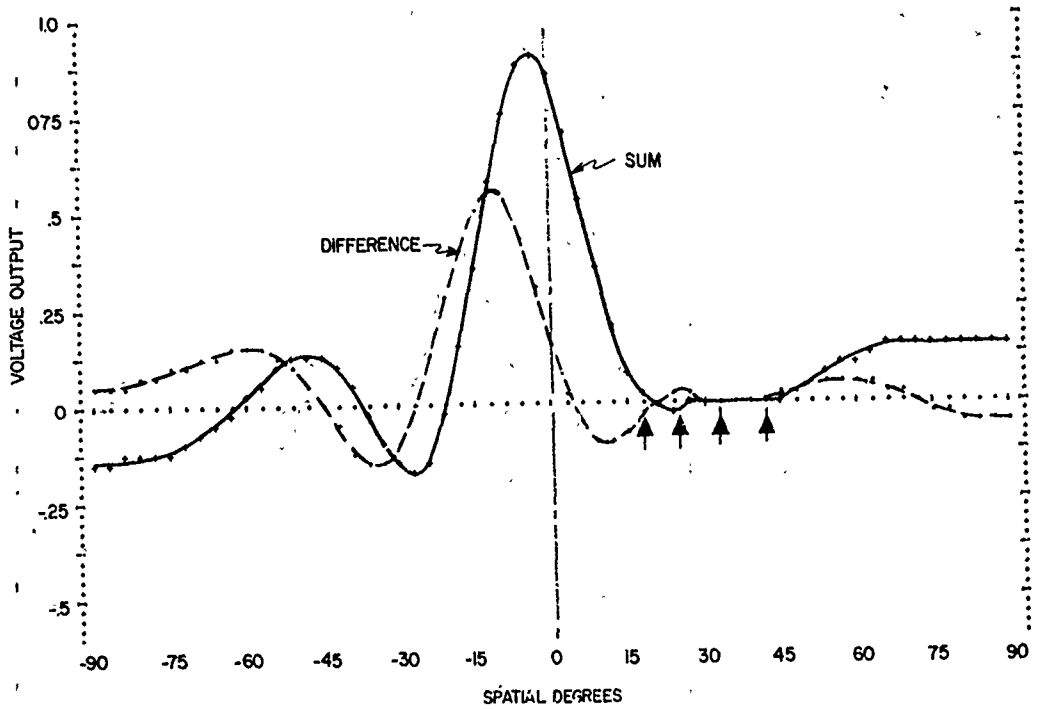

(c) t = 1,200 μs

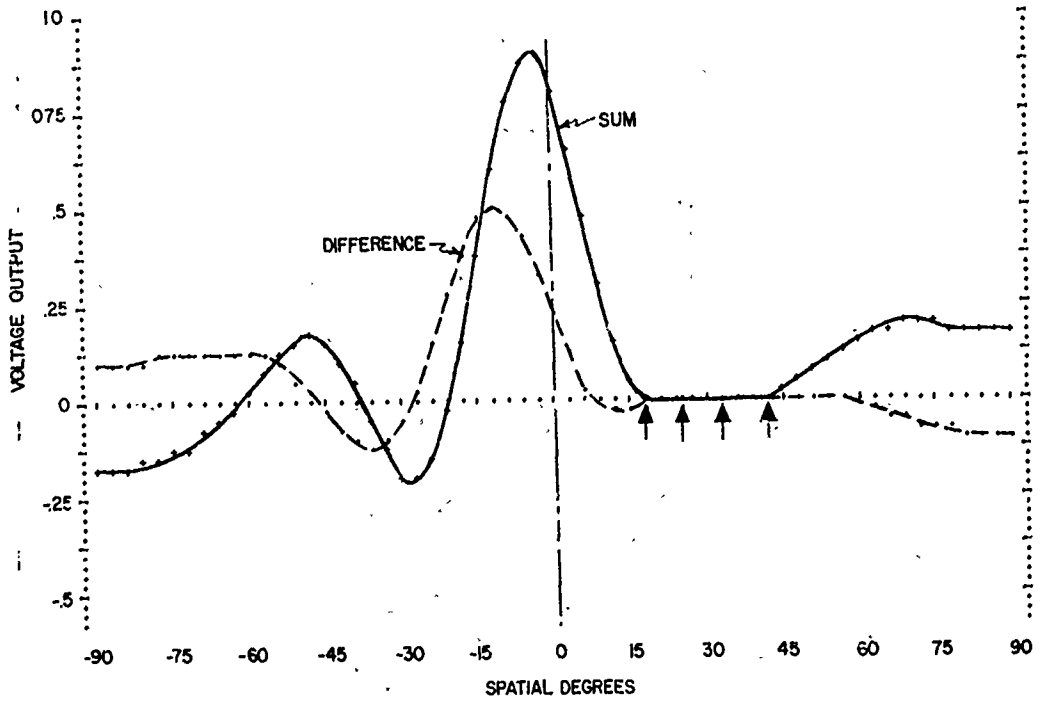

(d) Steady-state adapted

Fig. 57 (Continued)—Adaptive sum and difference patterns during transient for four sources, Case D

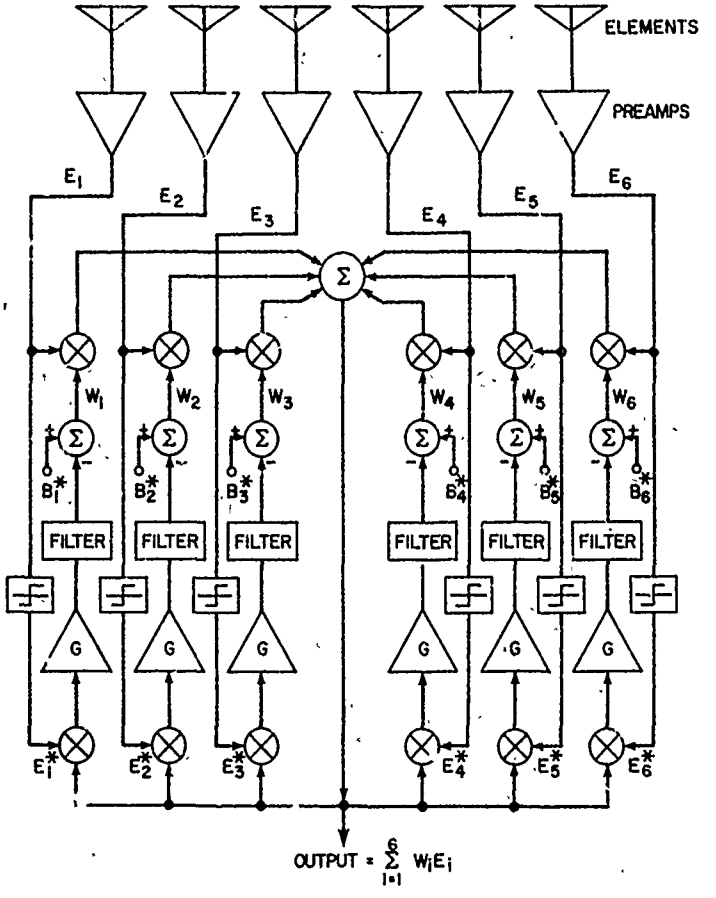

Fig. 58—Hard-limiter modification of linear adaptive array configuration

where h is an amplitude constant associated with the limiter arrangement, assumed to be equal for all channels. From Eq. (4.25) the $|\bar{E}_k|$ are given by

$$|\bar{E}_k| = \sqrt{|\bar{n}_0|^2 + \sum_{i=1}^{I} |\bar{J}_i|^2}\,; \tag{4.172}$$

i.e., the rms voltage magnitudes are to be equal for all channels. Under these assumptions, one finds that the elements of the new covariance matrix differ from the elements of M only by a common factor. This leads to the following equation, equivalent to Eq. (4.29):

$$\tau_0 \frac{d\mathbf{W}}{dt} + \left[\mathbf{I} + \left(\frac{\gamma'}{|\bar{E}_k|}\right)\mathbf{M}\right]\mathbf{W} = \mathbf{B}^* \tag{4.173}$$

where $\gamma' = k^2 h G'$. Operating upon Eq. (4.173) with the Q-matrix transformation as in Eqs. (4.54) through (4.57) results in

$$\tau_0 \frac{d\hat{\mathbf{W}}}{dt} + \left[\left(1 + \frac{\gamma'\beta_i^2}{|\bar{E}_k|}\right)\delta_{ij}\right]\hat{\mathbf{W}} = \hat{\mathbf{B}}^*. \tag{4.174}$$

Recall the equivalent orthonormal adaptive array system of Fig. 25 and note that Eq. (4.174) would be tantamount to defining a new input signal vector $\mathbf{E}'$ for that system, whereby

$$\mathbf{E}' = \sqrt{\frac{1}{|\bar{E}_k|}}\,\mathbf{E}; \tag{4.175}$$

i.e., the square root of a limiting operation is applied uniformly to all element signals before entering the Q-matrix transformation network, and there is no limiting in the orthonormal servo loops themselves.

Corresponding to Eq. (4.45) we have a new equivalent servo gain factor from Eq. (4.174),

$$\mu_i' = \left(\frac{\gamma'\beta_i^2}{|\bar{E}_k|}\right). \tag{4.176}$$

This is the important result of the limiter modification, because we are now back to the form of Eq. (4.47) and can use the solutions thereof if μ_i is replaced by μ_i'. From Eq. (4.176) define a quiescent servo gain factor μ_0' as in Eq. (4.60),

$$\mu_0' = \left(\frac{\gamma'\beta_0^2}{|\bar{n}_0|}\right) \tag{4.177}$$

where we anticipate that large values will be selected for μ_0' (via amplifier gains) for the same reasons as discussed in Sec. 3.4. From the ratio of μ_i' to μ_0', one can obtain a more convenient form for Eq. (4.176),

$$\mu_i' = \left(\frac{\mu_0'}{\sqrt{1 + \sum_{r=1}^{R} P_r}}\right)\left(\frac{\beta_i^2}{\beta_0^2}\right), \tag{4.178}$$

where P_r is the usual ratio of source power to receiver noise power. Comparing this expression against the one in Eq. (4.142), we note that the only difference is the square root of the power ratio summation in the denominator. That summation, however, produces a number of interesting effects, including the following:

1. The strong jammer power ratios will dominate the summation and result in lower values for any μ_i associated with the weak jammers.

2. For small eigenvalues, μ_i' will generally be smaller than μ_0' and can approach unity. This effect results in rather large magnitude levels for the adapted weights and requires a modification of the eigenvector beam concept equations.

3. For maximum power summations, the transient performance with limiters will be no better than without the limiters and may be worse.

4. It further complicates the maximum servo gain factor condition which relates to control-loop noise.

Equation (4.146) is now modified to the expression

$$\mu_m' = \left(\frac{\mu_0'}{\sqrt{1 + \sum_{r=1}^{R} P_r}} \right) \left(\frac{\beta_m^2}{\beta_0^2} \right) = \left(\frac{\pi B_c \tau_0}{10} \right) - 1 . \tag{3.179}$$

A little thought on the several parameters involved in this expression indicates that it will be difficult to make exact comparisons with the transient performance characteristics plotted previously. From Table 2, we see that the largest eigenvalue encountered was 18,544 in Case B, with a total power ratio of 2,450. Using these values, together with a reasonably high value of 100 for μ_0', leads to a preliminary selection for μ_m' of about 40,000. If the channel bandwidth B_c is kept at 5 Mc as before, τ_0 must be increased to 25,500 μs. Summarizing these selected constants, then, we have

$$\mu_0' = 100$$

$$\mu_m' \approx 40{,}000$$

$$\tau_0 = 25{,}500\ \mu s$$

$$B_c = 5\ \text{Mc}.$$

Before calculating transient response, it is pertinent to examine the steady-state orthonormal weight equation (Eq. (4.62)), which will now be given by

$$\hat{W}_i(\infty) = \left(\frac{1 + \mu_0'}{1 + \mu_i'} \right) \hat{W}_{qi} . \tag{4.180}$$

Note that since the value of μ_i' can be much smaller than μ_0', it is evident that the orthonormal weights can be much larger than the quiescent weights, and this can carry over into the final real weights. Therefore, the usual previous performance index of increase in output noise power cannot be used with the limiter modification. It is necessary to use the degradation in S/N ratio, defined in Eq. (4.159), instead. Based on this latter performance index, the following cases from Table 2 are compared:

Case A—The transient performance for this case of a single, narrowband interference source is greatly improved by the limiter modification, as shown in Fig. 59 for jammer power ratios of 21 and 31 dB. For such single-source cases, the system will behave in much the same manner as the single adaptive loop discussed in Sec. 3.4, because only one unique eigenvalue and one power ratio are involved. Note particularly the improvement at the lower power ratio of 21 dB.

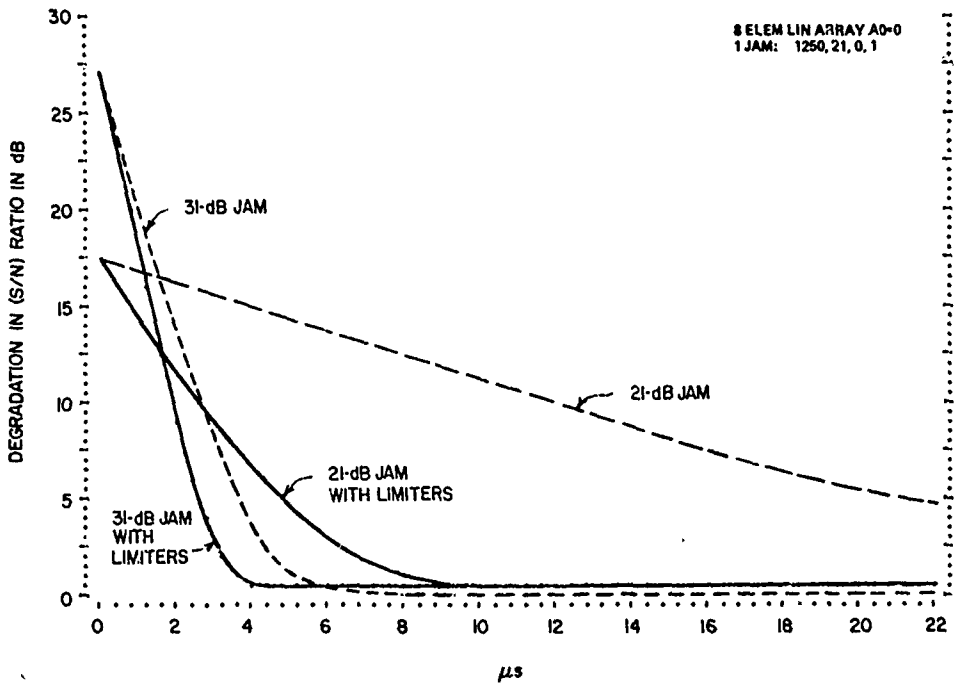

Fig. 59—Transient response with and without limiter modification for single source, Case A, for power ratios of 21 dB and 31 dB

To illustrate the increase in the adapting weights referred to above, Fig. 60 is a special plot of the increase in output noise power, in which the time scale becomes logarithmic after $t = 7.2$ μs. After the initial fast transient in which the jammer noise power is nulled, the weights increase in magnitude slowly (while keeping the jammer nulled out) until they reach the steady-state level given in Eq. (4.180). For the seven nonunique eigenvalues, $\mu_i' = 9.83$; the ratio in Eq. (4.180) is equal to 26.4, approximately representing the steady-state weight magnitudes; the square of that ratio then accounts for the 28-dB increase in output noise power. The array gain also increases by the same amount, so that the effect does not show up in the S/N plots of Fig. 59.

Case B—The transient performance for this two-source case is shown in Fig. 61. It is the same with limiters as without (compare with Fig. 36). The reason for the practically identical behavior is that this case was the basis for the choice of μ_m, τ_0, μ_m', and τ_0', and results in almost identical transient decay factors. For example, for the largest eigenvalue,

$$\alpha_m = \frac{1 + \mu_m}{\tau_0} = \frac{18{,}545}{12{,}750} = 1.455$$

$$\alpha_m' = \frac{1 + \mu_m'}{\tau_0} = \frac{37{,}458}{25{,}500} = 1.469.$$

The only major difference is that with the limiter modification, the magnitudes of the weights change in a manner similar to that described for Case A.

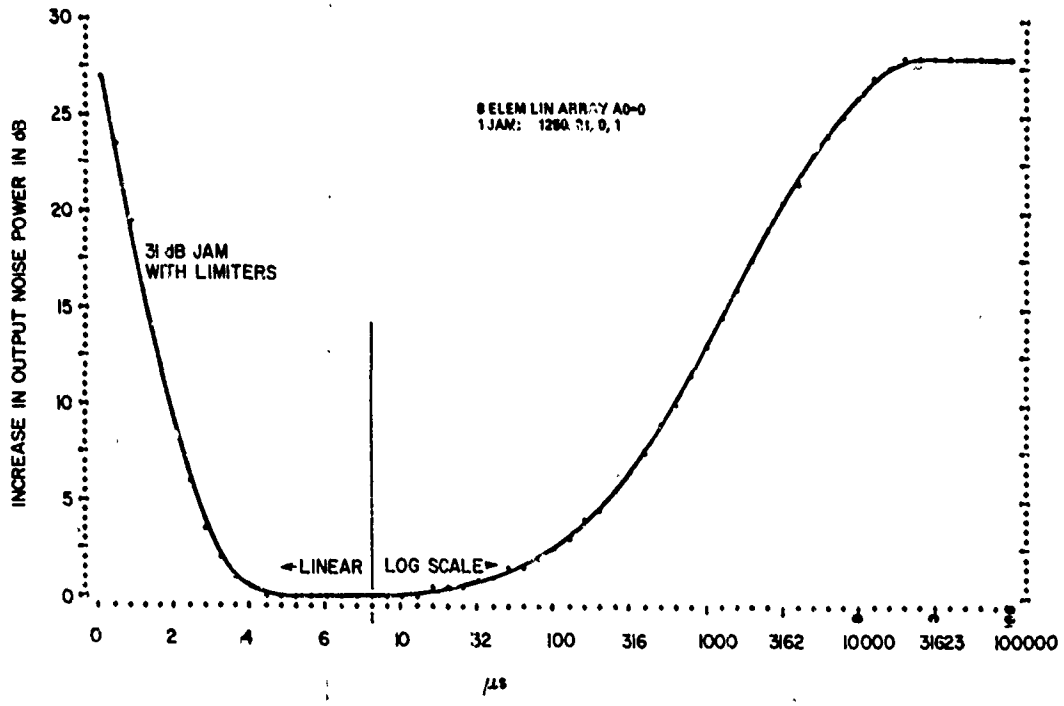

Fig. 60—Transient response for Case A in terms of output noise power, illustrating the increase in magnitude level of the weights

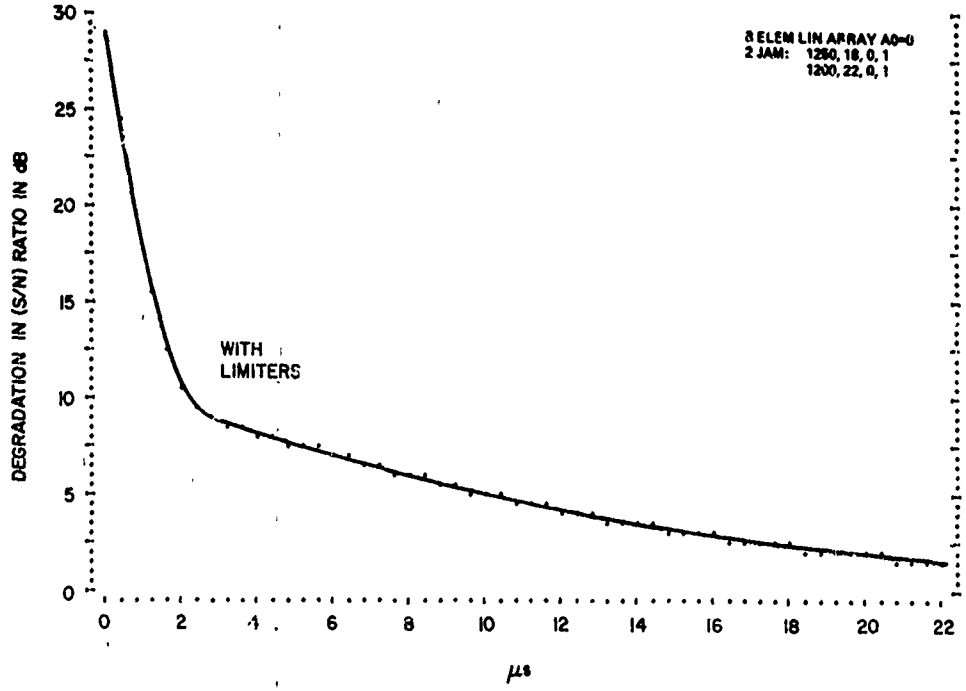

Fig. 61—Transient response with limiter modification for two sources, Case B

Case C—This two-source case is the same as Case B, except that the power ratio of the second source is reduced by 10 dB. Transient response is shown in Fig. 62 with and without limiters. Note that there is little difference, a reflection of the fact that the transient decay factors are not much different.

Case D—This four-source case has a transient response with limiters that is so nearly identical to that shown in Fig. 41 that there is no point in showing it. The transient decay factors are almost equal for the two conditions.

Case E—The single-source case with various bandwidths shows little difference with limiters. Figure 63 illustrates the transient responses for a bandwidth of 15%.

Case F—This case of main-beam jamming is little different from that shown in Fig. 47b, but it shows distinctly faster transient response with limiter modification if the power ratio were lowered by 10 dB or more, in a manner similar to Case A.

Case G—This extensive sidelobe-jamming case with limiters has a transient response nearly identical to that given in Fig. 50.

Case H—With symmetry in its extensive sidelobe jamming and twice the total power of Case G, this case shows some difference in the transient response. Note in Fig. 64 that the response is worse with limiters than without. The considerably poorer performance in the vicinity of 100 μs is partly caused by increased α_i values and partly by the effects of the slowly increasing weight magnitudes.

The steady-state adapted patterns for the above cases are not changed significantly by the limiter modification, provided that $\mu_0' \gg 1$. However, the transient pattern behavior will usually be different because of different transient decay factors α_i and a modification in the eigenvector beam summation. To bring out these differences, let us rewrite the steady-state orthonormal weights of Eq. (4.180) in the following form:

$$\hat{W}_i(\infty) = a\left(\frac{1 + \mu_{im}'}{1 + \mu_i'}\right)\hat{W}_{qi} \tag{4.181}$$

where

$$a = \left(\frac{1 + \mu_0'}{1 + \mu_{im}'}\right) \tag{4.182}$$

and

$$\mu_{im}' = \frac{\mu_0'}{\sqrt{1 + \sum_{r=1}^{R} P_r}}. \tag{4.183}$$

Under the eigenvalue condition that $\beta_i^2 = \beta_0^2$, μ_{im}' represents the minimum value of μ_i' from Eq. (4.178), and it will generally be much smaller than μ_0'. For example, in Case A

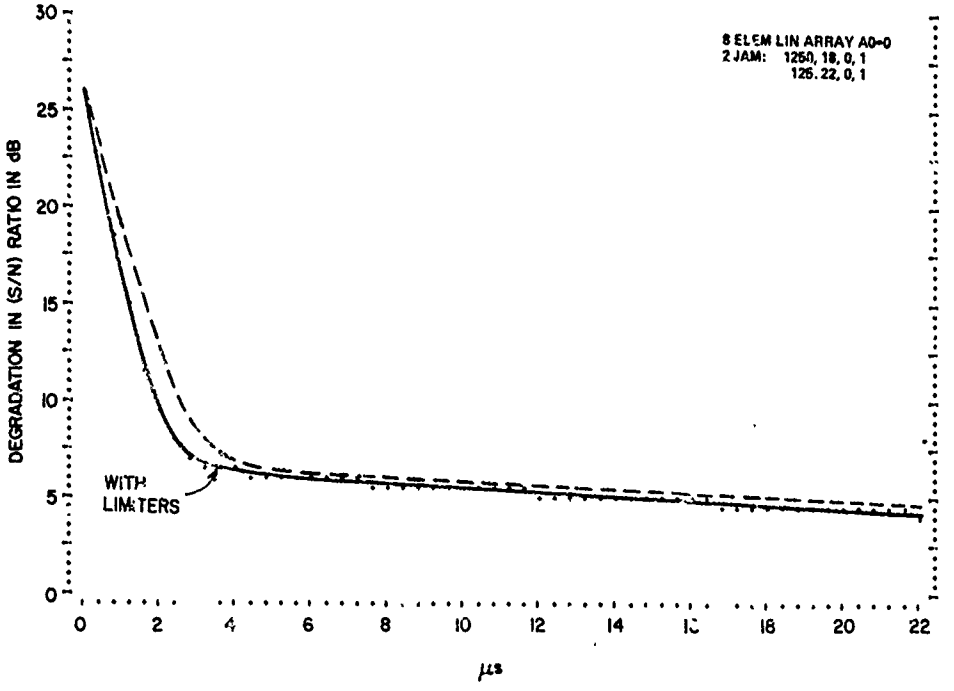

Fig. 62—Transient response with and without limiter modification for two sources, Case C

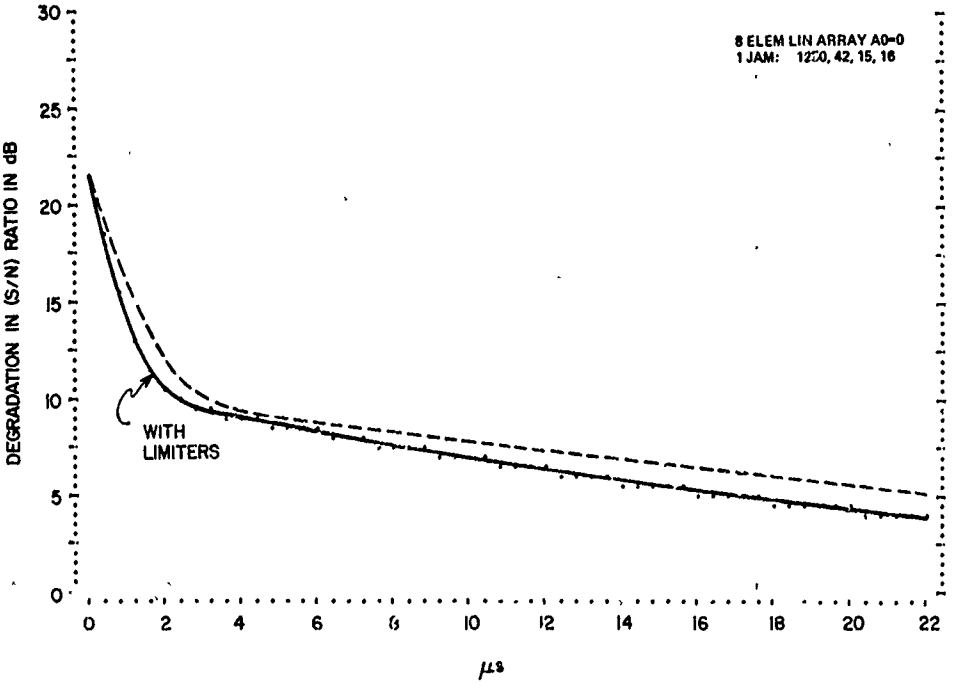

Fig. 63—Transient response with and without limiter modification for single source with 15% bandwidth, Case E3

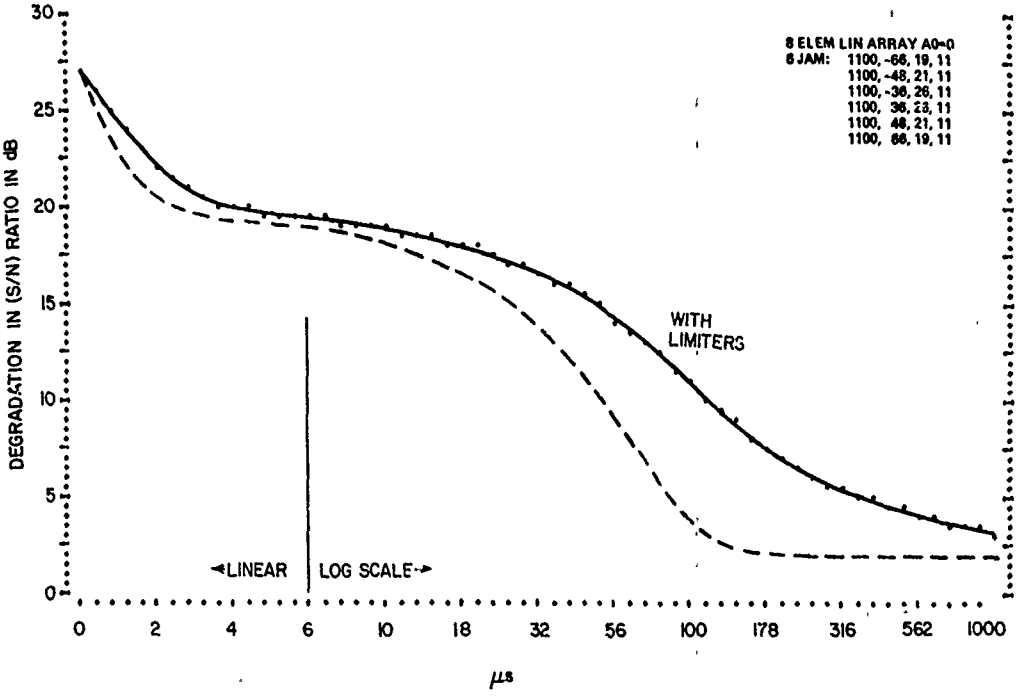

Fig. 64—Transient response with and without limiter modification for continuous-distribution sources, Case H

$\mu'_{im} = 2.83$, and this results in a value of $a = 26.4$ for the constant defined in Eq. (4.182). The constant a represents the increase in the magnitude level of the nonunique orthonormal weights.

Substituting this new expression for $\hat{W}_i(\infty)$ into Eq. (4.48), we can manipulate it into the following relationship for the orthonormal weights:

$$\hat{W}_i = a\left\{\hat{W}_{qi} - (1 - e^{-\alpha_i t})\left(\frac{\mu'_i - \mu'_{im}}{\mu'_i + 1}\right)\hat{W}_{qi} - \left(1 - \frac{1}{a}\right)e^{-\alpha_i t}\hat{W}_{qi}\right\}. \quad (4.184)$$

Compare Eq. (4.184) against Eq. (4.65), and note that the first two terms are the same if we assume that μ'_{im} plays the same roll as μ_0. However, we have an extra transient term on the right-hand side in the above expression.

Proceeding with the same arguments used in developing Eq. (4.119) results in the following output pattern function, from Eq. (4.184):

$$G(\theta, t) = a\left\{G_q(\theta) - \sum_{i=1}^{K}(1 - e^{-\alpha_i t})\left(\frac{\mu'_i - \mu'_{im}}{\mu'_i + 1}\right)\hat{W}_{qi}g_i(\theta) - g'(\theta, t)\right\} \quad (4.185)$$

where

$$g'(\theta,t) = \left(1 - \frac{1}{a}\right) \sum_{i=1}^{K} e^{-\alpha_i t} \hat{W}_{qi} g_i(\theta). \tag{4.186}$$

Compare Eq. (4.185) against Eq. (4.119), and note that except for $g'(\theta,t)$ the expression is similar if we assume equivalence of μ'_{im} and μ_0, and that under steady-state conditions the results should be virtually identical. This explains why the steady-state adapted patterns are not changed significantly by the limiter modification, except for the increase in level by the constant a.

However, the transient behavior is modified by the extra pattern function $g'(\theta,t)$, which has some rather interesting characteristics when plotted over time. For example, note that at time $t = 0$,

$$g'(\theta,0) = \left(1 - \frac{1}{a}\right) \sum_{i=1}^{K} \hat{W}_{qi} g_i(\theta) = \left(1 - \frac{1}{a}\right) G_q(\theta); \tag{4.187}$$

i.e., it reduces to the quiescent pattern and results in $G(\theta,0) = G_q(\theta)$, as it should. If we select $t = T_u$, at which time all of the unique transient decays have just finished, then all the remaining α_i will be identical and equal to α'_0, such that

$$g'(\theta,t) = \left(1 - \frac{1}{a}\right) e^{-\alpha'_0 t} \sum_{i=X_1}^{X_n} \hat{W}_{qi} g_i(\theta) \quad t \geq T_u \tag{4.188}$$

where $\alpha'_0 = (1 + \mu'_{im})/\tau'_0$ and $X_1, X_2, \ldots, X_n$ denote the nonunique members of the set of eigenvector beams. But such a summation will usually be approximately equal to the steady-state adapted pattern; i.e.,

$$G(\theta,\infty) \approx \sum_{i=X_1}^{X_n} \hat{W}_{qi} g_i(\theta). \tag{4.189}$$

Thus, for time $t \geq T_u$, Eq. (4.185) reduces to the approximation

$$G(\theta,t) \approx a\left\{1 - \left(1 - \frac{1}{a}\right) e^{-\alpha'_0 t}\right\} G(\theta,\infty) \quad t \geq T_u \tag{4.190}$$

where we have the steady-state pattern essentially established by time T_u and increasing slowly in level thereafter to its steady-state magnitude of $aG(\theta,\infty)$.

For precise pattern calculations during the transient, one should work with complete Eqs. (4.185) and (4.186). This requires computing a completely filled Q-transformation matrix and using all the eigenvector beams that have finite $\hat{W}_{qi}$ weighting. For example, in Case H, eigenvector beam $g_8(\theta)$ is not used in Eq. (4.119) because of the $(\mu_i - \mu_0)$

term deletion, but in Eq. (4.186) it is prominent and helps to account for the longer convergence time noted in Fig. 64.

In summary, the hard-limiter modification results in the same dynamic range improvements extolled in Sec. 3.4. It gives superior circuit operation and loop stability, but little improvement in transient response except for the special case of a single narrowband interference source. The advantages of dynamic-range improvement are enough to recommend incorporation of the hard limiter (or fast AGC).

5. CONCLUSION

An adaptive array consisting of a K-element linear array with K adaptive control loops of the Applebaum analog type derives feedback control error signals from the correlations between element signals, on the basis of the covariance matrix of the set of system inputs. The covariance matrix is a summation or repository of all interference distribution information as seen by the array in its operating environment.

The set of linear differential equations associated with the control-loop network can be solved by a Q-matrix transformation into orthonormal eigenvector space, with the Q matrix consisting of the eigenvectors of the covariance matrix. In this report, the purely mathematical Q-matrix transformation has been interpreted in terms of orthogonal beam-forming networks, similar in principle to a Butler matrix beam-forming network. This is the basis for an equivalent "orthonormal" adaptive control-loop network which is much easier to understand than the real network itself.

The Q-matrix beam-forming network produces a set of K orthogonal, normalized eigenvector beams, in which the array element weights associated with each eigenvector beam consists of the components of the eigenvector. The output powers from these beams are proportional to the associated eigenvalues and are decorrelated. The eigenvector beams have been used in a convenient expression for the output pattern function for the array. As developed in Eq. (4.119), the expression is

$$G(\theta,t) = G_q(\theta) - \sum_{i=1}^{K} (1 - e^{-\alpha_i t}) \left(\frac{\mu_i - \mu_0}{\mu_i + 1}\right) \hat{W}_{qi} g_i(\theta).$$

This requires only the quiescent pattern $G_q(\theta)$ plus the unique eigenvalues and associated unique eigenvectors. The term $(\mu_i - \mu_0)$ eliminates all of the eigenvector beams whose output power consists of receiver noise only. The expression uses the concept of array degrees of freedom, since one degree of freedom must be consumed for each unique eigenvalue generated by the covariance matrix.

Performance characteristics were calculated from the above expression for eight different distributions of interference sources, as listed in Table 2. These distributions were selected to demonstrate the effects of source power level, source location with respect to the quiescent beam pattern, source spacing in terms of array resolution, source bandwidth, and continuous source distributions. Some of the major effects noted were

1. Sidelobe jamming distorts the output pattern in proportion to the number of unique eigenvalues, i.e., the array degrees of freedom consumed.

2. Main-lobe jamming produces severe pattern distortion.

3. Slow convergence rates are associated with small eigenvalues, and small eigenvalues are generated by closely spaced sources, continuous source distributions, sources with bandwidth, low-power sources, and combinations of these.

4. Separated narrowband sources usually consume one array degree of freedom per source, but sources with bandwidth may consume two or three array degrees of freedom per source, depending on the source locations and their percentage bandwidths.

5. Narrowband sources are usually attenuated by developing a pattern null close to their locations. These nulls typically do not aline exactly with source position unless the source is very strong, with a power level of 30 dB or more above receiver noise power.

6. If there are many sources closely spaced so as to form a continuous distribution, the system attenuates them by developing a "low sidelobe notch" region in the adapted pattern; i.e., the array handles them on a resolution basis. This permits the array to use its degrees of freedom so efficiently that it can handle a large number of sources, far in excess of its number of available degrees of freedom.

In computing the eight source-distribution cases, the unique, retrodirective eigenvector beams were plotted. It was found that they could be characterized by a family of harmonically related pattern "modes." Case G, in particular, produced a classic, harmonically related set, up through the sixth harmonic. Even though these beams are not in real space, they give one an excellent perspective for the synthesis of adaptive pattern reactions to given interference distributions. They should be useful in developing beam-transformation algorithms and techniques for future adaptive systems.

Applebaum introduced a hard-limiter modification into his basic control loop to improve the circuit characteristics, particularly the system dynamic range. This modification was included in the analysis and resulted in a major change in the equivalent servo gain factors, plus the addition of an extra transient term in the above-mentioned output pattern function for the array.

One effect of the modification is that the magnitude levels of the adapted weights change considerably but slowly, so that there is no significant difference in the steady-state adapted pattern except for the increase in level. Also, the transient behavior is modified somewhat, but not by any large factor except in the very special case of a single narrowband jammer of low power level, for which a much faster response is obtained.

The present state-of-the-art in adaptive arrays is still in its infancy, and many problems remain to be addressed, in theory and in practice. However, progress is rapid and the future for these systems looks very promising. For example, accelerated convergence techniques are being developed to overcome sluggish response situations, and main-beam constraint techniques are being developed to overcome the objectionable main-beam distortions suffered by most of the current adaptive techniques.

REFERENCES

1. M.I. Skolnik, *Introduction to Radar Systems*, Chap. 4, McGraw-Hill, New York, 1962.
2. M.I. Skolnik, editor, *Radar Handbook*, Chap. 18 by F.M. Staudaher, McGraw-Hill, New York, 1970.
3. F.M. Staudaher, et al., "Adaptive Array Flight Test Definition Study," NRL Report 7695 (Confidential Report, Unclassified Title), Dec. 21, 1973.
4. Special issue on Active and Adaptive Antennas, *IEEE Trans. Antennas Propag.* **AP-12**, No. 2 (Mar. 1964).
5. S.P. Applebaum, R.G. Hiller, and P.W. Howells, "Sidelobe Cancellation Techniques," J. Missile Def. Res. V, No. 3, 129-153, Winter 1967 (Secret Article, Unclassified Title).
6. B. Widrow, "Adaptive Filters I: Fundamentals," Stanford Univ. Electronics Laboratories, Report SU-SEL-66-126 (Systems Theory Lab., Center for Systems Research, Tech. Report 6764-6), Dec. 1966.
7. F. Bryn, "Optimum Signal Processing of Three-Dimensional Arrays Operating on Gaussian Signals and Noise," *J. Acoust. Soc. Amer.* **34**, 289-297 (Mar. 1962).
8. S.W.W. Shor, "Adaptive Technique to Discriminate Against Coherent Noise in a Narrow-band System," *J. Acoust. Soc. Amer.* **39**, 74-78 (Jan. 1966).
9. P.E. Green, Jr., R.A. Frosch, and C.F. Romney, "Principles of an Experimental Large Aperture Seismic Array (LASA)," *Proc. IEEE* **53**, 1821-1833 (Dec. 1965).
10. R.T. Lacoss, "Adaptive Combining of Wideband Array Data for Optimal Reception," *IEEE Trans. Geosci. Electron* **GE-6**, No. 2, 78-86 (May 1968).
11. P.W. Howells, "Intermediate Frequency Side-Lobe Canceller," U.S. Patent 3,202,990, Aug. 24, 1965.
12. S.P. Applebaum, R.G. Hiller, and P.W. Howells, "Coherent Sidelobe Cancellation Techniques," Twelfth Annual Tri-Service Radar Symposium Record, Univ. of Michigan, pp. 469-490, AD 376-088, June 1966 (Secret Report, Unclassified Title).
13. S.P. Applebaum, "Adaptive Arrays," Syracuse Univ. Res. Corp., Report SPL TR 66-1, Aug. 1966.
14. S.P. Applebaum, et al. "Adaptive Antenna Arrays," Syracuse Univ. Res. Corp., Final Report SURC TR 71-137, Contract N00014-71-C-0230, June 30, 1971 (Secret Report, Unclassified Title).
15. R.C. Hansen, editor, *Microwave Scanning Antennas*, vol III, Chap. 5, Academic Press, New York, 1966.
16. A.E. Covington and N.W. Broten, "An Interferometer for Radio Astronomy With a Single-Lobed Radiation Pattern," *IRE Trans. Antennas Propag.* **AP-5**, No. 3, 247-255 (July 1957).
17. J.L. Pawsey and R.N. Bracewell, *Radio Astronomy*, International Monographs on Radio, Clarendon Press, Oxford, 1955.

18. M.F. Gardner and J.L. Barnes, *Transients in Linear Systems*, vol I, John Wiley & Sons, New York, 1942.

19. S.P. Applebaum and R.M. Davis, "Sidelobe Canceller Program, Special Report on Theory and Performance," Syracuse Univ. Res. Corp., Report SURC TR 71-90, Contract DAHC 60-69-C-0065, Apr. 1971 (Secret Report, Unclassified Title).

20. H. Chestnut and R.W. Mayer, *Servomechanisms and Regulating System Design*, 2d ed., vol I, John Wiley & Sons, New York, 1959.

21. L.E. Brennan, E.L. Pugh, and I.S. Reed, "Control-Loop Noise in Adaptive Array Antennas," *IEEE Trans. Aerosp. Electron. Syst.* AES-7, 254-262 (Mar. 1971).

22. F.B. Hildebrand, *Methods of Applied Mathematics*, 2d ed., Prentice-Hall, Englewood Cliffs, N.J., 1965.

23. J.H. Wilkinson, *The Algebraic Eigenvalue Problem*, Clarendon Press, Oxford, 1965.

24. Y.T. Lo, S.W. Lee, and Q.H. Lee, "Optimization of Directivity and Signal-to-Noise Ratio of an Arbitrary Antenna Array," *Proc. IEEE* 54, 1033-1045 (Aug. 1966).

25. S.M. Sanzgiri and J.K. Butler, "Constrained Optimization of the Performance Indices of Arbitrary Array Antennas," *IEEE Trans. Antennas Propag.* AP-19, 493-498 (July 1971).

26. R.F. Harrington, *Field Computation by Moment Methods*, Chap. 10, Macmillan, New York, 1968.

27. B. Widrow, P.E. Mantey, L.J. Griffiths, and B.B. Goode, "Adaptive Antenna Systems," *Proc. IEEE* 55, 2143-2159 (Dec. 1967).

28. L.J. Griffiths, "A Simple Adaptive Algorithm for Real-Time Processing in Antenna Arrays," *Proc. IEEE* 57, 1696-1704 (Oct. 1969).

29. C.K.H. Tsao, R.G. Cease, W.J. Bickford, and H.J. Rowland, "Analysis of a Signal Processor for an Antenna Array," *IEEE Trans. Aerosp. Electron. Syst.* AES-6, 79-87 (Jan. 1970).

30. A.L. McGuffin and W.J. McDaniel, "A Comparison of Sidelobe Cancellation and Adaptive Array Processing," Sixteenth Annual Tri-service Radar Symposium Record, Univ. of Michigan, pp 559-594, June 1970 (Secret Report, Unclassified Title).

31. "Adaptive Array Techniques for Coherent Airborne Radars," Technology Service Corp., Final Report TSC-PD-030-1, Contract N-00019-69-C-0662, Feb. 26, 1970 (Confidential Report, Unclassified Title).

32. L.E. Brennan and I.S. Reed, "Effect of Envelope Limiting in Adaptive Array Control Loops," *IEEE Trans. Aerosp. Electron. Syst.* AES-7, 698-700 (July 1971).

33. R.T. Compton, Jr., "Adaptive Arrays: On Power Equalization With Proportional Control," Ohio State Univ. Electroscience Lab., Report 3234-1, Contract N00019-71-C-0219, Dec. 1971.

34. K.L. Reinhard, "An Adaptive Array for Interference Rejection in a Coded Communication System," Ohio State Univ. Electroscience Lab., Report 2738-6, Contract F30602-69-C-0112, Apr. 1972.

35. O.L. Frost, III, "An Algorithm for Linearly Constrained Adaptive Array Processing," *Proc. IEEE* 60, 926-935 (Aug. 1972).

36. C.A. Baird, Jr., et al., "Adaptive Processing for Antenna Arrays," Radiation, Inc., Final Report, RADC-TR-72-174, Contract F30602-71-C-0173, July 1972.

37. L.E. Brennan and I.S. Reed, "Theory of Adaptive Radar," *IEEE Trans. Aerosp. Electron. Syst.* AES-9, 237-252 (Mar. 1973).

38. C.L. Zahm, "Application of Adaptive Arrays to Suppress Strong Jammers in the Presence of Weak Signals," *IEEE Trans. Aerosp. Electron. Syst.* AES-9, 260-271 (Mar. 1973).

39. R.L. Riegler and R.T. Compton, Jr., "An Adaptive Array for Interference Rejection," *Proc. IEEE* 61, 748-758 (June 1973).

40. S.A. Schelkunoff and H.T. Friis, *Antennas: Theory and Practice*, John Wiley & Sons, New York, 1952.

41. D.E.N. Davies, "Independent Angular Steering of Each Zero of the Directional Pattern for a Linear Array," *IEEE Trans. Antennas Propag.* AP-15, 296-298 (Mar. 1967).

42. Program CMPLXEIG, University of Wisconsin Computing Center, Jan. 1966, UWCC ID Code B0018-00.

Appendix A
TRANSIENT RESPONSE OF A SIMPLE *RLC* CIRCUIT

From the circuit shown in Fig. A1, the integro-differential equation may be written as

$$\frac{W}{R} + C\,\frac{dW}{dt} + \frac{1}{L}\int W\,dt = \frac{v}{R}. \tag{A1}$$

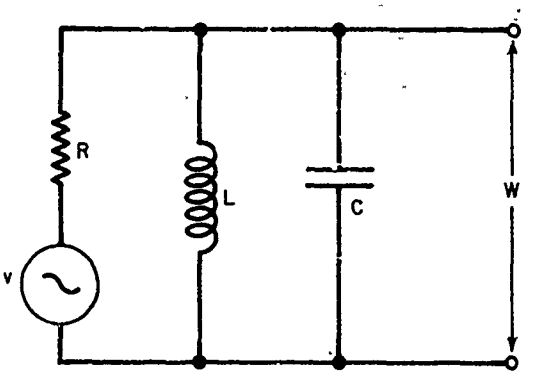

Fig. A1—Single-tuned *RLC* filter circuit for *W*

Taking the Laplace transform of both sides and assuming that initial charges and currents are zero, we get

$$\left(\frac{1}{R} + CS + \frac{1}{LS}\right) W(S) = \frac{V(S)}{R}, \tag{A2}$$

where $S = \sigma + j\omega$ is the usual Laplace complex variable. Then

$$W(S) = Y(S)\,V(S), \tag{A3}$$

where

$$Y(S) = \frac{2\alpha S}{(S+\alpha)^2 + \beta^2} \tag{A4}$$

$$\beta^2 = \beta_0^2 - \alpha^2 \tag{A5}$$

$$\beta_0^2 = \left(\frac{1}{LC}\right) = \text{natural resonant frequency} \tag{A6}$$

$$\tau = 2RC = \text{time constant} \tag{A7}$$

$$\alpha = \frac{1}{\tau} = \frac{1}{2RC} = \text{attenuation constant}. \tag{A8}$$

$Y(S)$ is the Laplace transform expression for the circuit itself, independent of any excitation function.

If we now take an input step function of a sinusoid for v, so that $v = 0$ for $t < 0$ and

$$v = \left(\frac{abG}{2}\right) \sin(\omega_0 t + \phi_0 - u) \quad \text{for} \quad t \geqslant 0, \tag{A9}$$

then its Laplace transform will be found to be

$$V(S) = \frac{abG}{2} \left\{ \frac{\sin(\phi_0 - u)\left[S + \dfrac{\omega_0}{\tan(\phi_0 - u)}\right]}{S^2 + \omega_0^2} \right\}. \tag{A10}$$

From Eq. (A3) we may write

$$W(S) = \frac{abG}{2} \left[\frac{2\alpha S}{(S+\alpha)^2 + \beta^2}\right] \left\{ \frac{\sin(\phi_0 - u)\left[S + \dfrac{\omega_0}{\tan(\phi_0 - u)}\right]}{S^2 + \omega_0^2} \right\}. \tag{A11}$$

This may be rewritten in the following series form, based upon the roots of S:

$$W(S) = abG \left\{ \frac{A}{2} \left[\frac{e^{j\psi}}{(S+\alpha) - j\beta} + \frac{e^{-j\psi}}{(S+\alpha) + j\beta}\right] + \frac{B}{2j}\left(\frac{e^{j\theta}}{S - j\omega_0} - \frac{e^{-j\theta}}{S + j\omega_0}\right) \right\}. \tag{A12}$$

Solving for the constants θ, B, ψ, and A, we have

$$\theta = \phi_0 - u + \tan^{-1}\left(\frac{\beta_0^2 - \omega_0^2}{2\alpha\omega_0}\right) \tag{A13}$$

$$B = \frac{1}{2\sqrt{1 + \left(\dfrac{\beta_0^2 - \omega_0^2}{2\alpha\omega_0}\right)^2}}. \tag{A14}$$

$$\psi = \frac{\pi}{2} + \tan^{-1}\left[\frac{\beta(\beta_0^2 - \omega_0^2)}{\alpha(\beta_0^2 + \omega_0^2)}\right] + \tan^{-1}\left[\frac{\beta \tan(\phi_0 - u)}{\omega_0 - \alpha \tan(\phi_0 - u)}\right] \tag{A15}$$

$$A = B\left(\frac{\beta_0}{\beta}\right)\sqrt{1 + \left[\frac{\beta \tan(\phi_0 - u)}{\omega_0 - \alpha \tan(\phi_0 - u)}\right]^2}\left[\cos(\phi_0 - u) - \frac{\alpha}{\omega_0}\sin(\phi_0 - u)\right]. \quad \text{(A16)}$$

Finally, we get our output in the time domain by taking the inverse Laplace transform of Eq. (A12), so that

$$W = L^{-1}[W(S)] \quad \text{(A17)}$$

$$W = abG[e^{-\alpha t}A\cos(\beta t + \psi) + B\sin(\omega_0 t + \theta)]. \quad \text{(A18)}$$

Appendix B

CONSTRUCTION OF NONUNIQUE EIGENVECTORS FOR FILLING OUT THE Q MATRIX

The method for filling out the Q matrix is based on using controlled null placement to optimize spatial coverage, in a manner similar to the operation of the Davies tree network discussed in Sec. 4.3. The vectors so derived are then orthogonalized by the Gram-Schmidt procedure and normalized to produce the desired eigenvectors.

Using Case B of Table B1, which involves two sources located at 18 and 22 degrees respectively, we establish these two source locations on the Z-plane unit circle as shown in Fig. B1a, using Eq. (4.80): $Z = \exp(j2u)$. These shall be regarded as *constrained null locations* for the nonunique beams. It is necessary to have as many constrained nulls as there are unique eigenvalues; we shall denote this number by the symbol K_u. With K_u null positions fixed, there remain $(K - K_u)$ null positions to be located on the circle and, although the choice of these positions is theoretically arbitrary, it seems desirable from a beam-forming point of view to seek locations which optimize the spatial coverage by maximizing the separations between the remaining null locations. If this principle is applied in Fig. B1b, the remaining null locations should be spaced apart equally by the angle

$$\left(\frac{360 - \phi}{K - K_u + 1}\right) = 49.7^\circ$$

where ϕ is the angular separation of the two closely spaced constrained nulls on the circle.

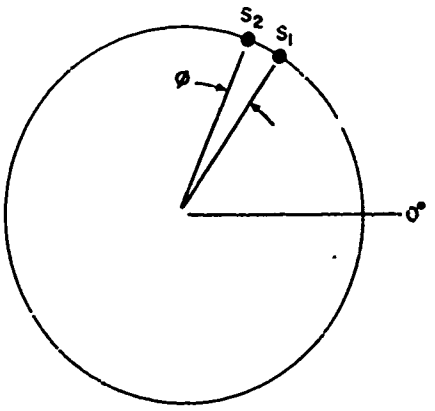

(a) Constrained-null (or source position) locations

Fig. B1—Null locations on Z-plane unit circle for Case B

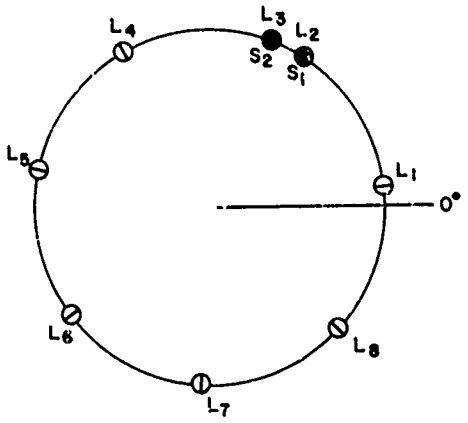

(b) Locations chosen for six remaining nulls

Fig. B1—Null locations on Z-plane unit circle for Case B (Continued)

When all of the null locations L_1 through L_8 have been selected, the next step is to form the nonunique beams by choosing $(K-1)$ of the K null positions for use in Eq. (3.83): $F(Z) = a_{K-1}(Z-Z_1)(Z-Z_2)(Z-Z_3)\ \ldots\ (Z-Z_{K-1})$. The constrained null positions L_2 and L_3 must be used in each beam. If the ith beam is denoted by $G_i(Z)$, then

$$G_i(Z) = (Z-Z_1)(Z-Z_2)(Z-Z_3)\ \ldots\ (Z-Z_{K-1}). \tag{B1}$$

The null selections for the six beams associated with Fig. B1 are shown in Table B2. Computer programs are available for using the null positions of Eq. (B1) to solve for the complex coefficients associated with the standard polynomial form of $G_i(Z)$,

$$G_i(Z) = A_0 + A_1Z + A_2Z^2 + A_3Z^3 + \ldots + A_{K-1}Z^{K-1}. \tag{B2}$$

These complex coefficients constitute the components of the element weighting vectors associated with the beams:

$$G_i(\theta) = (W_i^t S) = \sum_{k=0}^{K-1} A_k S_{k+1}, \tag{B3}$$

where

$$W_i^t = [A_0, A_1, A_2, A_3, \ldots, A_{K-1}] \tag{B4}$$

and S is defined in Eq. (4.8): $S^t = [S_1, S_2, S_3, \ldots, S_K]$. In general, the W_i vectors calculated by the above procedure are not orthogonal to one another, and it is necessary to orthogonalize by the Gram-Schmidt procedure*.

*F.B. Hildebrand, *Methods of Applied Mathematics*, 2d. ed., Prentice-Hall, Inc., Englewood Cliffs, N.J., 1965.

Table B1
Selected Distributions of Interference Sources

Case	Interference Sources					Unique Eigenvalues	
	Number of Sources	Power Ratios	Location Angle (Deg)	Bandwidth (%)	Spectrum Lines	Number	Values
A	1	1,250	21	0	1	1	10,001
B	2	1,250 1,200	18 22	0 0	1 1	2	18,544 1,058
C	2	1,250 125	18 22	0 0	1 1	2	10,812 190
D	4	40 125 400 1,250	18 25 33 42	0 0 0 0	1 1 1 1	4	11,616 2,486 406 16.5
E1	1	1,250	42	0	1	1	10,001
E2	1	1,250	42	7	3	2	9,986 16.4
E3	1	1,250	42	15	16	3	9,529 469 4.7
F	1	1,250	5	0	1	1	10,001
G	3	1,100 1,100 1,100	36 48 66	26 21 19	11 11 11	6	13,316 9,692 3,091 296 10.5 1.16
H	6	1,100 1,100 1,100 1,100 1,100 1,100	-66 -48 -36 36 48 66	19 21 26 26 21 19	11 11 11 11 11 11	8	13,532 13,386 12,619 9,682 3,224 350 14.7 1.18

Table B2
Beam Null Locations

Null Positions	Nonunique Beams					
	$G_1(\theta)$	$G_2(\theta)$	$G_3(\theta)$	$G_4(\theta)$	$G_5(\theta)$	$G_6(\theta)$
Z_1	L_2	L_1	L_1	L_1	L_1	L_1
Z_2	L_3	L_2	L_2	L_2	L_2	L_2
Z_3	L_4	L_3	L_3	L_3	L_3	L_3
Z_4	L_5	L_5	L_4	L_4	L_4	L_4
Z_5	L_6	L_6	L_6	L_5	L_5	L_5
Z_6	L_7	L_7	L_7	L_7	L_6	L_6
Z_7	L_8	L_8	L_8	L_8	L_8	L_7

In our example, we start with the two unique eigenvectors $\mathbf{e}_1$ and $\mathbf{e}_2$, the components of which are printed out in Table B3. These two are already orthogonal and normalized, of course. We next take the first vector $\mathbf{W}_1$, corresponding to the nonunique beam $G_1(\theta)$, and form the new vector,

$$\mathbf{V}_3 = \mathbf{W}_1 - q_1\mathbf{e}_1 - q_2\mathbf{e}_2 . \tag{B5}$$

The requirement that $\mathbf{V}_3$ be orthogonal to $\mathbf{e}_1$ leads to the relation

$$(\mathbf{e}_1^{*t}\mathbf{V}_3) = (\mathbf{e}_1^{*t}\mathbf{W}_1) - q_1 = 0$$

or

$$q_1 = (\mathbf{e}_1^{*t}\mathbf{W}_1) ; \tag{B6}$$

similarly,

$$q_2 = (\mathbf{e}_2^{*t}\mathbf{W}_1) . \tag{B7}$$

Thus, we "subtract off" the $\mathbf{e}_1$ and $\mathbf{e}_2$ components of $\mathbf{W}_1$, obtaining the vector $\mathbf{V}_3$, which is now orthogonal to both $\mathbf{e}_1$ and $\mathbf{e}_2$. $\mathbf{V}_3$ is then normalized by dividing by its Hermitian length to get the eigenvector $\mathbf{e}_3$:

$$\mathbf{e}_3 = \frac{\mathbf{V}_3}{\sqrt{(\mathbf{V}_3^{*t}\mathbf{V}_3)}} . \tag{B8}$$

Eigenvector $\mathbf{e}_3$ is therefore our first nonunique eigenvector.

To get the second nonunique eigenvector $\mathbf{e}_4$, we take the second vector $\mathbf{W}_2$ from our set and form the new vector $\mathbf{V}_4$, orthogonal to each eigenvector, so that

Table B3
Eigenvalues and Eigenvectors for a Two-Source Case*†

Eigenvector Coefficient	Amplitude	Phase Angle (Deg)
1,1	0.340120	69.7477
1,2	0.351501	8.3626
1,3	0.359156	-53.03
1,4	0.363004	245.573
1,5	0.363004	184.175
1,6	0.359156	122.778
1,7	0.351501	61.3852
1,8	0.340120	0
2,1	0.537157	250.308
2,2	0.387808	188.701
2,3	0.234347	126.989
2,4	0.078413	64.5464
2,5	0.078413	185.762
2,6	0.234347	123.319
2,7	0.387808	61.607
2,8	0.537157	0

*Jammer power ratios 1,250; location angles 18° and 22°; bandwidth 0%; one spectrum line.
†Unique eigenvalues: 18,544.4 and 1,057.58

$$V_4 = W_2 - q_1 e_1 - q_2 e_2 - q_3 e_3 , \tag{B9}$$

where the q_i constants are to be evaluated as before. Dividing V_4 by its Hermitian length then results in e_4.

The above process is simply repeated for each of the W_i in turn, until all of the non-unique eigenvectors have been computed, whereupon they can be entered into the Q matrix to fill it out.